UC Santa Barbara

UC Santa Barbara Electronic Theses and Dissertations

Title

In-Situ Characterization of the Surfaces & Interfaces in Superconducting Coplanar Waveguides, RNiO3 heterostructures, and Self Assembled ErSb Nanostructures Grown by Molecular Beam Epitaxy

Permalink

https://escholarship.org/uc/item/0f4080px

Author

Wilson, Nathaniel Spencer

Publication Date

2017

Peer reviewed|Thesis/dissertation

eScholarship.org Powered by the California Digital Library University of California

UNIVERSITY OF CALIFORNIA

Santa Barbara

In-Situ Characterization of the Surfaces & Interfaces in Superconducting Coplanar Waveguides, $RNiO_3$ heterostructures, and Self Assembled ErSb Nanostructures Grown by Molecular Beam Epitaxy

By

Nathaniel Spencer Wilson

Committee in charge:

Professor Christopher Palmstrøm, Chair

Professor Art Gossard

Professor Susanne Stemmer

Professor John Martinis

December 2017

The dissertation of Nathaniel Spencer Wilson is approved

Art Gossard

Susanne Stemmer

John Martinis

Christopher Palmstrøm, Committee Chair

August 2017

ACKNOWLEDGEMENTS

As is the case of any work of this size its success is due to the efforts of more then any one person. I would like to extend heartfelt thanks to all the people who have contributed, in one form or another, to my success during graduate school.

My PI Prof. Chris Palmstrøm who introduced me to this field, and has been a constant unending font of ideas throughout the entire process. Chris has always been a strong proponent of good science before all else and it shows in all of the graduate students that leave his group.

The rest of my committee for their contributions to the various subjects discussed within this document. Prof. John Martinis for showing me what it takes to really move a project from a university research setting and into industry it has been fascinating to watch the evolution of superconducting qubits while I have been here. Prof. Susanne Stemmer who was involved with the research on transition metal oxide materials and whose group I have discussed many of the difficulties of oxide MBE growth with over the years. Prof. Art Gossard for being a guru of MBE knowledge, for shaping the culture of the MBE groups here into what it is today, and keeping everyone involved with each other despite the myriad number of different projects we are all working on.

My fellow graduate students, post docs, visiting professors, and project scientists in the Palmstrøm group both past and present; Shinobu, Brian, Jason, Tony, Ludwig, Sahil, Bo, Anthony, Sean, Jay, Dan, Tobias, Tony, Mihir, Joon Sue, Sukgeon, Shouvik, Aranya, Alex, Elliot, and Hadass. These are the people truly responsible for everything that comes out of the Palmstrøm lab it is only with their combined input and support that any of this is possible.

I would like to thank the groups of Anders Mikkelsen and Rainer Timm at Lund University, Sweden. The close collaboration with them and their students Martin, Johan and Jovana has taught me much about STM over the years.

The shared facilities at UCSB are second to none and I would like to thank all the work and discussions with the staff their over the years, the CNSI microscopy facility in particular Stephan Kraemer, the nanofabrication facility, and the MRL x-ray lab have all been immensely helpful over the years.

Finally I would like to thank all the friends I've made here over the years you have made all the long nights bearable, and my family who without their continued support over the years I would never find myself in the place I am now.

CURRICULEM VITA OF NATHANIEL S. WILSON
August 2017

EDUCATION

University of California, Santa Barbara, CA
PhD, Materials Engineering 2011-2017

Purdue University, West Lafayette, IN
BS. Materials Science (with Distinction) 2007-2011

RESEARCH EXPERIENCE

University of California Santa Barbara
Doctoral Research
Research Advisor: Prof. Chris Palmstrøm

- Investigated growth of self-assembled ErSb nanostructures in a GaSb matrix grown by Molecular Beam Epitaxy (MBE). Identified growth mode responsible for formation of horizontal nanowires and identified new low temperature growth mode.
- Investigated how surface chemistry and morphology of Sapphire and Silicon surfaces leads to losses in superconducting aluminum wave guides grown by MBE for quantum computing applications
- Grew thin films of $LaNiO_3$ and characterized the thickness dependent metal to insulator transition via Scanning Tunneling Spectroscopy (STS)

Purdue University
Undergraduate Research
Research Advisor: Prof. Alejandro Strachan

- Investigated yield criterion of PMMA via molecular dynamic simulation as a function of uniaxial to isotropic strain.
- Investigated the degradation of sintered $SrTiO_3$ for thermoelectric use under high temperature gradients. (Senior Design in partner with Corning Inc.)

RESEARCH INTERESTS

- Impact of interfaces on device and material properties, and control of interfaces during growth and sample preparation.
- Surface mediated formation of nanostructures, particularly understanding underlying mechanisms in order to achieve nanostructure growth in a wider range of material systems

TEACHING EXPERIENCE

University of California Santa Barbara

Teaching Assistant

- Structure Evolution (Spring 2013)
- Led Discussion Sections

PUBLICATIONS and PRESENTATIONS

Anthony McFadden, Nathaniel Wilson, Tobias Brown-Heft, Chris Palmstrom, Dan Pennachio, Mihir Pendharkar, John Logan Interface Formation of Epitaxial MgO/Co_2 MnSi(001) Structures: Elemental Segregation and Oxygen Migration Journal of Magnetism and Magnetic Materials (Accepted)

Anthony McFadden, Tobias Brown-Heft, Dan Pennachio, Nathaniel Wilson, John Logan, and Chris Palmstrøm. Oxygen Migration in Epitaxial CoFe/MgO/Co_2MnSi Magnetic Tunnel Junctions. J. Appl. Phys. (Accepted)

S. D. Harrington, A. Sharan, A. D. Rice, J.A. Logan, A.P. McFadden, M. Pendharkar, D.J. Pennachio, N.S. Wilson, Z. Gui, A. Janotti, and C. J. Palmstrøm Valence-band offsets of CoTiSb/$In_{0.53}Ga_{0.47}As$ and CoTiSb/$In_{0.52}Al_{0.48}As$ heterojunctions App. Phy. Lett. (Accepted)

J.A. Logan, T.L. Brown-Heft, S.D. Harrington, N.S. Wilson, A.P. McFadden, A.D. Rice, M. Pendharkar, and C.J. Palmstrøm, Growth, structural, and magnetic properties of single-crystal full-Heusler Co2TiGe thin films J. Appl. Phys. **121**, 213903 (2017).

Eugenio Jaramillo, Nathaniel Wilson, Stephen Christensen, Jonathan Gosse, and Alejandro Strachan. Energy-based yield criterion for PMMA from large-scale molecular dynamics simulations Phys. Rev. B **85**, 024114 (2012)

N. Wilson, S. Kraemer, C. Palmstrøm (2017). Growth of Self Assembled Horizontal Nanowires in a GaSb Matrix, Presented at APS, New Orleans, LA

N. Wilson, S. Kraemer, C. Palmstrøm (2017). Surface Mediated formation of GaSb/ErSb Nanostructures, Presented at PCSI, Santa Fe, NM

N. Wilson, S. Kraemer, J. Kawasaki, B. Schultz, C. Palmstrøm (2016). Growth and Characterization of Horizontal ErSb Nanowires in a GaSb Matrix, Presented at NAMBE, Saratoga Springs, NY

N. S. Wilson, C. J. Palmstrøm (2014). Characterization of the Electronic Structure of $LaNiO_3$ Thin Films Through a Metal to Insulator Transition, Presented at PCSI, Santa Fe, NM

PUBLICATIONS IN PREPERATION

N. S. Wilson, S. Kraemer, D. Pennachio, P. Callahan, M. Pendharker, C. J. Palmstrøm. Mechanism for In-plane Self Assembled Nanowire Formation, *Manuscript in Preparation*

SELECTED AWARDS

PCSI Young Investigator
2017

SKILLS

Molecular Beam Epitaxy (MBE), Scanning Tunneling Microscopy (STM), X-Ray Photoelectron Spectroscopy (XPS), Atomic Force Microscopy (AFM), X-Ray Diffraction (XRD), Scanning Electron Microscopy (SEM)

ABSTRACT

In-Situ Characterization of the Surfaces & Interfaces in Superconducting Coplanar Waveguides, $RNiO_3$ heterostructures, and Self Assembled ErSb Nanostructures Grown by Molecular Beam Epitaxy

By

Nathaniel Spencer Wilson

Surfaces and interfaces are responsible for many of the properties observed in electronic devices. However, characterizing the properties and effects of these interfaces remains one of the most challenging problems in materials science. This is due to both the limited number of characterization techniques that are sensitive to small interfacial regions, as well as the problems associated with surface contamination when exposing a clean surface to atmosphere. In this thesis these problems are overcome through the use of in-situ growth and characterization. Taking advantage of the layer by layer interfacial control achievable with molecular beam epitaxy (MBE) highly precise surfaces and interfaces are created. In-situ surface characterization via x-ray photoelectron spectroscopy (XPS) and scanning tunneling microscopy (STM) is then used to characterize the grown structures. Three different materials are examined, Al superconducting coplanar waveguides (SCW), metal to insulator transitions in rare earth nickelates, and self-assembled ErSb nanostructures. Collectively, these material systems

demonstrate the importance of contaminants at interfaces, interfacial control of material properties, and the effect of surfaces on material growth.

Two level states are thought to be one of the primary loss mechanisms for qubits and resonators fabricated from SCW. In-situ XPS is used to analyze the physical changes that occur at the surface during cleaning procedures used to improve qubit coherence times. Possible sources of TLS are identified, and include the presence of hydrogen and carbon on the initial sapphire substrate. Requirements for creating a similar TLS free surface when transitioning to SCW fabrication using silicon substrates is also discussed.

Materials in the $RNiO_3$ (R = a trivalent rare earth ion) family exhibit a metal to insulator transition(MIT) as a function of temperature and film thickness. Strain is shown to clearly suppress or enhance the MIT observed in $PrNiO_3$ thin films. A separate MIT transition is observed as a function of $LaNiO_3$ film thickness and characterized by in-situ STM and XPS. A clear gap is observed in the density of states for thin $LaNiO_3$ films providing insight into the nature of the MIT and suggesting a source other than disorder. $LaAlO_3$/$LaNiO_3$ superlattices are characterized and show that the MIT and transport properties of $LaNiO_3$ may be tunable via superlattice structure.

$Er_xGa_{1-x}Sb$ is a model system for examining self-assembled nanostructures producing nanoparticles, out-of-plane nanowires, in-plane nanowires and nanosheets. The morphology of the growth surface is characterized via in-situ STM. The growth mechanism responsible for the transition from out-of-plane to in-plane nanowire growth is identified as the formation of large macrosteps with step heights of ~7nm flowing across the surface and a surface energy model is developed to predict this behavior. A

novel nanoparticle consisting of extremely thin in-plane nanowires was identified for low temperature, high Sb pressure growths and may prove beneficial to a number of technological applications.

Table of Contents

I. Introduction 1

II. Superconducting resonators and qubits 3

A. What is a qubit? 3

B. Decoherence in qubits 4

C. The xmon qubit and two level states 5

III. Metal to insulator transition of rare earth nickelates 13

A. Perovskite structure 13

B. Metal to insulator transition in $RNiO_3$ 14

IV. ErSb self-assembled nanostructures 21

A. Introduction 21

B. Observed nanostructures 22

C. Embedded growth mode 24

V. Experimental techniques 29

A. Molecular beam epitaxy 29

B. X-ray Photoemission Spectroscopy 36

C. Scanning tunneling microscopy 39

D. Scanning tunneling spectroscopy 42

VI. Source of TLS in superconducting resonators 44

A. XPS analysis of sapphire (0001) surface 44

B. Ex-situ preparation of Si (001) surface 50

C. In-situ cleaning of Si(001) surface 53

D. Conclusions & future Work 58

VII. Interfacial control of the metal to insulator transition in $RNiO_3$ 61

A. Growth of $RNiO_3$ by MBE 61

B. Transport properties of $RNiO_3$ thin films 73

C. XPS of $LaNiO_3$ heterostructures 78

D. STS of $LaNiO_3$ MIT 86

E. Superlattice structures 92

F. Conclusion and future work 98

VIII. Formation of In-plane ErSb nanowires 101

A. Experimental setup 101

B. Characterization of nanowires 102

C. Surface Energy Model 111

D. Horizontal nanowire formation mechanism 115

E. Low temperature growth mode 119

F. Conclusions and Future Work 127

IX. Summary and Conclusion 128

X. References 133

XI. Appendix A – sapphire surface prep and buffer growth 144

A. Ex-situ preparation of sapphire (0001) surface 144

B. Sapphire buffer growth 146

XII. Appendix B – STM of Heusler materials 154

A. NiTiSn 154

B. $Au_xPt_{1-x}LuSb$ 158

LIST OF FIGURES

Figure II-1A bloch sphere representation illustrating the possible states of a qubit the Z axis represents the energy level of the qubit while the x and y plane represents the phase. Image from wikipedia [136] .. 4

Figure II-2 (a) An Xmon qubit surrounded by the control and readout circuit elements, the Xmon is the crossed shaped capacitor in the bottom right, and the SQUID loop (b), Josephson junctions highlighted in blue. (c) Diagram of the qubit and surrounding circuit elements. Reprinted figure with permission R. Barends, J. Kelly, A. Megrant, D. Sank, E. Jeffrey, Y. Chen, Y. Yin, B. Chiaro, J. Mutus, C. Neill, P. O'Malley, P. Roushan, J. Wenner, T. C. White, A. N. Cleland, and J. M. Martinis, "Coherent josephson qubit suitable for scalable quantum integrated circuits," Phys. Rev. Lett., vol. 111, no. 8, pp. 1–5, 2013 7

Figure II-3 Schematic of the double potential well of a two level state. If the energy spacing between the two levels is similar to that of qubit interactions may occur. 8

Figure II-4 (a) cross sectional view of a coplanar waveguide depicting dimensions and interfaces. (b) Participation ratios of the different interfaces present in a coplanar waveguide as a function of geometry. Reprinted from J. Wenner, R. Barends, R. C. Bialczak, Y. Chen, J. Kelly, E. Lucero, M. Mariantoni, A. Megrant, P. J. J. O'Malley, D. Sank, A. Vainsencher, H. Wang, T. C. White, Y. Yin, J. Zhao, A. N. Cleland, and J. M. Martinis, "Surface loss simulations of superconducting coplanar waveguide resonators," Appl. Phys. Lett., vol. 99, no. 11, pp. 2009–2012, 2011., with the permission of AIP Publishing. 10

Figure II-5 Power dependence of the internal quality factor Qi versus average photon number in the resonator <n_{photon}>, for resonators with w =15μm. Lines are guides to the eye. The typical low-power statistical error from a least-squares fit of Eq. (3) is ~3%, smaller than the symbol size. Reprinted from A. Megrant, C. Neill, R. Barends, B. Chiaro, Y. Chen, L. Feigl, J. Kelly, E. Lucero, M. Mariantoni, P. J. J. O'Malley, D. Sank, A. Vainsencher, J. Wenner, T. C. White, Y. Yin, J. Zhao, C. J. Palmstrøm, J. M. Martinis, and A. N. Cleland, "Planar superconducting resonators with internal quality factors above one million," Appl. Phys. Lett., vol. 100, no. 11, 2012., with the permission of AIP Publishing. 11

Figure III-1Crystal structure of a cubic perovskite material, atom positions are labeled as would be expected for $LaNiO_3$. Octahedra are drawn showing the Ni-O bonds which are the dominant conduction pathway in the $RNiO_3$. 14

Figure III-2 Illustration of how conduction of charge between lattice sites results in an increase in energy by an amount equal to the repulsion between two electrons for a half-filled band (bottom) while a partially filled band of any other filling results in no net change in energy (top). 16

Figure III-3 Diagram illustrating how the electron-electron interactions in a half filled band result in a repulsive force creating an energy splitting (U) between the filled and unfilled states creating an Upper Hubbard Band (UHB) and Lower Hubbard Band (LHB). One of two types of insulators can result a Mott-Hubbard Band where the band gap is between the UHB and LHB, or a charge-transfer insulator where the band gap is between two bands of different character here illustrated as a gap between the d and p bands. 17

Figure III-4 Phase diagram showing the metal to insulator magnetic transition for the $RNiO_3$ family of materials plotted as a function of rare earth ionic radius and tolerance factor, a measure of the octahedral tilts in the crystal with smaller tolerance factor corresponding to greater tilts. Reprinted figure with permission from J. B. Torrance, P. Lacorre, A. I. Nazzal, E. J. Ansaldo, and C. Niedermayer, "Systematic study of insulator-metal transitions in perovskites RNiO3 (R=Pr,Nd,Sm,Eu) due to closing of charge-transfer gap," Phys. Rev. B, vol. 45, no. 14, pp. 8209–8212, 1992 copyright 1992 by the American Physical Society. 18

Figure III-5 Schematic diagram of the type of heterostructure theoretically needed to create a Mott based transistor. 19

Figure IV-1 (Right) Crystal structures for the rocksalt ErSb and the zincblende GaSb along with lattice parameters. (Left) Ternary phase diagram for the Er-Ga-Sb material system at 800°C, of interest is the tieline between ErSb and GaSb which shows little solid solubility between the two. Ternary phase diagram reprinted with permission from A. Guivarc'h, A. Le Corre, P. Auvray, B. Guenais, J. Caulet, Y.

Ballini, R. Gúcrin, S. Députier, M. C. Le Clanche, G. Jézéquel, B. Lépine, A. Quémerais, and D. Sébilleau, "Growth by molecular beam epitaxy of (rare-earth group V element)/III-V semiconductor heterostructures," J. Mater. Res., vol. 10, no. 8, pp. 1942–1952, 1995. 22

Figure IV-2 TEM image showing the range of self-assembled nanoparticles observed in the $Er_xGa_{1-x}Sb$ material system with variation of the Er composition. At 3% or less ErSb composition isotropic nanoparticles are observed, from ~5% to 30% out-of-plane ErSb nanowires form, 30%-50% in-plane ErSb nanowires form, and >50% sheets of ErSb are observed. Figure created by Jason Kawasaki. 24

Figure IV-3 STM topographic images, line scans and schematics showing the evolution of the sample surface for (a) ErSb nanoparticles nucleated on a GaSb surface by deposition of 0.6 monolayers of ErSb with continued overgrowth of GaSb in increments of 2 monolayers, and (b) alternative layers of 0.6 monolayers of ErSb and 2 monolayers of GaSb deposited on the sample surface. Reprinted with permission from J. K. Kawasaki, B. D. Schultz, H. Lu, A. C. Gossard, and C. J. Palmstrøm, "Surface-mediated tunable self-assembly of single crystal semimetallic ErSb/GaSb nanocomposite structures," Nano Lett., vol. 13, no. 6, pp. 2895–2901 2013. Copyright 2017 American Chemical Society. 26

Figure IV-4 Composite image consisting of HAADF-STEM images along the [110] and [110] crystallographic directions, and a 3-D representation of a STM image of the [001] growth surface. The out-of-plane component of the STM image is exaggerated compared to the rest of the image for aid in identifying the observed surface reconstructions corresponding to GaSb and ErSb. 28

Figure V-1 Schematic of a typical MBE system, effusion cells provide elemental fluxes for film growth, a manipulator allows for substrate rotation and heating during growth. In-situ characterization of the surface is present in the form of reflective high energy electron diffraction. A cryo-panel is present to ensure particles stick to the walls and do not drift onto the substrate. 29

Figure V-2 Diagram showing the crystal surface, the intersection of the ewald sphere with k-space and the observed diffraction pattern for a smooth 2-D surface (a-c), a rough epitaxial surface (d-f) and a polycrystalline surface (g-i). Reprinted with permission from F. Tang, T. Parker, G.-C. Wang, and T.-M. Lu, "Surface texture evolution of polycrystalline and nanostructured films: RHEED surface pole figure analysis," J. Phys. D. Appl. Phys., vol. 40, pp. R427–R439, 2007. 32

Figure V-3 – Schematic showing the growth of a monolayer on a smooth surface with the corresponding scattering of an electron beam from the increasingly rough surface, and the resulting intensity of the RHEED signal as a function of surface morphology. Reprinted V. P. LaBella, M. R. Krause, Z. Ding, and P. M. Thibado, "Arsenic-rich GaAs(0 0 1) surface structure," Surf. Sci. Rep., vol. 60, no. 1–4, pp. 1–53, 2005 with permission from Elsevier. 34

Figure V-4 Diagram of the Palmstrøm MBE lab at the University of California Santa Barbara. The qubit and $RNiO_3$ materials were grown in the Oxide/Nitride chamber while the ErGaSb films were grown in the III-V growth chamber. All films are able to be characterized in-situ with x-ray photoelectron spectroscopy, or scanning tunneling microscopy. 36

Figure V-5 Cartoon of the experimental setup in XPS (left) and a diagram of the photoemission process (right). 37

Figure V-6 Plot of electron mean free path as a function of energy commonly referred to as the universal curve. Typical electrons of interest in XPS have energies ranging from ~10-1500 eV corresponding to mean free paths of ~1nm. Image from wikipedia[64] 38

Figure V-7 Hi-Res XPS spectra of a silicon sample after a buffered hydrofluoric etch which yields a hydrogen terminated Si surface (left), and the same sample after an in-situ Ozone clean which has resulted in silicon oxides on the surface (right). 39

Figure V-8 Schematic of a typical STM experimental setup. A bias is applied between the tip and the sample and the tunneling current between the two is used in a feedback loop to maintain a constant tip sample separation. As the tip is moved across the sample surface the variations in height needed to maintain a constant tunneling current are recorded forming a topo graph of the surface. Image reproduced from Wikipedia.[66] 40

Figure VI-1 Survey XPS spectra showing all observed peaks for a sapphire (0001) surface prior to in-situ cleaning, contaminants are observed in the form of F_{1s}, and C_{1s} peaks. 45

Figure VI-2 Carbon and Fluorine 1s peak area plotted as a fraction of Oxygen 1s peak area plotted as a function of annealing temperature in three different oxygen environments; oxygen plasma, ozone, and O_2. 46

Figure VI-3 (Left) Hi-res XPS spectra showing the presence of a high binding energy shoulder on the O_{1s} core level indicative of O-H bonding. (Right) Plot of the O-H shoulder area to O_{1s} peak area as a function of cleaning temperature for several different oxygen environments. 47

Figure VI-4 Hi-res XPS scan of a sapphire(0001) surface annealed to 750°C without the presence of Oxygen. (Left) O_{1s} peak with a Gaussian fit (red) overlapping the experimental data indicating the lack of a high binding energy shoulder, showing that O-H bands have been removed from the surface. (Right) C_{1s} core level indicating the presence of carbon on the surface. 48

Figure VI-5 Hi-res XPS spectra of a (0001) sapphire surface as loaded into the system (red/bottom), after an in-situ ozone clean (purple/top), and after 5-min exposure to air (middle/tan). 50

Figure VI-6 XPS survey scans of Si(001) surface after etching in nanostrip, buffered HF and transportation to the MBE system by various methods. Vacuum Bag corresponds to a vacuum sealer located in the nanofab, DI water indicates the sample was submerged in DI water during transportation, glass and plastic boxes were in atmosphere. 52

Figure VI-7 XPS Survey Scan and Hi-res scans of the C_{1s} and O_{1s} peaks for an epi-ready Si(001) surface annealed in UHV at 850°C. The lack of carbon and oxygen signal indicate low surface coverage of these contaminants. 54

Figure VI-8 AFM and RHEED images of Si(001) surfaces annealed under different conditions. The 650°C annealed surface is a hydrogen terminated surface, the three other annealing temperatures are from epi-ready surfaces with native oxide still present upon loading into the growth system. RHEED of each surface shows the 2x1 reconstruction associated with Si(001) with the exception of the 900°C surface which shows spots indicative of a rough surface. The table shows calculated surface coverage of the pyramidal structures and RMS values of the surface. 55

Figure VI-9 Hi-res XPS spectra of the C_{1s} core level showing the shift in peak position to lower binding energies with the application of a high temperature anneal in the presence of hydrogen or ozone. The solid lines represent the peak positions associated with hydrocarbons and the dashed lines represent the range of energies associated with SiC bonding. 58

Figure VII-1 Schematic of the MBE system used to grow $RNiO_3$ materials. Shuttered growth from elemental sources was used in an activated oxygen overpressure. 63

Figure VII-2 A model depicting the crystal structure of a $LaAlO_3$ substrate and buffer layer with a $LaNiO_3$ film, monolayers are numbered and each monolayer corresponds to a single shutter operation during growth. 65

Figure VII-3 (a) RHEED images along the [100] direction showing the unreconstructed diffraction pattern of a $LaNiO_3$ film when terminated with a La layer and the 2x reconstruction associated with Ni terminated layers. (b) An XRD 2θ-ω scan showing the (002) reflection of both the $LaAlO_3$ substrate and the $LaNiO_3$ film. (c) Intensity vs time of the specular spot in a RHEED pattern for a $LaNiO_3$ film during growth, intensity is observed to increase on La monolayers and decrease on Ni monolayers 66

Figure VII-4 RHEED images along the [001] direction of the $SrTiO_3$ substrate and 3 unit cell thick films of $LaNiO_3$ grown on an as received $SrTiO_3$ substrate, an annealed $SrTiO_3$ substrate with a stepped surface and a $LaAlO_3$ substrate with a $LaAlO_3$ buffer layer. RHEED of $LaNiO_3$ on an annealed $SrTiO_3$ surface is significantly improved though still shows broader diffraction streaks than that of $LaAlO_3$ buffer substrates. 68

Figure VII-5 (Left) AFM of an annealed $SrTiO_3$ substrate showing the stepped surface consisting of single and double unit cell step heights. (Right) AFM of a 5 unit cell thick $LaNiO_3$ film grown on a stepped $SrTiO_3$ surface a stepped surface is still present indicating continuous film growth. 69

Figure VII-6 XRD of a 30 unit cell thick $LaNiO_3$ film on an annealed $SrTiO_3$ substrate. Thickness fringes surrounding the $LaNiO_3$ peaks are present indicating a sharp high quality interface. No additional phases are observed 70

Figure VII-7 RHEED of $GdNiO_3$ film growth on a $LaAlO_3$ substrate and a $SrLaAlO_4$ substrate. RHEED pattern quickly becomes diffuse indicative of poor crystalline quality and a disordered surface. 71

Figure VII-8 Chart of Formation energies for several rare earth transition metal oxides at temperature of 1100K. The family of $ReNiO_3$ is shown to have a positive heat of formation for all members except for $LaNiO_3$ indicating the increasing difficulty of growing thin films with heavier rare earth elements. Reprinted with permission from A. Kaul, O. Gorbenko, I. Graboy, M. Novojilov, A. Bosak, A. Kamenev, S. Antonov, I. Nikulin, A. Mikhaylov, and M. Kartavtzeva, "Epitaxial Stabilization in Thin Films of Oxides," MRS Proc., vol. 755, no. 6, pp. 4026–4043, 2002.. Copyright 2002 American Chemical Society. 72

Figure VII-9 XRD of the (002) reflection for thin films of $PrNiO_3$ grown on $LaAlO_3$ (left), LSAT (middle), and $SrTiO_3$ (Right) substrates. Black curves are as grown samples without an ex-situ anneal, red curves are from samples after an ex-situ anneal at 700°C for 2 hours. 75

Figure VII-10 Sheet resistance plotted for 30 unit cell thick $PrNiO_3$ films grown on $LaAlO_3$, LSAT, and $SrTiO_3$ substrates. $LaAlO_3$ imparts a compressive strain, while LSAT and $SrTiO_3$ impart tensile strain. (Right) is a blow up of the resistance of $PrNiO_3$ on LSAT highlighting the minima in resistance observed at ~110K. 76

Figure VII-11 (Left) resistivity plotted as a function of temperature for $LaNiO_3$ thin films grown on $LaAlO_3$ substrates of several different thicknesses, a transition from metallic behavior to insulating behavior is observed at a critical thickness of 3 unit cells (UC). (Left) Resistivity vs temperature for $LaNiO_3$ thin films grown on $SrTiO_3$ substrates plotted for several film thicknesses the transition between metallic and insulating behavior is shifted to thicker films between 5-7 unit cells (UC). 77

Figure VII-12 (Right) XPS spectra of a $LaAlO_3$ film, 3 unit cell $LaNiO_3$ film on $LaAlO_3$, and a thick 20 unit cell thick $LaNiO_3$ film. Lines indicate the values used to calculate the band offset. (Left) Diagram illustrating the calculated band offset, and values measured valence to core level spacing. 80

Figure VII-13 (Left) XPS used to calculate the energy loss spectra of $LaAlO_3$, intersection between peak background noise and post peak background increase is shown for the O_{1s} core level. (Right) calculated $LaAlO_3$ bandgap in comparison to previously calculated band offset. 81

Figure VII-14 XPS of the valence band and La 5_p and 5_s orbitals for $LaAlO_3$ buffer layer, 3 unit cell thick $LaNiO_3$ which is insulating, 4 unit cell thick $LaNiO_3$ which is metallic, and 20 unit cell thick $LaNiO_3$ films grown on $LaAlO_3$. Lines are a guide to the eye, and bulk valence band edge is from the 20 unit cell thick film, and not directly measured by a gold standard. No significant suppression of spectral weight occurs at the Fermi level for thin $LaNiO_3$ films. 84

Figure VII-15 XPS of the valence band and La 5_p and 5_s orbitals for $SrTiO_3$, 5 unit cell thick $LaNiO_3$ which is insulating, 7 unit cell thick $LaNiO_3$ which is metallic, and 21 unit cell thick $LaNiO_3$ films grown on $SrTiO_3$. Lines are a guide to the eye, and bulk valence band edge is from the 21 unit cell thick film, and not directly measured by a gold standard. No significant suppression of spectral weight occurs at the Fermi level for thin $LaNiO_3$ films. 85

Figure VII-16 STM image taken at 77K which shows the typical $LaNiO_3$ surface at 3 unit cells for both La and Ni termination and 5 unit cell thick Ni terminated thin films. The Ni terminated 5 unit cell thick film shows a monolayer step parallel to the bottom edge of the frame that corresponds to a height 0.39 nm. RHEED (Bottom Right) shows a streaky pattern for the 5 UC thick film. STS for these surfaces is reported in Figures Figure VII-18 - Figure VII-19 87

Figure VII-17 STS spectra at constant tip height taken at 4K for $LaNiO_3$ films of 3, 5, and 7 UC thicknesses. Band gap for 5 unit cell thick film is calculated by fits to the linear portion of the band edges and

extrapolated to zero, process is illustrated by the dashed lines. The 7 unit cell film corresponds to the onset of conductivity for $LaNiO_3$ on $SrTiO_3$. Spectra have been normalized to conductance at -1 V. 88

Figure VII-18 STS spectra taken with variable tip height at 77K for La and Ni terminated films of 3 unit cells on Nb:$SrTiO_3$, and a Ni terminated 5 unit cell thick film on Nb:$SrTiO_3$. Spectra are the averaged shape of several locations on each surface. Reported band gaps are calculated by fits to the linear region of the band edges. 90

Figure VII-19 Minimum observed band gaps measured via variable tip height STS on $LaNiO_3$ films grown on Nb:$SrTiO_3$ for 3 unit cell thick films with Ni (3 unit cells) and La (3.5 unit cells) termination, and a 5 unit cell thick film with Ni termination. Band gaps are calculated by fits to the linear region of the band edges. 91

Figure VII-20 XRD scans of the (002) reflection for superlattice structures with 3 and 5 superlattice repeats. A single superlattice layer consists of 5 unit cells of $LaNiO_3$ and 5 unit cells of $LaAlO_3$. Films were grown on $LaAlO_3$ substrates. Fringes correspond to the superlattice period, with the smaller fringes of the 5 repeat sample are thickness fringes for individual layers. 93

Figure VII-21 STEM of a $LaNiO_3$/$LaAlO_3$ superlattice structure along the [100]. $LaAlO_3$ layers are 10 unit cells thick while $LaNiO_3$ layers are 5 unit cells thick. The topmost $LaNiO_3$ layer, indicated by the arrow, of the film shows two atomic lattices offset by a unit cell vector of (½,½,½). 94

Figure VII-22 Resistivity as a function of temperature for $LaNiO_3$/$LaAlO_3$ superlattices with 1, 3, and 5 repeats grown on $LaAlO_3$ substrates. Superlattice layers correspond to a 5 unit cell layer of $LaNiO_3$ and a 5 unit cell layer of $LaAlO_3$. 96

Figure VII-23 Resistivity as a function of temperature for two $LaNiO_3$/$LaAlO_3$ superlattices with 3 superlattice repeats grown on $LaAlO_3$ substrates. The $LaAlO_3$ layer of each superlattice is varied one superlattice has a $LaAlO_3$ layer of 5 unit cells the other 10 unit cells. 97

Figure VII-24 Resistivity as a function of temperature for two $LaNiO_3$/$LaAlO_3$ superlattices with 3 superlattice repeats grown on $LaAlO_3$ substrates. $LaNiO_3$ layer thickness was varied between 2 and 3 unit cells. 3 unit cell thick $LaNiO_3$ layers in a superlattice show a region of metallic behavior despite single layer 3 unit cell thick films of $LaNiO_3$ showing insulating behavior (see Figure VII-11). 98

Figure VIII-1 (a) STM of 0.15 monolayers of ErSb deposited on GaSb(001) surface, -0.3V bias. (b) STS of ErSb nanoparticle, red is GaSb and shows clear gap in density of states, blue is ErSb and is a metallic density of states. 102

Figure VIII-2 STM and line scan of (a) Er0.2Ga0.8Sb(001) surface ErSb particles at base of pits, (b) Er0.25Ga0.75Sb(001) surface ErSb particles at base of pits and (c) Er0.3Ga¬0.7Sb(001) surface ErSb nanowires lie in plane of surface. 104

Figure VIII-3 (a) SEM of Er0.3Ga0.7Sb(001) surface, inset shows a blowup of one of the spiral macrostep features. (b) STM depicting a pair of macrosteps and the changing surface morphology across the terrace between them. Highlighted areas show positions of higher resolution images used to calculate ErSb surface coverage (c) 14% ErSb, (d) 88% ErSb, (e) 70% ErSb, (f) 5% ErSb. 105

Figure VIII-4 HAADF-STEM of Er0.3Ga0.7Sb samples capped with amorphous AlOx. Lighter regions correspond to ErSb nanowires. (a) Image along the [110] direction perpendicular to the long axis of the nanowires. (b) First observable nanoparticles on the surface of the macrostep in (a) ~100nm from the macrostep edge. (c) Image along the [1$\bar{1}$0] direction parallel long axis of nanowires. (d) First observable nanoparticles on the macrostep seen in (c) ~15nm from step edge. TEM done by Stephan Kraemer. 107

Figure VIII-5 ECCI image of a 25nm $Er_{0.3}Ga_{0.7}Sb$ film grown on a GaSb substrate. The only defects with observable strain fields on the sample are misfit dislocations, one of which can be seen in the center of the image. The spiral macrostep structure is not observed on this surface. ECCI performed by Patrick Callahan 109

Figure VIII-6 A macrostep on a 25nm $Er_{0.3}Ga_{0.7}Sb$(001) surface imaged in three different modes, (a) ECCI electron channeling effects hide nanowires within the sample only nanowires lying on the surface are

clearly visible, regions of new growth near the notch feature and macrostep edges are observed to have smaller and less dense nanowires. (b) Backscatter electron image tilted 2.5° out of the channeling condition used for figure (a), nanowires from layers beneath the surface are clearly visible. (c) Secondary electron image showing surface features of the macrostep. ECCI performed by Patrick Callahan. 111

Figure VIII-7 (a) Diagram showing the two surface configurations used in the model. The macrostep on the right is comprised of the GaSb above the nanoparticles (hpit). (b) Plot of equation 2 showing the ratio of surface energies between vertical nanowire and horizontal nanowire surface morphologies. The transition occurs at lower Er concentrations as surface area contribution to a single macrostep increases. The different lines represent different values for the area parameter A. 115

Figure VIII-8 (a) Diagram showing the growth model for Ga adatoms diffusing along the surface. Ga adatoms reflect from the bottom of a macrostep, majority of growth occurs from the top edge of a macrostep, some growth occurs on the leading edge of the macrostep due to the Schwoebel barrier. (b) Ball and stick model showing overgrowth of an ErSb nanoparticle by GaSb. 118

Figure VIII-9 STM of 7.5 nm of $Er_{0.3}Ga_{0.7}Sb(001)$ the beginning of step bunching can be seen. Inset shows ErSb nanoparticles are present one monolayer below the growth plane. 119

Figure VIII-10 STM image showing horizontal nanowires grown at a substrate temperature 480°C. Sample was grown by codeposition of $Er_{0.15}Ga_{0.85}Sb$. STM image taken at 77K with a -2V tip bias. 120

Figure VIII-11 STM topographic images showing 0.15 monolayers of ErSb deposited at a temperature 480°C (a) which shows no embedded growth and a surface coverage of 14.8%, and 520°C (b) which shows the expected embedded growth mode and a surface coverage of 3.7%. 121

Figure VIII-12 STEM image showing ErSb nanowires grown at several varying temperatures with GaSb buffers between each layer. Large embedded growth mode nanowires are observed at all temperature likely due to a decrease in Sb pressure identified after growth. Image taken by Dan Pennachio. 123

Figure VIII-13 STM image showing a GaSb(001) surface with 0.15 monolayers of Er deposited on top of it in an Sb overpressure ~1/10 the Sb overpressure typically used for nanowire growth. The dashed line indicates an estimate for the original position of the GaSb step shown in the image, growth is thought to have occurred from ejected Ga atoms. 125

Figure VIII-14 STM topographic image of the nanofilament growth mode observed during codeposition of $Er_{0.3}Ga_{0.7}Sb$ at a substrate temperature of 480°C. (Inset) a to scale STM image of one of the smallest nanoparticles observed in the embedded growth regime. 126

Figure XI-1 AFM micrographs showing (left) an as received CMP sapphire (0001) surface and (right) a sapphire (0001) surface annealed in air at 1050°C for 30 minutes. Step height of the right micrograph correspond to single monolayers with a thickness of 0.22 nm. 145

Figure XI-2 RHEED images along the [1000] for sapphire grown by oxidation of elemental Al at several different substrate temperatures. Three regimes are shown corresponding to amorphous, 3D, and Al adatom sticking coefficient of $<<1$. 148

Figure XI-3 RHEED images along the [1000] showing (a) typical initial substrate diffraction, (b) ~400 nm of Al_2O_3 deposited at a substrate temperature of 900°C, and (c) 80 nm of Al_2O_3 deposited at a substrate temperature of 1200°C. 149

Figure XI-4 RHEED along the [1000] direction of sapphire surface grown at 1200°C with and without an oxidizing environment present during high temperatures. (Left) Images of the starting substrate before growth (Right) images corresponding to samples after 80 nm of Al_2O_3 deposition. 150

Figure XI-5 Triple axis XRD scan of the (0006) peak for a sapphire substrate before growth and the same sample after deposition of 80nm of sapphire at 1200°C. 151

Figure XI-6 AFM of an 80 nm Sapphire film deposited at 1200°C in an Ozone overpressure. 152

Figure XI-7 RHEED of Al grown on a (0001) sapphire surface grown by in-situ e-gun deposition for two different substrate temperatures. 25°C samples shows rings indicative of a polycrystalline film. 152

Figure XII-1 Approximate surface reconstruction phase diagram as a function of temperature and bulk Ti composition. Points represent experimental observations. Figure courtesy of Anthony Rice. 155

Figure XII-2 (a-c) STM images of c(2x2) ($NiTi_{0.97}Sn_{1.03}$), (2x1) (NiTiSn) and c(2x4) ($NiTi_{1.01}Sn_{0.99}$) surfaces showing filled states at 77K using a W tip with a bias of -0.5V and a tunneling current of 30 pA, (d-f) Depth profiles of the corresponding surfaces to surface above, with dotted lines marking where depth profiles were taken, and solid squares highlighting surface unit cells. The c(2x4) and (2x1) surface also showed domains rotated 90° relative to those shown. 156

Figure XII-3 a)STM of a full-Heusler surface showing filled states at 77K using a W tip with a bias of -0.5V and a tunneling current of 30 pA and b) step profiles taken along dotted line in 8a. Other terraces on the surface showed similar rows rotated 90°. 157

Figure XII-4 Ball-and-stick models for a) c(2x2) ($NiTi_{0.97}Sn_{1.03}$), b) (2x1) (NiTiSn), c) c(2x4) ($NiTi_{1.01}Sn_{0.99}$ at low T) and d) fH (Ni_2TiSn). Figure courtesy of Anthony Rice. 158

Figure XII-5 (a) Diagram of the sample structure used for STM measurements. (b) Image of the PtLuSb surface at 4k and a bias of -0.5V. (c) blowup of the dominant surface reconstruction observed for the PtLuSb surface. 159

Figure XII-6 STM images of the surfaces for $Au_xPt_{1-x}LuSb$ samples where x = 1/8, ¼, and 3/8. Unlike PtLuSb consistent surface reconstructions were not observed and samples were significantly rougher. 160

Figure XII-7 (Left) Variable tip height STS measurements for various compositions of $Au_xPt_{1-x}LuSb$, STS spectra are vertically offset from each other. A consistent pair of peaks is observable across all samples in the valence band showing a shift with Au composition, no such consistent feature is present in the conduction band. (Right) linear fit of the position of the pair of peaks in the valence band to sample composition. 161

I. Introduction

"The interface is the device" this statement was made by Prof. Herb Kroemer in his Nobel acceptance speech[1]. At the time Prof. Kroemer was referencing the role of heteroepitaxy in band gap engineering and the myriad number of devices enabled by it. However, the statement is if anything more far reaching than originally intended. Even when the actual device is not explicitly dependent on the interface we find that the structure or electronic properties often are dependent on interface or surface effects. This thesis will examine three differing material systems that while seemingly unrelated are united by the critical role that the surface and or interface plays in their resulting structure, operation or growth.

Superconducting coplanar wave guides, one of the leading technologies for realizing a quantum computer, have loss mechanisms dominated by surface and interface effects. Despite the relatively familiar materials used in their manufacture, the material defects of interest may be fundamentally different from the electronically active defects explored by the semiconducting community at large over the last 60 years. Surface characterization will be shown to play a fundamental role in identifying and mitigating the presence of loss mechanisms in the fabrication of qubits.

The metal to insulator transition seen in rare earth nickelate ($RNiO_3$) perovskites is found to vary widely from bulk properties when observed in thin films near interfaces. A thickness dependent metal to insulator transition is observed for films of only a few unit cells in thickness. Understanding the behavior in these films near the substrate film interface is critical as many of the experiments in literature are performed on samples

where conduction is occurring in proximity to this interface, and proposed applications are reliant on heterostructures.

$Er_xGa_{1-x}Sb$ is a model system for exploring the mechanisms behind self-assembly of a wide range of nanostructures. The formation of nanowire structures in $Er_xGa_{1-x}Sb$ will be shown to be governed by surface morphology during the growth process.

Through the analysis of these three material systems the importance of contaminants at interfaces, the control of material properties via interfaces, and the control of surface morphology on material growth will be explored. This thesis will introduce the background of these material systems in chapters II-IV followed by an introduction of the growth and in-situ measurement techniques used in chapter V. Chapter VI will examine the contaminants and chemical bonding observed at the interface used in quantum computing structures. Chapter VII will examine the nature of the thin film metal to insulator transition observed in rare earth nickelates and the role interfaces have on material properties. Chapter IX will examine the mechanisms behind formation of in-plane ErSb nanowires during codeposition of ErSb & GaSb.

II. Superconducting resonators and qubits

A. What is a qubit?

The area of quantum computing is currently an intense area of research. The primary drive for this is that quantum computers are predicted to be much more efficient at specific types of computational problems. The most famous example being Shor's algorithm which is used to factor large numbers. Applications for quantum computers range from modeling of quantum systems to national security applications in cryptography.

A quantum computer differs from a regular computer by the composition of its logical components. A quantum computer is composed of qubits, while a normal computer is formed by bits. A bit is formed from a transistor and is capable of being in one of two states, an on or an off state. A qubit is similar, it has two potential energy levels, a ground state and an excited state. The difference between a bit and a qubit is that the two states in the qubit must be quantum states which enables the qubit to take either the ground state, $|0\rangle$, it's first excited state, $|1\rangle$, or any superposition of the two. The very nature of a qubit means it must be built from something exhibiting quantum mechanical behavior typical choices include; energy levels of a single atom,[2] superconducting circuits,[3] spin up and spin downs states of a nuclear or electronic spin,[4] and energy levels in a quantum dot.[5] This brings its own set of challenges as the energy spacing between levels in a quantum system is typically quite small, requiring measurements at millikelvin temperatures and introducing errors in qubits due to energy fluctuations. In comparison bits operate and are stable at room temperature.

The state of a qubit can be shown in the form of the Bloch sphere, Figure II-1. On the Bloch sphere Z position represents the energy state of the qubit, with the ground state and excited state each corresponding to one of the poles. The qubit may occupy either of these positons or a position in between the two which represents a superposition of the |0> and |1> states, position along the equator represents the phase of the qubit.

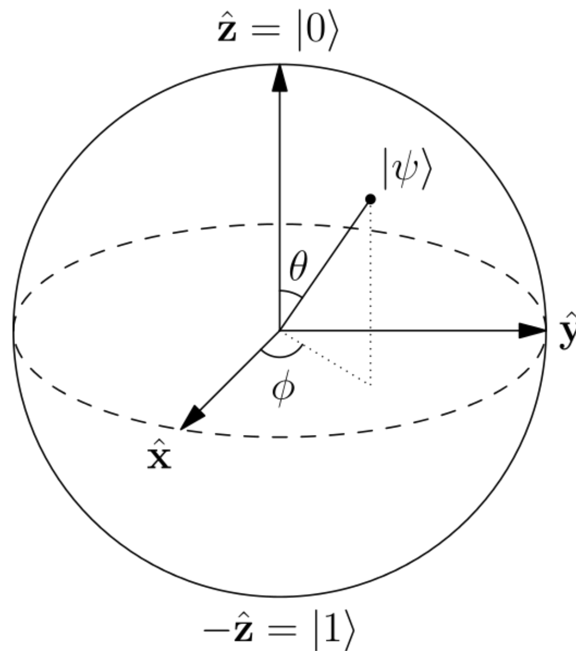

Figure II-1A bloch sphere representation illustrating the possible states of a qubit the Z axis represents the energy level of the qubit while the x and y plane represents the phase. By Glosser.ca (Own work) [CC BY-SA 3.0 (http://creativecommons.org/licenses/by-sa/3.0)], via Wikimedia Commons [135]

B. Decoherence in qubits

Coherence is a measure of qubit lifetime, or once a qubit is set in a specific state how long it takes before interactions with the environment change the initialized state. The bare minimum requirement is that the coherence time of a qubit be longer than the time required to perform an operation. Typical coherence times for qubits based on superconducting circuits are on the order of 10's of microseconds (resulting in a gate

fidelity of ~99.5%), this is in stark contrast to classical computing where bit states are stable for thousands of years. This problem can be alleviated through clever design and implementation of error correction, for example with the surface code.[6] The surface code works by creating networks of physical qubits that together make up one logical qubit, the resulting logical qubit has a fidelity that scales exponentially with the number of physical qubits used in the array. However, even assuming surface code implementation and an improvement of gate fidelity to ~99.95%, implementing Shor's algorithm to factor a 2000 bit number (10^{600}) would require roughly a billion physical qubits.[6] Such large numbers of qubits are quite challenging to implement as they must be operated at milikelvin temperatures. Thus, one of the most pressing challenges is improvement of physical qubit coherence times to enable surface code implementation at reasonable qubit quantities.

Decoherence in qubits encompasses two types of errors relaxation, and dephasing. A relaxation error occurs when the energy state of the qubit changes, on the Bloch sphere this corresponds with a shift in the Z direction towards/away from the spheres poles. The second type of error is a dephasing error and on the Bloch sphere is shown by a change in the plane of the equator. One of the primary loss mechanisms in qubits is through two level states (TLS) which result in relaxation errors.

C. The xmon qubit and two level states

Superconducting coplanar waveguides are of the leading physical systems for qubit fabrication. Superconducting coplanar waveguides have many advantages including the ability for top down processing, where features are defined

lithographically, an advantage over many other physical qubit systems which rely on positioning of single atoms,[4] or elaborate nanowire structures.[7] A comprehensive analysis of the state of superconducting qubits is beyond the scope of this thesis, this chapter will instead bypass much of the theory and history responsible for the current state of the art designs and focus instead on the materials problem of qubit decoherence resulting from two level systems (TLS).

In reality a qubit requires several features to be useful for quantum computing; it must be able to interact with a readout line so the state of the qubit can be queried, it must have control lines so that the state may be manipulated allowing the qubit to be brought into and out of frequency with other elements, and it must be able to interact with other nearby qubits.[8] Figure II-2 shows an optical micrograph of a superconducting qubit and how these features may be implemented.[8] The qubit itself is the cross feature located in the bottom right of the micrograph, it is a superconducting waveguide and the ground state and first excited state of the waveguide (which resembles a harmonic oscillator) comprise the qubit. The Josephon junction highlighted in the blowup is required to change the energy spacing from the equally spaced levels seen in a harmonic oscillator to a non-linear spacing enabling specific addressing of two individual levels to be used as a qubit. The neighboring features are capacitive coupled to the qubit and are composed of; readout by a superconducting resonator connecting the qubit to the readout line (top), a separate resonator acting as a quantum bus so neighboring qubits may interact (right), z control of the qubit states (bottom), and XY control of the qubit states (left). Many of the loss mechanisms present in this system are

shared by both the qubit and the various control and readout resonators, for this reason the quality factor of resonators, similar to the readout resonator depicted in Figure II-2(a), are used as benchmarks for comparing different materials and processes as this skips the time and money intensive process of ebeam lithography needed to define the Josephon junction.

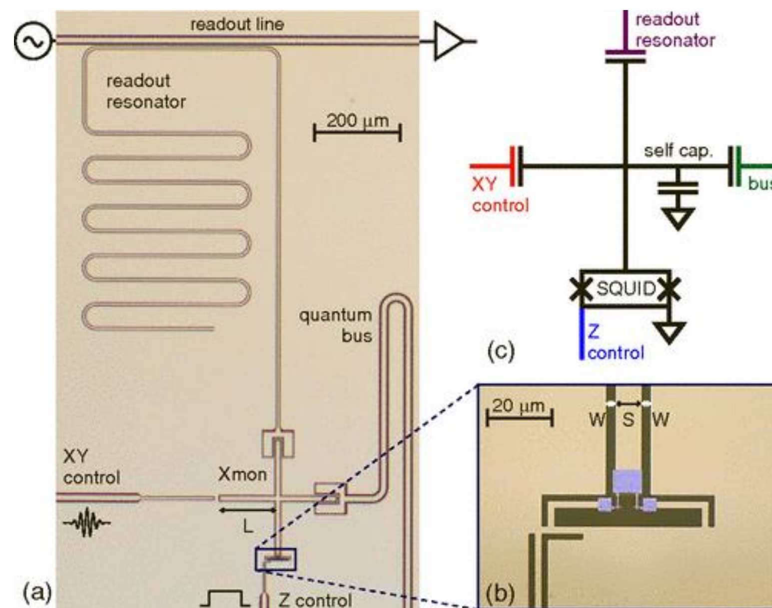

Figure II-2 (a) An Xmon qubit surrounded by the control and readout circuit elements, the Xmon is the crossed shaped capacitor in the bottom right, and the SQUID loop (b), Josephson junctions highlighted in blue. (c) Diagram of the qubit and surrounding circuit elements. Reprinted figure with permission R. Barends, J. Kelly, A. Megrant, D. Sank, E. Jeffrey, Y. Chen, Y. Yin, B. Chiaro, J. Mutus, C. Neill, P. O'Malley, P. Roushan, J. Wenner, T. C. White, A. N. Cleland, and J. M. Martinis, "Coherent josephson qubit suitable for scalable quantum integrated circuits," Phys. Rev. Lett., vol. 111, no. 8, pp. 1–5, 2013. Copyright 2017 by the American Physical Society.

In contrast to the microwave engineering needed the materials engineering of the heterostructure appears to be almost trivial, the entirety of the device is formed by a superconducting thin film on a dielectric, with the various features defined lithographically. However, the previously mentioned TLS are the limiting factor of coherence time in these qubits, and attempting to identify and control their source is where the material science challenge lies in this field. The TLS theory currently used by

the qubit community was developed in the 1970's as a way to describe the low temperature anomaly observed in heat capacity for amorphous materials.[9]–[11] Theory defines a two level state as anything that takes the form of a double potential well with energy spacing between the two states of ΔE, see Figure II-3. If a TLS has ΔE on the order of the energy spacing between $|0\rangle$ and $|1\rangle$ of the qubit it is possible for the qubit to lose energy to excite the TLS. Overtime the TLS can relax back to its ground state by emission of a phonon allowing it to interact with the qubit once more. This process results in a relaxation error with the qubit as the initial state initialized by the user is no longer present.

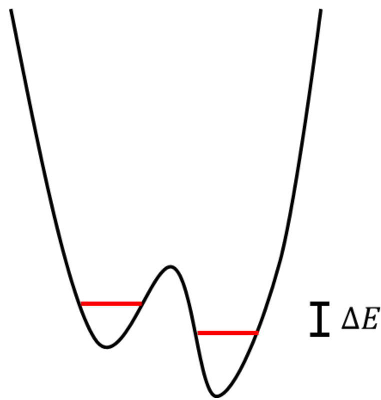

Figure II-3 Schematic of the double potential well of a two level state. If the energy spacing between the two levels is similar to that of qubit interactions may occur.

While TLS theory explains the behavior of resonators at low temperatures the microscopic mechanism that gives rise to the TLS is not known. The most common explanation given in the literature is tunneling of atoms between two configurations, but other mechanisms including polarons[12], hydrogen defects[13] and tunneling of electrons to trap states[14], [15] have been put forward. All of these possible

explanations require the microscopic TLS mechanism to be located in a disordered local environment to create the energy splitting between the two local minima of the double potential.

Typically TLS are assumed to be located in an amorphous oxide region, in a superconducting qubit structure this would correspond to the native oxide layer of the superconductor formed when exposed to air, or the oxide layer of the Josephon junction, and indeed for some time these were the areas of focus. However, a more beneficial method of thinking about the presence of TLS is in the form of participation ratios. Since the TLS must in some way couple to the electric field generated by the superconducting waveguide the positional dependence of said electric field implies that the coupling of a TLS to the qubit will also be heavily position dependent. Figure II-4 shows the participation ratios for the different interfaces present in a coplanar waveguide as modeled by a finite element analysis of the electric fields.[16] Analysis of this model reveals that TLS's located at the metal-air and metal-substrate interfaces have a participation ratio two orders of magnitude larger than those in the surface oxide interface, this result implies that even if there are fewer TLS states at the metal-substrate interface the ones that do form will have a much larger impact on qubit performance than those that exist at the metal-air surface. The participation ratio's calculated for the corner, and substrate-air interfaces can be further reduced by altering the geometry of the waveguides to include an etched trench into the substrate, eliminating the 90° corner.[16] The only surface participation ratio not significantly altered by geometry effects is the metal-substrate interface, and a different method of limiting TLS at this interface is required.[16]

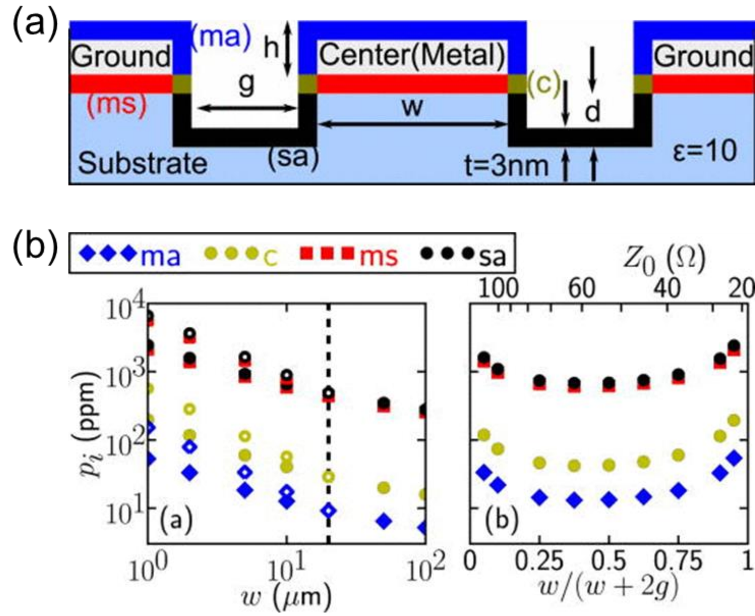

Figure II-4 (a) cross sectional view of a coplanar waveguide depicting dimensions and interfaces. (b) Participation ratios of the different interfaces present in a coplanar waveguide as a function of geometry. Reprinted from J. Wenner, R. Barends, R. C. Bialczak, Y. Chen, J. Kelly, E. Lucero, M. Mariantoni, A. Megrant, P. J. J. O'Malley, D. Sank, A. Vainsencher, H. Wang, T. C. White, Y. Yin, J. Zhao, A. N. Cleland, and J. M. Martinis, "Surface loss simulations of superconducting coplanar waveguide resonators," Appl. Phys. Lett., vol. 99, no. 11, pp. 2009–2012, 2011., with the permission of AIP Publishing.

The effect of the metal-substrate interface is seen experimentally when observing the quality factor of SCW's as a function of growth process, Figure II-5.[17] The quality factor of all the resonators increases with increasing photon density, a feature indicative of TLS losses from interfaces dominating at low power, with TLS saturation occurring as photon density increases.[18] The change in internal quality factor for the various growth processes is therefore ascribed to the differences in interfacial quality at the metal-substrate interface, identical processing was used so nominally the metal-air and substrate-air interfaces are identical across all devices.

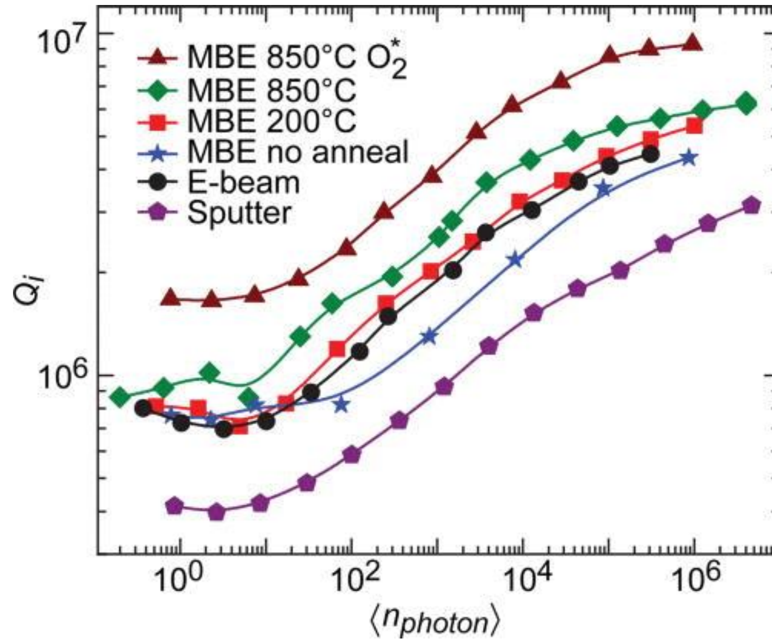

Figure II-5 Power dependence of the internal quality factor Qi versus average photon number in the resonator <n_{photon}>, for resonators with w =15μm. Lines are guides to the eye. The typical low-power statistical error from a least-squares fit of Eq. (3) is ~3%, smaller than the symbol size. Reprinted from A. Megrant, C. Neill, R. Barends, B. Chiaro, Y. Chen, L. Feigl, J. Kelly, E. Lucero, M. Mariantoni, P. J. J. O'Malley, D. Sank, A. Vainsencher, J. Wenner, T. C. White, Y. Yin, J. Zhao, C. J. Palmstrøm, J. M. Martinis, and A. N. Cleland, "Planar superconducting resonators with internal quality factors above one million," Appl. Phys. Lett., vol. 100, no. 11, 2012., with the permission of AIP Publishing.

The resonators shown in Figure II-5 were all fabricated from a 100nm thick layer of Aluminum on c-plane sapphire. All sapphire wafers had the same initial treatment of Acetone, Isopropanol and DI-water rinses before being loaded into the growth system. Samples grown via e-beam and sputtering were subjected to an ion mill before Al deposition, while MBE samples were subjected to a 200°C outgassing anneal in the load lock, followed by either no further anneal, a high temperature anneal of 850°C in the growth chamber, or a high temperature 850°C anneal in an O_2^* (oxygen plasma) with a background pressure of 10^{-6} torr. The background pressure in the various deposition chambers was $6x10^{-8}$ for the e-beam, and sputtered films, and $5x10^{-10}$ for the MBE grown films, it should be noted that the MBE environment here refers to films grown by e-beam

deposition of Al in an MBE chamber with the associated UHV conditions and cryoshield, and not the typical MBE growth method of thermal evaporation from an effusion cell.

The results of this experiment show that there must exist a materials explanation for the difference in resonator quality for the different growth techniques. However, beyond the simplistic view of MBE growth being in a cleaner environment and resulting in fewer TLS there exists no specific hypothesis for the source of this effect. The goal of the work presented in chapter VI is to establish an understanding of the specific physical effects that the MBE cleaning methods have on the interface that may result in fewer TLS, and to develop processes that may improve on them.

III. Metal to insulator transition of rare earth nickelates

A. Perovskite structure

Recently, perovskite oxides and their related phases have been a constant source of new and exciting physics not seen in other materials systems. These include properties such as, high temperature super conductivity,[19] magnetism,[20], [21] metal to insulator transitions and 2D electron gasses,[22], [23] sometimes with more than one of these in the same material. In addition, since all of these materials nominally share a similar crystal structure, it opens the possibility that interesting heterostructures combining these various properties may be accessible.

Perovskite materials are of the chemical form ABX_3. The crystal structure for a perovskite is shown in Figure III-1 for the material $LaNiO_3$. The crystal structure is commonly thought of in the form of oxygen octahedral around the B site atoms, for the $LaNiO_3$ example these would be the Ni-O octahedral, and it is these bonds that dominate many of the electronic properties. Not shown in Figure III-1 are the possible distortions and tilts between atoms present in many of the $RNiO_3$ materials in particular the bond angles between oxygen octahedra are thought to play a critical role in electronic properties of the materials, these distortions are affected by the size of the R ion with smaller ions leading to larger distortions.[24]

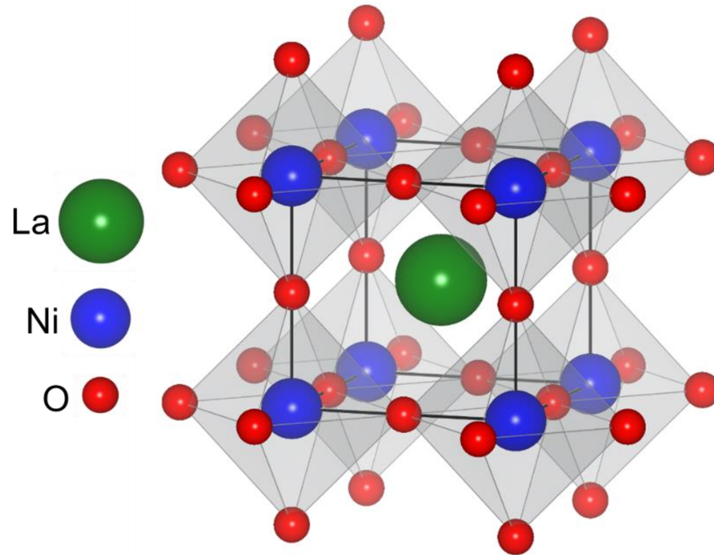

Figure III-1Crystal structure of a cubic perovskite material, atom positions are labeled as would be expected for $LaNiO_3$. Octahedra are drawn showing the Ni-O bonds which are the dominant conduction pathway in the $RNiO_3$.

The source of most of the new physics in these materials is related to the fact that these oxides are correlated electron materials. A material with correlated electrons implies that electron-electron interactions must be taken into account when predicting bulk behavior. This is in stark contrast to regular semiconductor physics, which follow Bloch theory, and states that electronic band structure can be calculated from the periodic potential of the atom cores in the lattice, but electrons within the crystal do not interact.

B. Metal to insulator transition in $RNiO_3$

Bloch theory makes a straightforward prediction that materials with a completely filled band are insulators, while materials with a less than full band are metals. This is the case for most typical semiconductors, which are insulators with filled bands and the property of interest is the band gap between the filled band and the next empty band. However, Bloch theory is based entirely on the periodic potential of the atomic nuclei

without any electron-electron interactions, an incorrect assumption for many oxide materials.[25] When taking into account the presence of electron-electron interactions new possibilities exist, which result in insulators.

One such possibility is the interaction resulting in Mott-Hubbard and charge-transfer insulators, both of which are closely related.[26] Electron-electron interactions are between two negative charges resulting in a coloumbic repulsive force between them. If we consider the case of a generic partially filled band with any level of filling except for ½, we get the case illustrated in the top of Figure III-2. The figure illustrates movement of an electron from a lattice site to an adjacent lattice site. For the case of a partially filled band, the initial state has two electrons on a single lattice site and the final state also has two electrons on a single lattice site. The energy from the repulsive force between electrons is identical, so there is no barrier to motion of electrons through the crystal structure, resulting in a metal as would be expected by Bloch theory. However, for the case of a band with exactly half filling we get the result shown in the bottom half of Figure III-2, in this situation the starting configuration has electrons equally spaced on all lattice sites, if an electron moves to an adjacent site there now exists a pair of electrons in much closer proximity. This results in an increase in total energy of the configuration of electrons in the system the magnitude of this increase in energy is a quantity labelled as U. The need to give an electron an additional amount of energy U before it can move lattice sites in the crystal results in an effective band gap.

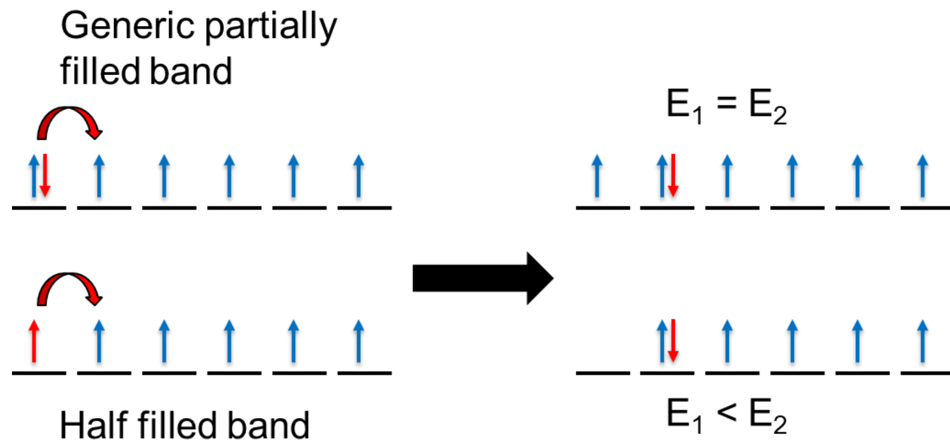

Figure III-2 Illustration of how conduction of charge between lattice sites results in an increase in energy by an amount equal to the repulsion between two electrons for a half-filled band (bottom) while a partially filled band of any other filling results in no net change in energy (top).

The effect of the repulsive term present in a half filled band is illustrated in the band structure shown in Figure III-3, which shows the creation of both a Mott-Hubbard insulator and a charge-transfer insulator. The half-filled band of electrons, shown here as the d-band is metallic by Bloch's theorem. However, once electron-electron interactions are considered the d-band is split by the repulsive term U into two separate bands known as the upper and lower Hubbard bands. For the case of a Mott-Hubbard insulator the material becomes an insulator if the repulsive term in greater than the bandwidth of the upper and lower Hubbard bands, U > 2w. A charge-transfer insulator is formed by the same process, except the lower Hubbard band lies beneath the filled band of another orbital, here shown as the p band. The band gap is now based on the parameter Δ, which represents the energy between the difference between the repulsive term U and the top of the filled p band.

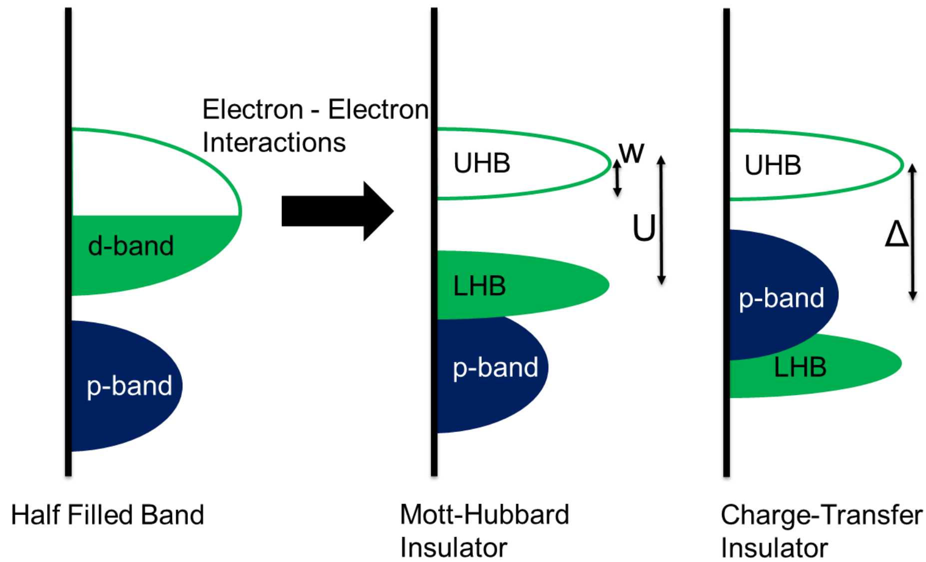

Figure III-3 Diagram illustrating how the electron-electron interactions in a half filled band result in a repulsive force creating an energy splitting (U) between the filled and unfilled states creating an Upper Hubbard Band (UHB) and Lower Hubbard Band (LHB). One of two types of insulators can result a Mott-Hubbard Band where the band gap is between the UHB and LHB, or a charge-transfer insulator where the band gap is between two bands of different character here illustrated as a gap between the d and p bands.

A metal to insulator (MIT) transition is seen when a material changes from metallic behavior (typically seen as decreasing resistivity with decreasing temperature indicating a decrease in scattering due to phonons), to insulating behavior (increasing resistivity with decreasing temperature indicating fewer thermally excited charge carriers) as a function of some parameter. The family of $RNiO_3$, where R can be any rare earth atom, exhibits one such MIT which varies as a function of R. The phase diagram for the $RNiO_3$ MIT is shown in Figure III-4.[24] The transition occurs at a critical temperature above which the material is metallic and below which the material is an insulator. The exception to this is the case of $LaNiO_3$, which is a metal in its bulk crystal at all temperatures.

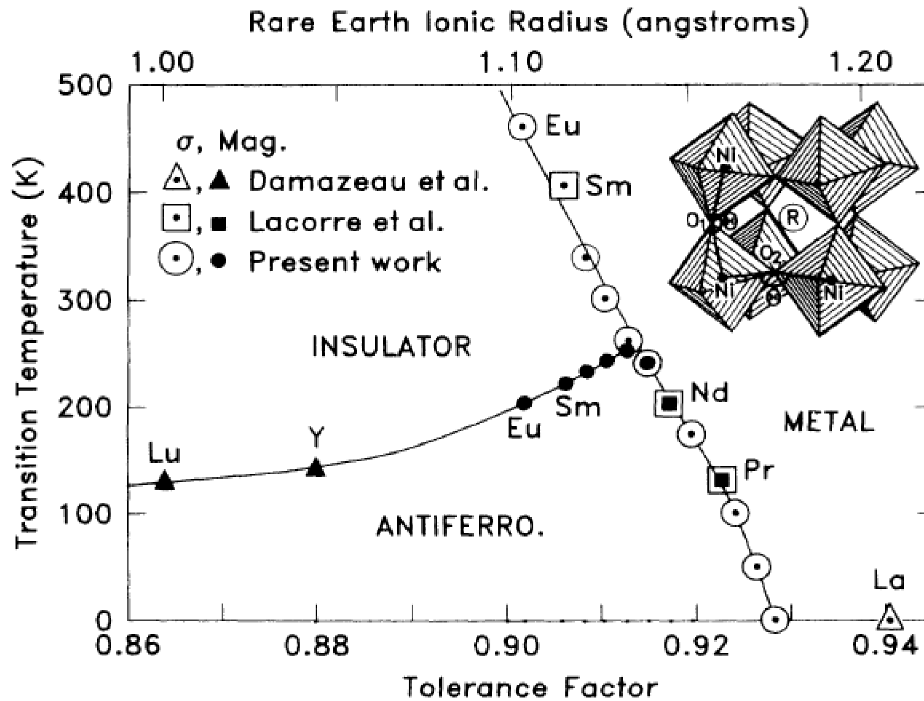

Figure III-4 Phase diagram showing the metal to insulator magnetic transition for the $RNiO_3$ family of materials plotted as a function of rare earth ionic radius and tolerance factor, a measure of the octahedral tilts in the crystal with smaller tolerance factor corresponding to greater tilts. Reprinted figure with permission from J. B. Torrance, P. Lacorre, A. I. Nazzal, E. J. Ansaldo, and C. Niedermayer, "Systematic study of insulator-metal transitions in perovskites RNiO3 (R=Pr,Nd,Sm,Eu) due to closing of charge-transfer gap," Phys. Rev. B, vol. 45, no. 14, pp. 8209–8212, 1992. Copyright 2017 by the American Physical Society.

The MIT in bulk crystals of $RNiO_3$ is still an area of research with multiple explanations present in literature. One explanation attributes the MIT to band width tuning in a charge transfer insulator.[24], [27], [28] In the rare earth nickelates the width of the bands, w in Figure III-3, are heavily dependent on tilts and bond distances of the Ni-O bonds which make up the oxygen octahedral in the crystal structure. For relatively straight bonds (large atomic radii, low Z rare earths) exchange between the Ni-O atoms is large resulting in wide bands and metallic behavior, as tilts between octahedra increase (due to small atomic radii, high Z rare earths) larger bond angles and less exchange between Ni-O atoms results in less dispersion in the bands and a transition to insulating behavior. In the extreme case of $LaNiO_3$ the bandwidth w is always larger than the

repulsive term U, so overlap between the upper Hubbard band and the filled p band is always present and the material is a metal at all temperatures. Other rare earth nickelates are metallic at high temperatures, but as temperature is reduced a decrease in band width means the repulsion term U is enough to separate the upper Hubbard and p bands, this is often accompanied by a phase transition from the orthorhombic pbnm space group to a monoclinic phase $P2_1/n$, creating two individual nickel crystallographic sites and possibly charge ordering as well.[29]

The nature of this insulator implies that if excess charge can be introduced to the material it will be immediately metallic, giving the potential of an extremely efficient transistor.[30] The family of $RNiO_3$ materials is one candidate for the creation of such a device. The Mott material in the device can be supplied by a $RNiO_3$ with a suitably tuned MIT. The insulating gate barrier can be either $LaAlO_3$, or $SrTiO_3$ both perovskite materials with relatively close lattice constants to the $RNiO_3$ with large band gaps. $LaNiO_3$ can form the metallic top gate, this results in an all epitaxial structure as shown in Figure III-5.

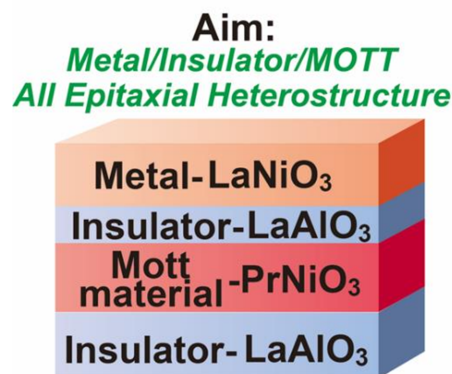

Figure III-5 Schematic diagram of the type of heterostructure theoretically needed to create a Mott based transistor.

Of course this structure is based off the as-measured bulk properties of the materials, so there are often many unforeseen challenges and interactions when constructing a heterostructure, both in the growth of the materials as well as altered properties brought about by the presence of strain and interfaces not present in bulk crystals. Chapter VII will discuss the effects of interfaces on the electronic properties and the MIT observed in thin films of these materials. In particular a MIT observed as a function of film thickness independent of rare earth ion will be examined, and tenability of said MIT will be demonstrated through the use of superlattice heterostructures.

IV. ErSb self-assembled nanostructures

A. Introduction

Spontaneous phase separation resulting in self-assembled nanostructures has been observed in a wide range of materials systems including semiconductors,[31] oxides,[32] metals[33] and polymers.[34] Often these nanostructures show new and desirable properties resulting from asymmetry and orientation,[35] confinement,[36] or increased coupling with a matrix material,[31] making them an exciting area of interest when looking for new material properties. Spinodal decomposition and the resulting microstructures has long been an area of interest in bulk materials,[37] however, many of the nanostructures grown by thin film deposition techniques find the self-assembly of nanostructures dictated by kinetics and surface effects. Understanding the processes governing spontaneous phase separation in a surface dominated regime is imperative to enable engineering of nanostructures during thin film growth.

The rare earth-group V (RE-V)/III-V material system is an ideal test bed for investigating nanostructures formed by spontaneous phase separation. RE-V materials are monopnictides, typically resulting in semimetals. Thin films of these materials were initially studied for use as epitaxial contacts to III-V semiconductors.[38]–[43] One of the primary challenges for this material is defect formation during III-V overgrowth due to the difference in symmetry and bonding of III-V (001) and RE-V (001) surfaces.[44] Due to these complications, research has moved away from complete thin film coverage to structures with embedded RE-V nanoparticles in a III-V matrix. The majority of current research in this area focuses on the ErAs material system where ErAs nanoparticles in a

GaAs or InGaAs matrix have found use in a number of applications, such as photomixers,[45] tunnel junctions,[46] thermoelectrics,[33], [47] and may be used to influence quantum dot formation.[48] Interest has also recently expanded to other similar materials such as TbAs which may form semiconducting nanoparticles,[49] and TbAs/ErAs core-shell nanostructures.[50] All of these applications take advantage of the fact that RE-V materials are well suited to nanoparticle nucleation due to the low solid solubility of Rare-Earths within III-V semiconductors as well as RE-V stability, resistance to diffusion, compatible crystal structures, and lattice matching.[40], [51], [52]

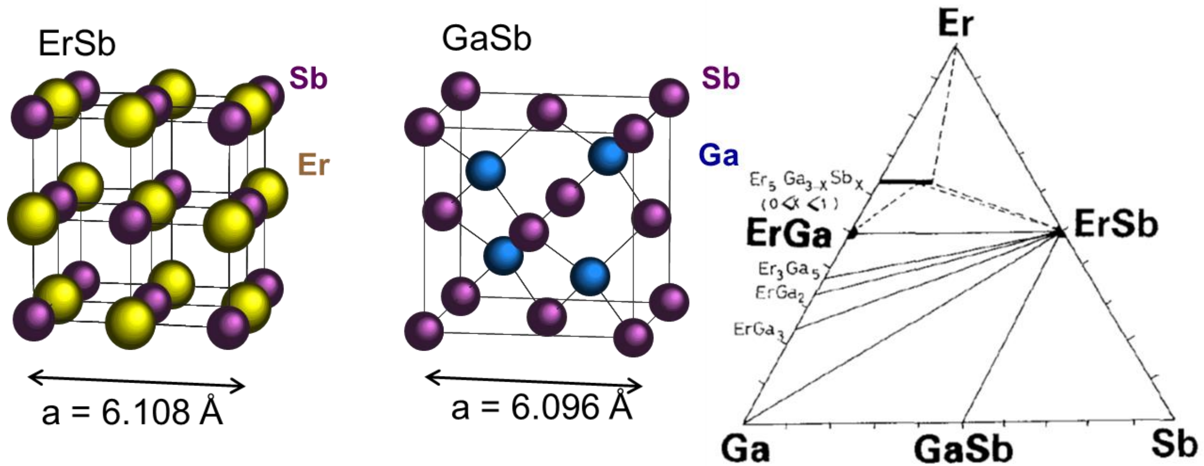

Figure IV-1 (Right) Crystal structures for the rocksalt ErSb and the zincblende GaSb along with lattice parameters. (Left) Ternary phase diagram for the Er-Ga-Sb material system at 800°C, of interest is the tieline between ErSb and GaSb which shows little solid solubility between the two. Ternary phase diagram reprinted with permission from A. Guivarc'h, A. Le Corre, P. Auvray, B. Guenais, J. Caulet, Y. Ballini, R. Gúcrin, S. Députier, M. C. Le Clanche, G. Jézéquel, B. Lépine, A. Quémerais, and D. Sébilleau, "Growth by molecular beam epitaxy of (rare-earth group V element)/III-V semiconductor heterostructures," J. Mater. Res.*, vol. 10, no. 8, pp. 1942–1952, 1995.*

B. Observed nanostructures

The ErSb/GaSb material system studied in this work has exhibited the widest range of different nanostructures seen in a RE-V/III-V material system, including

isotropic nanoparticles, vertical nanowires, horizontal nanowires and nanosheets all of which are accessible by controlling the Er to Ga flux ratio.[53] The formation of nanoparticles and vertical nanowires is explained by an embedded growth mode where Er adatoms replace Ga in the first 3-4 monolayers of the GaSb surface.[53]–[55] ErSb has a lower heat of formation than GaSb which drives a replacement reaction resulting in embedded growth. This combined with the difference in surface energies between GaSb and ErSb, which inhibits GaSb growth on ErSb, results in vertical nanowires.[54] However, this model fails to provide a mechanism for the formation of the stratified layers of horizontal nanowires and nanosheets observed at Er concentrations in excess of 30%.

The range of nanoparticles achievable in the $Er_xGa_{1-x}Sb$ material system was previously explored in the Palmstrøm group by Jason Kawasaki and Brian Schultz.[53] The nanoparticles were observed by TEM and shown in Figure IV-2. The entire sample was grown by codeposition of Er and Ga in an Sb overpressure. The only parameter changed during the growth was the ratio of the Er to Ga flux. As expected by the low solid solubility of Er in GaSb, nanoparticles nucleate almost immediately. At low Er concentrations of ~3% or less the Er takes the form of roughly spherical nanoparticles. As the Er composition is increased to ~5% the morphology of the nanoparticles change and begin forming vertical out-of-plane nanowires. The nanowires are observed to have an octagonal cross section and can be made to branch into multiple nanowires.[53] With continued increase in Er composition to ~25-30%, the out-of-plane nanowires transition to in-plane horizontal nanowires that are oriented along the $[1\bar{1}0]$ crystal direction, which also form in stratified layers with layers of ~5-9nm of pure GaSb between

nanowire containing layers. As Er composition continues to increase to ~50% the in-plane nanowires become nanosheets presumably approaching the regime of complete ErSb layers with continued increase in Er composition.

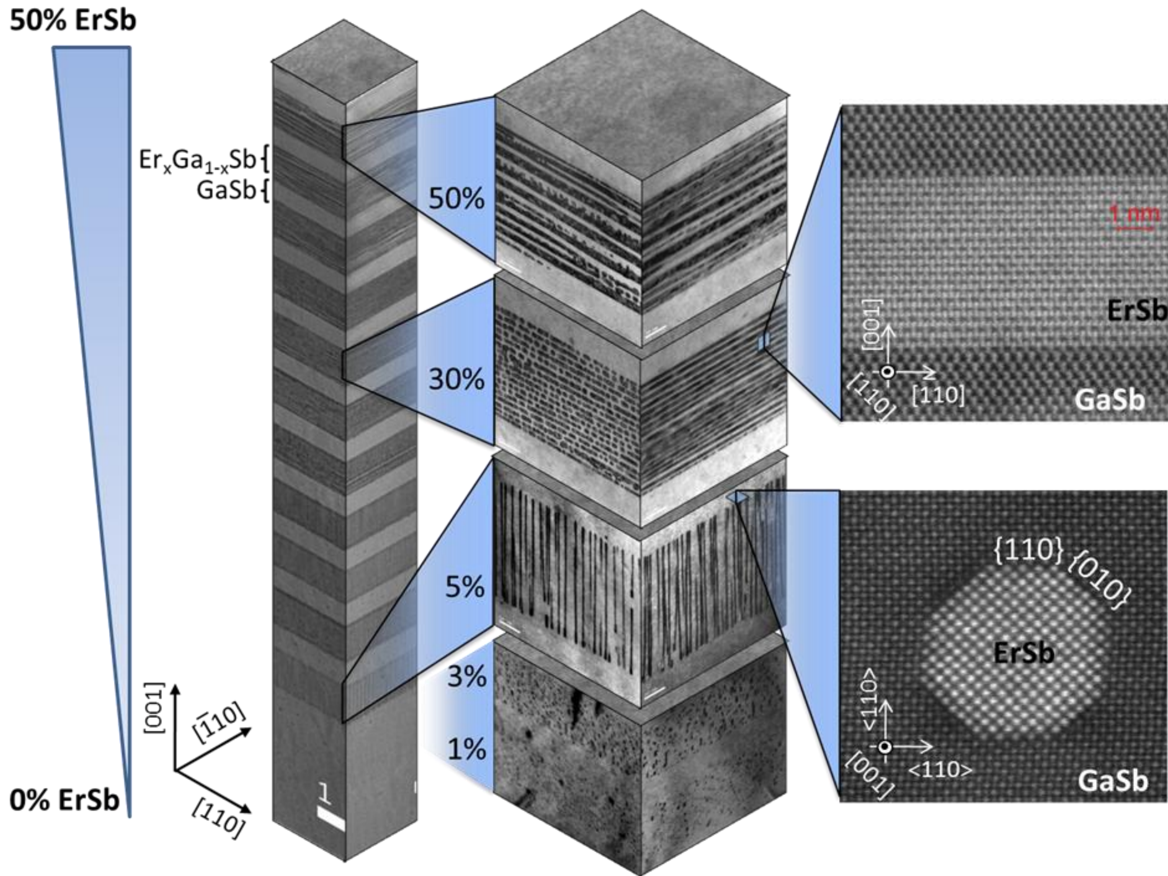

Figure IV-2 TEM image showing the range of self-assembled nanoparticles observed in the $Er_xGa_{1-x}Sb$ material system with variation of the Er composition. At 3% or less ErSb composition isotropic nanoparticles are observed, from ~5% to 30% out-of-plane ErSb nanowires form, 30%-50% in-plane ErSb nanowires form, and >50% sheets of ErSb are observed. Figure created by Jason Kawasaki.

C. Embedded growth mode

The embedded growth mode responsible for nanoparticles and vertical nanowires was well characterized previously. Figure IV-3 illustrates the embedded growth mechanism as observed by STM.[53] The growth process was modeled by first depositing 0.6 monolayers of ErSb on a GaSb surface, Figure IV-3(a), followed by

repeated deposition of 2 monolayers of GaSb until a smooth GaSb surface was recovered. It was observed that ErSb coalesces into particles which are embedded 3 monolayers beneath the surface and extend one monolayer out of the surface, illustrated by the schematics below the STM topographs. Subsequent layers of GaSb initially avoid covering the ErSb islands, instead GaSb grows around the ErSb particles leaving the ErSb exposed in pits. After 4 monolayers of GaSb growth the ErSb particles begin to be covered. Eventually a pristine surface is recovered after 10 monolayers of GaSb growth. This process results in relatively isotropic nanoparticle formation for small concentrations of ErSb.

The behavior of GaSb refusing to wet ErSb is due to the difference in surface energies between GaSb and ErSb, and is the underlying mechanism responsible for out-of-plane nanowire growth. Figure IV-3(b) shows a similar layer by layer study where initially 0.6 monolayers of ErSb was deposited on a GaSb surface, resulting in nanoparticles. Two monolayers of GaSb were then deposited with GaSb growing only on the GaSb and leaving the ErSb particles exposed. Next another 0.6 monolayers of ErSb was deposited, which imitates conditions seen in codeposition of $Er_xGa_{1-x}Sb$. As seen in the STM, ErSb when given the opportunity will grow on top of previously nucleated ErSb nanoparticles. New particles were nucleated only if already present nanoparticles have reached a height of 1 monolayer above the GaSb surface. If this process is repeated with a continual flux of Ga and Er supplied ErSb will continue to preferentially form on the nanoparticles. This results in an elongation of the nanoparticles in the out-of-plane direction and formation of out-of-plane nanowires.

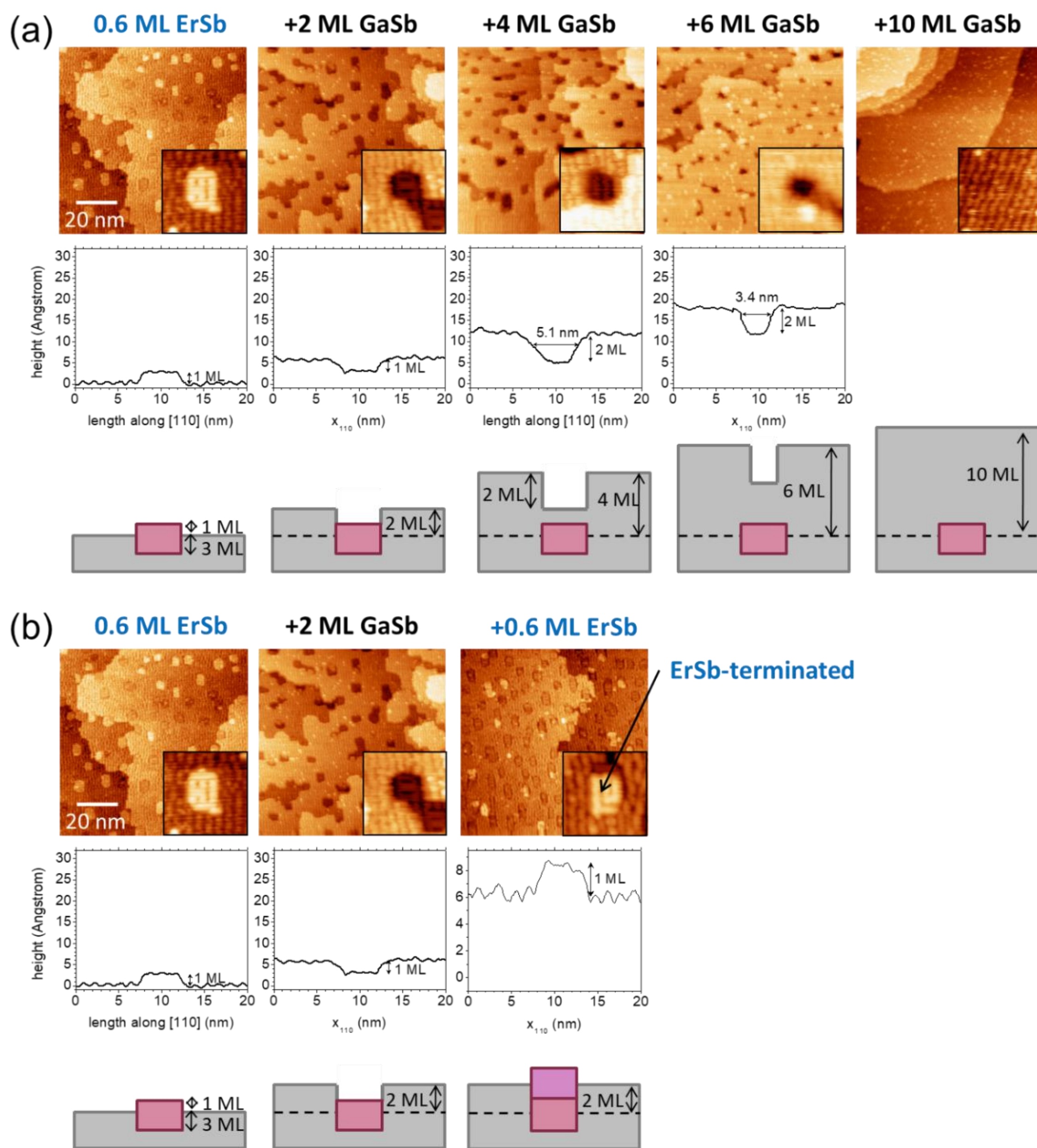

Figure IV-3 STM topographic images, line scans and schematics showing the evolution of the sample surface for (a) ErSb nanoparticles nucleated on a GaSb surface by deposition of 0.6 monolayers of ErSb with continued overgrowth of GaSb in increments of 2 monolayers, and (b) alternative layers of 0.6 monolayers of ErSb and 2 monolayers of GaSb deposited on the sample surface. Reprinted with permission from J. K. Kawasaki, B. D. Schultz, H. Lu, A. C. Gossard, and C. J. Palmstrøm, "Surface-mediated tunable self-assembly of single crystal semimetallic ErSb/GaSb nanocomposite structures," Nano Lett.*, vol. 13, no. 6, pp. 2895–2901 2013. Copyright 2017 American Chemical Society.*

The embedded nanoparticle growth mode gives a straightforward growth process which explains the presence of both nanoparticles and out-of-plane nanowires. The

difficulty comes when examining the structure of the in-plane nanowires. Figure IV-4 shows a composite image of TEM images along the two perpendicular in-plane <110> directions, along with an STM topography image, showing in-plane nanowires for an $Er_{0.3}Ga_{0.7}Sb$ sample. The interesting structure observed with in-plane nanowires is the stratified layers they are observed to form. This results in in-plane ErSb nanowires covered with a layer of pure GaSb, in stark contrast to what would be predicted by the embedded growth process observed for out-of-plane nanowires. The growth mode observed in vertical nanowire formation implies that as long as sufficient Er flux is supplied GaSb should not overgrow ErSb, despite this at higher Er compositions the nanostructures clearly show GaSb overgrowth of ErSb in the form of stratified layers.

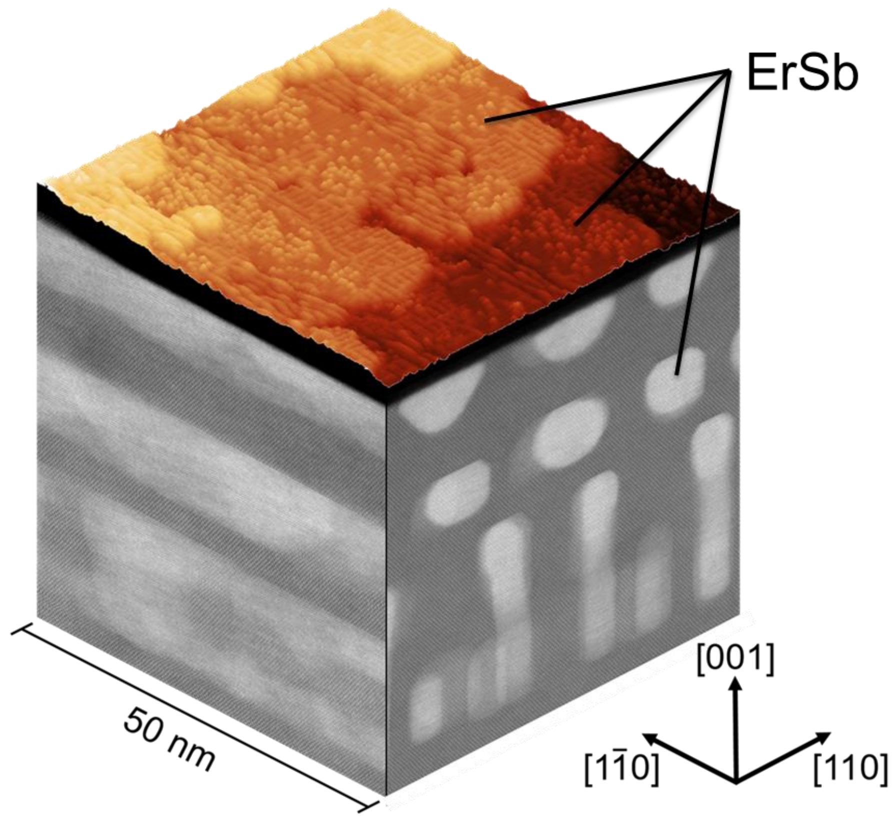

Figure IV-4 Composite image consisting of HAADF-STEM images along the [1$\bar{1}$0] *and* [110] *crystallographic directions, and a 3-D representation of a STM image of the* [001] *growth surface. The out-of-plane component of the STM image is exaggerated compared to the rest of the image for aid in identifying the observed surface reconstructions corresponding to GaSb and ErSb.*

This implies that a different growth mechanism is responsible for in-plane nanowire formation, one that is not well understood. It is important to understand the formation mechanism behind these structures if they are to be incorporated into sensitive device heterostructures. Chapter VIII focuses on developing a theory for the transition from out-of-plane to in-plane nanowires.

V. Experimental techniques

A. Molecular beam epitaxy

Ultimately, a surface or interface is limited by the method used to grow the structure. A wide range of techniques exist for the growth of a crystal on a substrate, of those, Molecular Beam Epitaxy (MBE) is typically viewed as resulting in the most pristine and abrupt interfaces.

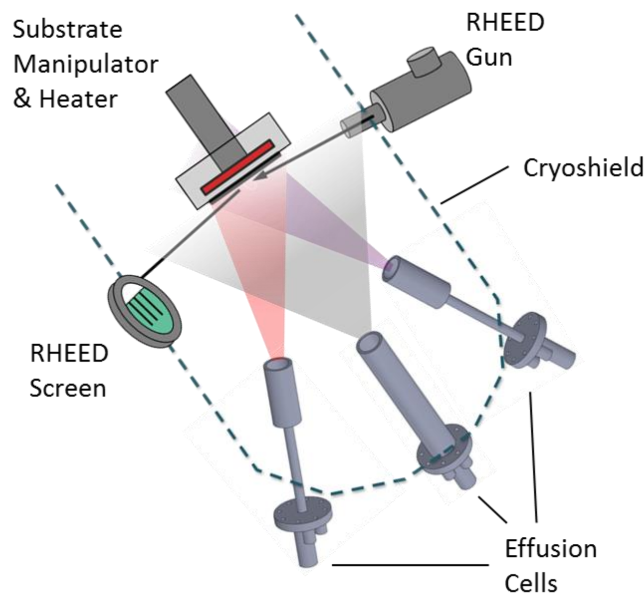

Figure V-1 Schematic of a typical MBE system, effusion cells provide elemental fluxes for film growth, a manipulator allows for substrate rotation and heating during growth. In-situ characterization of the surface is present in the form of reflective high energy electron diffraction. A cryo-panel is present to ensure particles stick to the walls and do not drift onto the substrate.

The molecular beam in MBE refers to the environment within the growth chamber, an MBE system is kept in Ultra High Vacuum (UHV), 10^{-10}-10^{-12} mbar. UHV is used in part to lower the potential contaminants present in the system, and secondly to ensure behavior of a molecular beam, this refers to the mean free path of a particle in

UHV which is on the order of thousands of kilometers, thus an adatom evaporated from an effusion cell will not interact with anything until it reaches the growth substrate, creating a beam of atoms between the effusion cell and substrate. The basic setup of a MBE growth chamber is as seen in Figure V-1 a central substrate manipulator used to heat and rotate the substrate is surrounded by several effusion sources which in typical MBE are comprised of elemental materials in non-reactive crucibles heated by resistive filaments. The sources are heated until a measurable vapor pressure of the material is achieved and growth is controlled via shutters between each individual source and the substrate.

The vapor pressure of a material has very predictable behavior as a function of temperature due to the Arrhenius relationship.

$$P(T) = Ae^{-E_a/k_b T}$$

Where k_b is the Boltzmann constant, E_a is the activation energy required to remove an atom from the bulk in the elemental source either by sublimation or evaporation, and A is a term used to account for geometry effects. The flux of an elemental source can be measured at several different temperatures and the resulting points fit a line on a log scale, this relationship can be used to predict flux at any point within the range of temperatures measured allowing for a level of flux control down to single atomic layers.

The second aspect of MBE is the epitaxy, MBE is not an equilibrium process and through the careful selection of substrate material the atomic lattice of the substrate can be used to aid in formation of a specific phase and crystal orientation of the grown film.

While all of this is important for achieving the highest quality of material possible, an equally important part of MBE when creating precise surfaces and interfaces comes from the in-situ monitoring available in the form of Reflective High Energy Electron Diffraction (RHEED). RHEED offers many insights as to what is occurring on the sample surface in real time during growth. The RHEED system on an MBE chamber consists of a RHEED gun which provides the electron beam and a phosphor screen at the opposite side of the chamber to observe the diffracted electrons, see Figure V-1. The diffraction pattern is the reciprocal of the real space so for an ideal 2-D surface the diffraction condition will result in 1-D rods perpendicular to the sample surface, the intersection between the rods and the e-wald sphere creates the observed diffraction pattern which for a smooth surface results in vertical streaks, or in the case of a very high quality surface with very thin rods a ring of spots. If on the other hand the sample surface is rough the electrons pass through bulk like material resulting in a bulk diffraction pattern consisting of a grid of spots, polycrystalline material results in concentric rings as diffraction though multiple orientations is observed, and amorphous material results in a diffuse background, these possibilities are schematically shown in Figure V-2.[56]–[58]

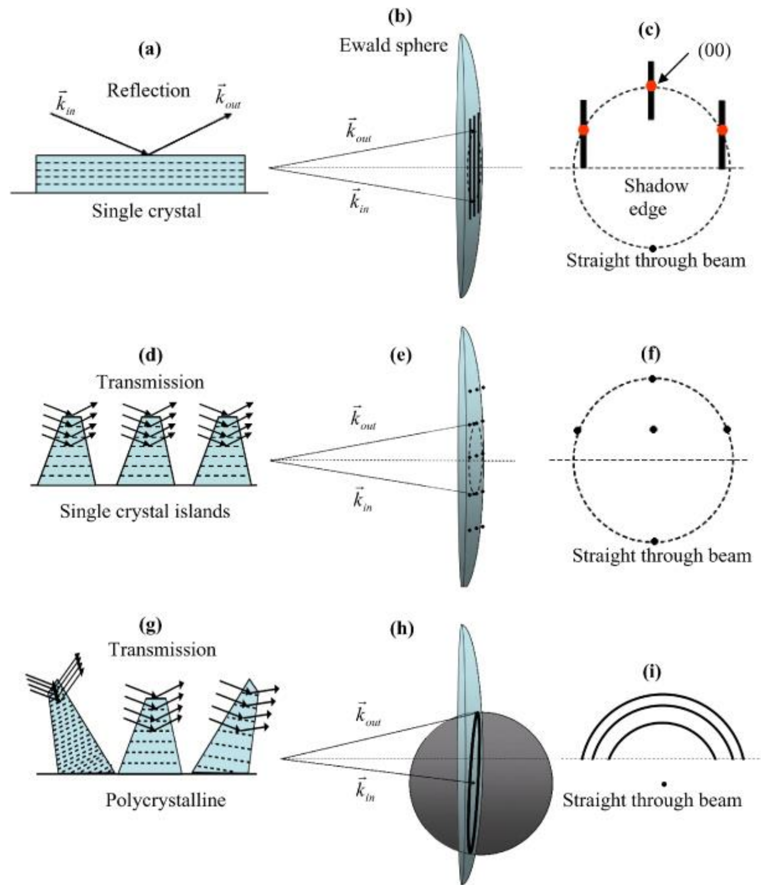

Figure V-2 Diagram showing the crystal surface, the intersection of the ewald sphere with k-space and the observed diffraction pattern for a smooth 2-D surface (a-c), a rough epitaxial surface (d-f) and a polycrystalline surface (g-i). Reprinted with permission from F. Tang, T. Parker, G.-C. Wang, and T.-M. Lu, "Surface texture evolution of polycrystalline and nanostructured films: RHEED surface pole figure analysis," J. Phys. D. Appl. Phys.*, vol. 40, pp. R427–R439, 2007.*

If the periodicity of the surface varies from the periodicity of the bulk unit cell additional streaks are observed in RHEED. The RHEED pattern is in reciprocal space so if the surface periodicity of the cell is doubled the spacing between the observed RHEED streaks is 1/2 the original spacing, likewise if the periodicity is tripled the spacing is 1/3 the original spacing. Surface reconstructions are common in the III-V semiconductors with the reconstruction typically reported in the form of an (A x B) where A is the size of the surface unit cell along the $[1\bar{1}0]$ direction and B is the size along the [110] direction,

this convention varies from material to material for example in the perovskite oxides discussed later the RHEED direction of interest is along the [100]. Surface reconstructions can impart a great deal of knowledge about the sample surface during growth. In III-V's the reconstruction is a function of group V overpressure as well as substrate temperature and entire phase diagrams have been mapped out for this relationship.[59]–[61] Surface reconstructions observed in novel materials grown by MBE such as oxides or the Heusler compounds where a growth window does not exist can provide knowledge about composition of the material and aid in achieving stoichiometric growth as will be seen to be the case for the $RNiO_3$.[62]

In addition to knowledge of the surface periodicity it was also found that when in the layer by layer growth regime the intensity of the RHEED pattern oscillates with a periodicity matching the deposition time of a single monolayer.[58] In layer by layer growth the smooth sample surface is gradually roughened as new monolayers nucleate on the surface, these islands eventually coalesce to form a new pristine surface upon which the process repeats. RHEED is sensitive to this surface roughness and peaks in intensity correspond to the smooth complete monolayers, while minima in intensity correspond to the surface with half a monolayer nucleated on it, as shown in the diagram in Figure V-3[63]. This is an extremely powerful result which allows for immediate feedback of fluxes for k-cells. RHEED oscillations were used to calibrate the fluxes of the sources for growth of $Er_xGa_{1-x}Sb$ discussed later in this work.

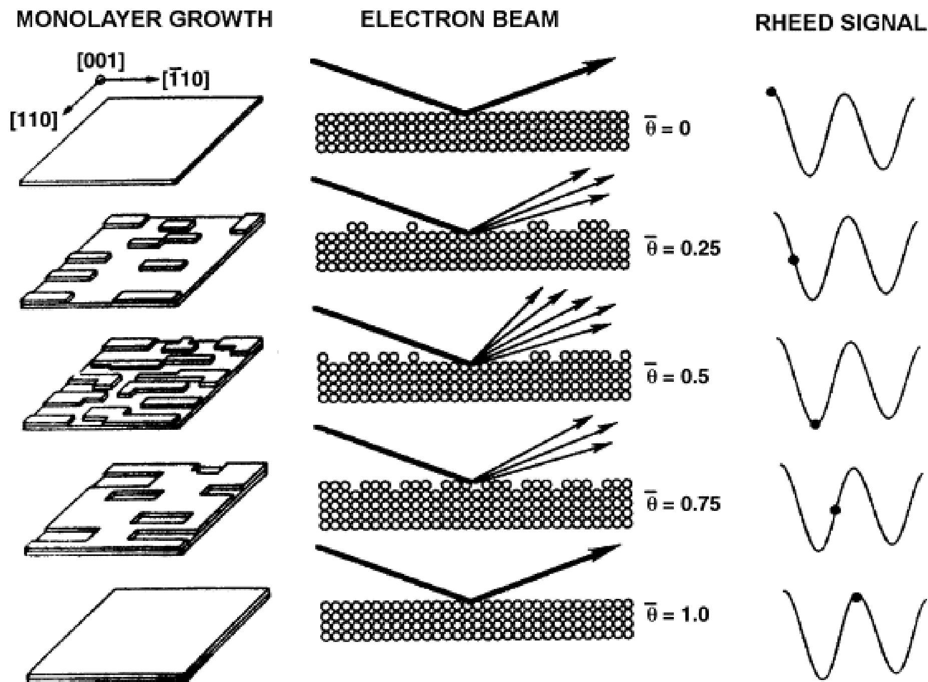

Figure V-3 – Schematic showing the growth of a monolayer on a smooth surface with the corresponding scattering of an electron beam from the increasingly rough surface, and the resulting intensity of the RHEED signal as a function of surface morphology. Reprinted V. P. LaBella, M. R. Krause, Z. Ding, and P. M. Thibado, "Arsenic-rich GaAs(0 0 1) surface structure," Surf. Sci. Rep., vol. 60, no. 1–4, pp. 1–53, 2005 with permission from Elsevier.

Even with monolayer control of thin film growth, surfaces and interfaces remain an extremely challenging aspect of materials science to work on in a large part due to the difficulty of accurately measuring their properties. The difficulties arise from two primary reasons; The first is that a large number of the most powerful techniques in the arsenal of a materials scientist probe a region of the material much larger than the interface, X-ray diffraction probes the bulk of the sample with all regions in the path of the x-rays contributing to the result, scanning electron microscopy has an interaction volume on the order of microns, and electronic measurements may or may not be dominated by interface effects making it difficult to separate them from the bulk properties. The second difficulty is due to contamination of the surface outside of the growth environment, looking at a buried interface is much more difficult than a surface

but the atmosphere, especially oxygen, frequently reacts with the material of interest fundamentally changing the properties at the interface. Even when a material does not oxidize in atmosphere samples once removed from the vacuum system are immediately contaminated by a number of airborne particles including a wide range of hydrocarbons that are immediately visible in techniques such as XPS. To overcome this surface sensitive techniques are frequently paired with some sort of etching process to remove protective layers and measure interfaces underneath, which may damage the sample, or the measurement must be performed without ever breaking vacuum.

It is the second option that the Palmstrøm lab at the UCSB is uniquely suited for, the lab consists of six growth chambers, a III-V MBE system, two Heusler compound growth systems, an oxide/nitride system, a metal organic system, and a chemical beam epitaxy system all connected to each other by UHV. In addition to the RHEED located within each of the growth chambers several surface sensitive measurements are also located in-situ consisting of low energy electron diffraction, auger spectroscopy, x-ray photoemission spectroscopy (XPS), and scanning tunneling microscopy (STM), the latter two of which are heavily utilized in this work.

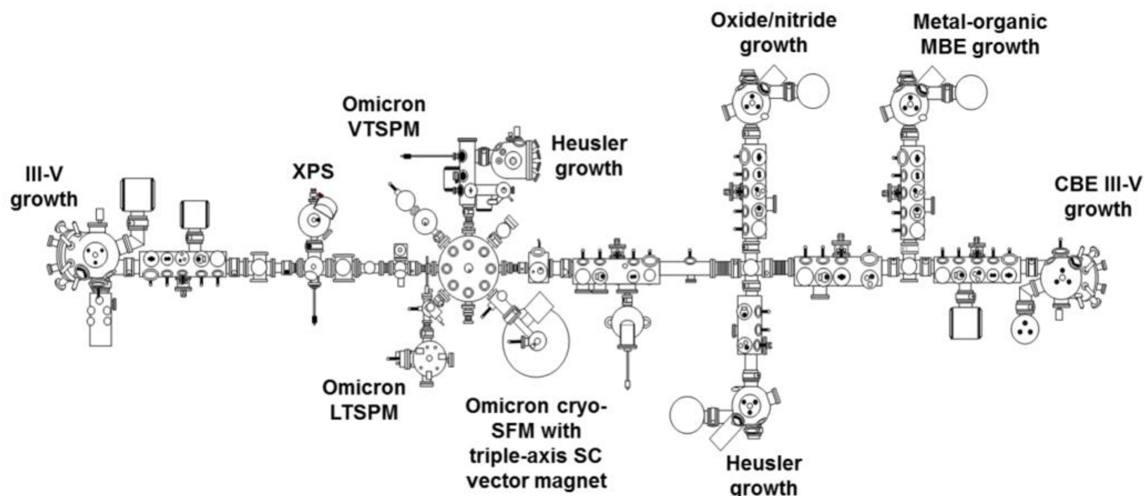

Figure V-4 Diagram of the Palmstrøm MBE lab at the University of California Santa Barbara. The qubit and $RNiO_3$ materials were grown in the Oxide/Nitride chamber while the ErGaSb films were grown in the III-V growth chamber. All films are able to be characterized in-situ with x-ray photoelectron spectroscopy, or scanning tunneling microscopy.

A schematic of the growth system and in-situ characterization equipment is shown in Figure V-4, the samples used in the work on superconducting waveguides and $RNIO_3$ were grown in the oxide system, while the self-assembled RE-V nanostructures were grown in the III-V growth system. All of these samples were capable of in-situ transfer to the XPS system or the low temperature STM.

B. X-ray Photoemission Spectroscopy

XPS is a surface sensitive characterization technique that is capable of providing compositional information, as well as information on the chemical bonding of constituent atoms. XPS makes use of the photoelectric effect where light shined on a sample results in photo emitted electrons. The experimental setup consists of a monochromated x-ray source, and an electron detector capable of measuring the energy of the emitted electrons. The schematic for such a setup can be seen in Figure V-5.

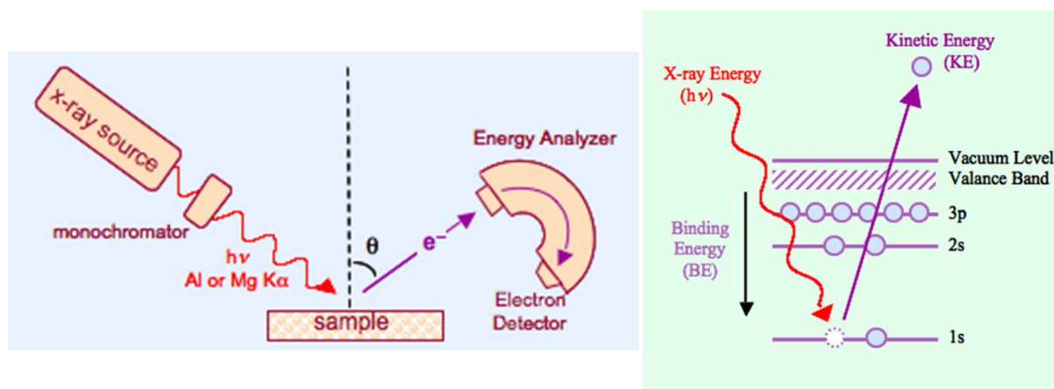

Figure V-5 Cartoon of the experimental setup in XPS (left) and a diagram of the photoemission process (right).

Since the incident x-rays are from a known source, Al for the in-situ detector used in this work, and are monochromated the initial energy of the system is well known with a distribution width of ~0.8 eV. Upon entering the sample the incident x-rays interact with electrons and excite them out of the material, the resulting electrons must conserve energy resulting in the equation

$$KE = hv - BE$$

Where KE is the kinetic energy of the escaped electron, hv is the energy of the incident x-ray and BE is the binding energy of the electron, a schematic of the process is shown on the right side of Figure V-5. From this relationship it is straightforward to calculate the Binding energy of each electron detected. If the sample is not conductive it should be noted that significant charging is likely to occur during the measurement process, the charging of the sample will interact with the charge of the exiting electrons resulting in a shift of the detected binding energies. The experimental setup has a low energy electron flood gun designed to counteract this effect but a shift in binding energy is still expected. This makes it difficult to know the absolute position of core levels or the fermi level

without a standard metallic sample, but the analysis used in this work is primarily concerned with relative spacing between peaks, alleviating this concern.

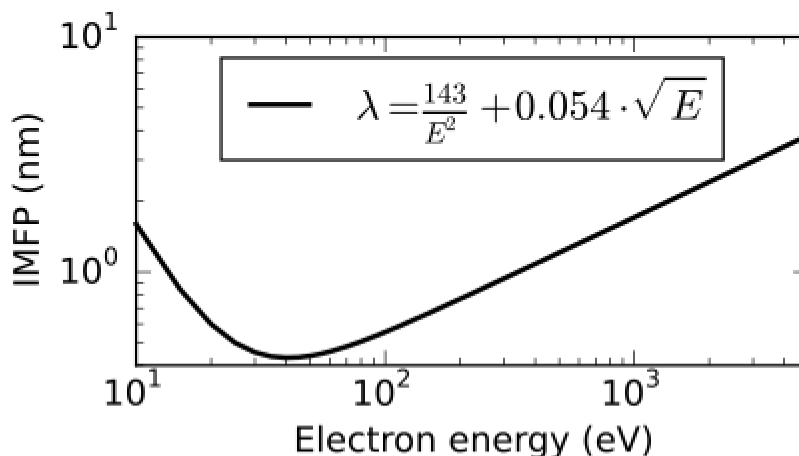

Figure V-6 Plot of electron mean free path as a function of energy commonly referred to as the universal curve. Typical electrons of interest in XPS have energies ranging from ~10-1500 eV corresponding to mean free paths of ~1nm. By G (Own work) [CC BY-SA 4.0 (http://creativecommons.org/licenses/by-sa/4.0) or GFDL (http://www.gnu.org/copyleft/fdl.html)], via Wikimedia Commons. [64]

The binding energy of electrons is element specific, this allows for straightforward identification of elements present on the sample surface by matching the observed peaks to the known characteristic patterns of elements. If other factors such as transition probabilities and photoelectric cross sections are taken into account it is possible to predict the intensities of observed peaks allowing for compositional information to be extracted from the measurement. The National Institute for Standards & Technology (NIST) has compiled a database of XPS patterns for various materials published in literature that is helpful for identifying specific patterns.[65]

Finally, XPS is able to yield information about the local bonding environment of the detected elements. Peak positions will shift on the order of several eV depending on the local bonding of the atoms. This allows for example the identification between bulk

Si atoms, SiO and SiO_2 each of which are differentiated by shifts of the binding energy by a few eV, and when in coexistence this is observed as a peak with a distinct shoulder. An example of this is shown in Figure V-7, which shows the Si_{2p} core level of a hydrogen terminated silicon surface formed by an ex-situ HF etch, which is well described by a single Gaussian, and the same sample after an Ozone clean where a high binding energy shoulder corresponding to the SiO, and SiO_2 bonding configurations is readily observable.

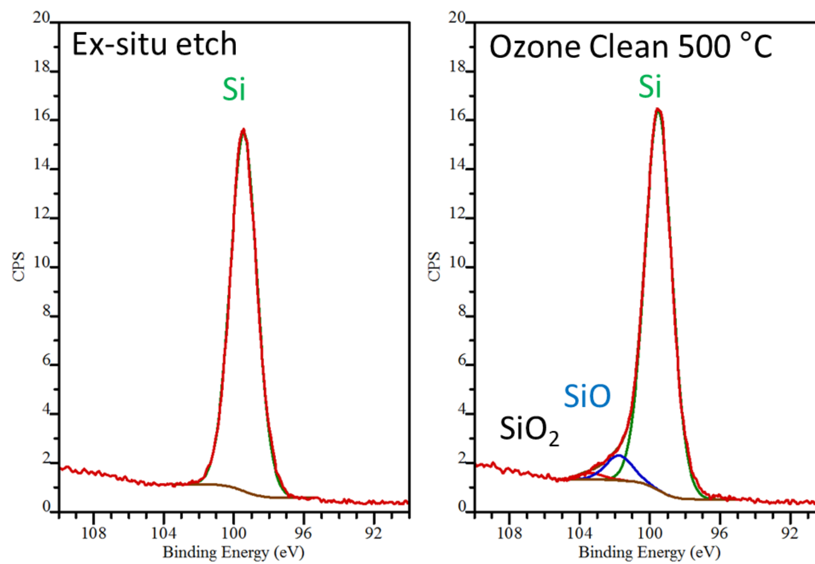

Figure V-7 Hi-Res XPS spectra of a silicon sample after a buffered hydrofluoric etch which yields a hydrogen terminated Si surface (left), and the same sample after an in-situ Ozone clean which has resulted in silicon oxides on the surface (right).

C. Scanning tunneling microscopy

Scanning tunneling spectroscopy (STM) is a powerful tool for investigating surfaces and is capable of providing both topographic information on sample surfaces with atomic resolution as well as local probes of the density of states. An STM makes use

of electron tunneling to provide extremely sensitive feedback during the measurement process. A diagram of a typical STM setup is shown in Figure V-8

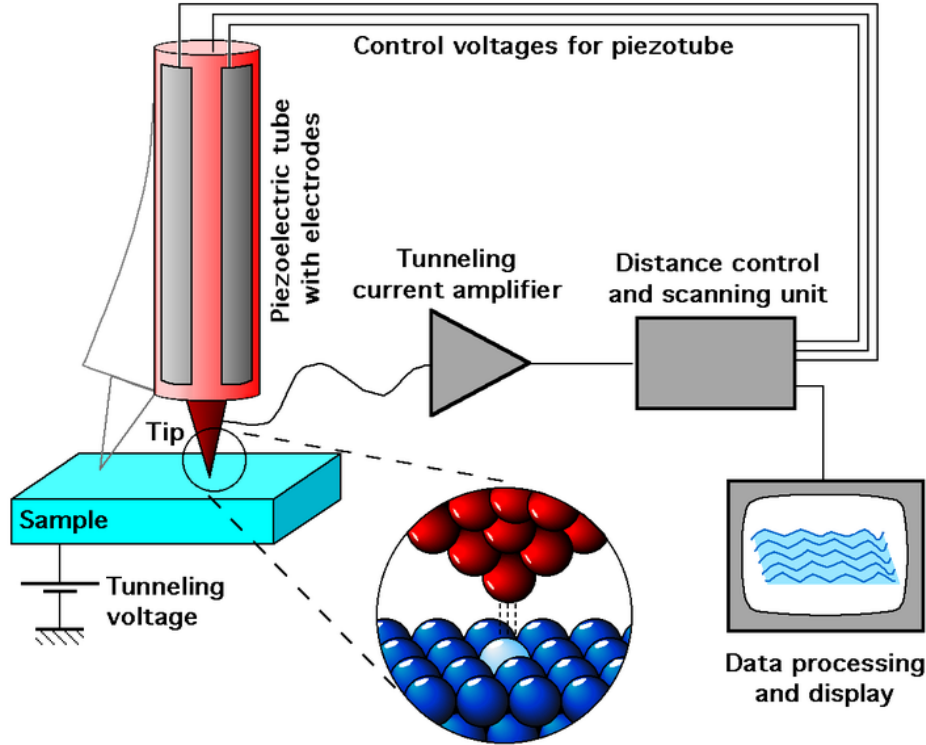

Figure V-8 Schematic of a typical STM experimental setup. A bias is applied between the tip and the sample and the tunneling current between the two is used in a feedback loop to maintain a constant tip sample separation. As the tip is moved across the sample surface the variations in height needed to maintain a constant tunneling current are recorded forming a topo graph of the surface. By Michael Schmid [CC BY-SA 2.0 at (http://creativecommons.org/licenses/by-sa/2.0/at/deed.en)], via Wikimedia Commons. [66]

The idea behind using a STM to map the surface of a sample is easily grasped with a very simple tunneling model, namely a one-dimensional system where tunneling is occurring across a vacuum barrier with a barrier height of V_0 and a width of z, z is the tip-sample separation in this model. It is possible to calculate the transmission through the barrier which results in the tunneling current of the form

$$I \propto exp(-2\kappa z) \qquad (1)$$

where $\kappa = \sqrt{2m(V_o - \epsilon)}/\hbar$. From this it is readily observed that the tunneling current is exponentially dependent on the separation between the tip and the sample. This results in a very large change in the tunneling current for small changes in tip position, and given the fine control of tip motion granted by the piezoelectric tip stage, allows for mapping of the sample surface.

However, the actual tunneling process is more complicated as both the electronic structure of the tip and surface must be accounted for. The theory of the tunneling process in STM was developed by Tersoff and Hamman[67], [68] based on tunneling theory of Bardeen.[69] To accurately model the tunneling process in STM the problem requires time dependent perturbation theory, and several assumptions such as a spherical tip shape, and slowly varying barrier height with these approximations the expression for tunneling current is

$$I(eV, R) \propto exp(-z\sqrt{\frac{8m\phi}{\hbar^2}})\rho_t(0)\int_0^{eV}\rho_s(eV, R)d\epsilon \quad (2)$$

where it can now be seen that in addition to the exponential dependence on tip sample separation z, the current also directly depends on the density of states of the sample, ρ_s, and tip, ρ_t. The convolution of topographical data and electronic structure is readily observed on surfaces such as GaAs(110) where imaging of the Ga and As atoms is interchangeable based on bias voltage, due to ionic nature of the bonding resulting in the As atoms showing up as filled states, and Ga atoms as empty states.[70]

D. Scanning tunneling spectroscopy

Often it is the electronic structure of the sample that is of primary interest in an STM measurement. If the derivative of equation 2 with respect to voltage is taken the result is

$$\frac{dI}{dV} \propto \rho_t(0)\rho_s(eV, R) \qquad (3)$$

which shows that the dI/dV of the sample is directly proportional to the local density of states of the sample which is a measurement known as scanning tunneling spectroscopy (STS)

In practice an STS measurement is performed by locking the tip in place and turning off the feedback loop the sample bias is then swept while measuring the tunneling current. While it is possible to analyze dI/dV directly from the I/V curve, by numerical differentiation, the measurement is often noisy, it is more common to use a lock in amplifier to apply a small AC bias on top of the normally applied sample bias. The lock in measures the strength of the AC signal as a function of sample bias which results in a measurement of dI/dV. Typical values for the lock-in consist of frequencies in the kHz and amplitudes on the order of 5-15 mV; a smaller amplitude is beneficial as large amplitudes will broaden features seen in the measurement so long as the signal is still detectable.

The standard dI/dV measurement is effective for metals, but for materials with energy band gaps tunneling current varies from essentially zero within the band gap with much higher values measured at biases outside of the band gap requiring a wide range of sensitivity. One method of increasing the dynamic range of the measurement is to

move the tip closer to the sample at low biases and away from the sample at high biases making use of the exponential relationship between tunneling current and sample tip separation. This is known as variable tip height STS measurement which moves the tip in a predetermined fashion during the STS measurement, typically tip height is related to voltage in a form such as $Z(V) = Z_0 + \alpha|V|$, where Z_0 is initial tip height, V is applied bias, and α a constant of the form nm/V. The tip height dependence can be removed from the result if the dI/dV is normalized by the I/V measurement yielding (dI/dV)/(I/V). For wider gaped semiconductors where I/V reaches zero before dI/dV a divergence occurs unless a Gaussian or exponential broadening has been applied, this methodology was developed and shown not to fundamentally change the resulting density of states by Feenstra.[71]

VI. Source of TLS in superconducting resonators

A. XPS analysis of sapphire (0001) surface

As discussed in chapter II, the primary goal in this chapter is to identify the possible physical sources of TLS present at the interface between the superconducting material, aluminum, and the dielectric, either sapphire or silicon. XPS is the primary method chosen to investigate this interface as it should be able to provide information on the elements present at the interface, their bonding environments, and how these change over the course of various cleaning procedures.

Sapphire(0001) substrates were subjected to a solvent clean consisting of sonication without heating in Isopropanol, methanol, and DI water before being loaded into the MBE system. Once loaded into the MBE system, an initial analysis of the substrate was done using XPS. A typical survey spectrum can be seen in Figure VI-1. Only two sources of contamination are noticeable in the survey scan, with peaks corresponding to carbon, and fluorine. The carbon peak is expected and is seen on every sample loaded into the system from atmosphere, it is indicative of hydrocarbons on the sample surface. Fluorine is much more surprising to observe since no fluorine containing compounds were used prior to loading into the system. The source of the Fluorine was eventually suspected to be from the fluoroware wafer containers commonly used to transfer wafers. The remaining peaks all correspond to the sapphire substrate. In order to observe what role the cleaning procedures had on these contaminants high-res XPS spectra was taken of each of the observed peaks as well as peaks associated with Al or O from the substrate material.

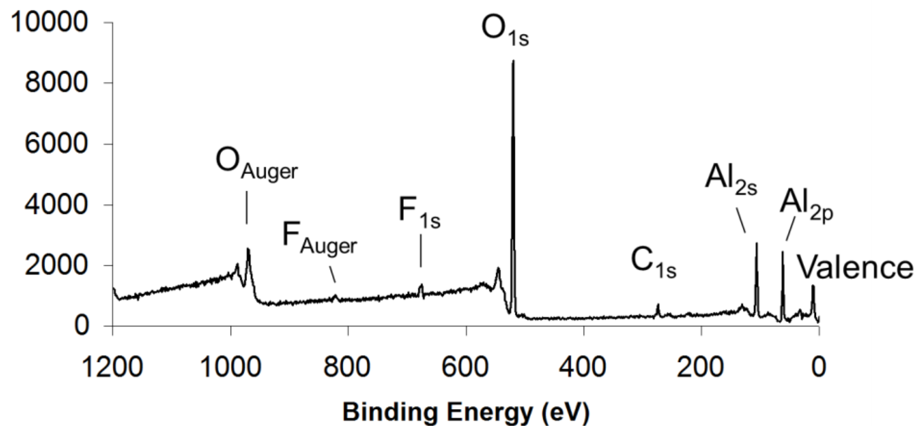

Figure VI-1 Survey XPS spectra showing all observed peaks for a sapphire (0001) surface prior to in-situ cleaning, contaminants are observed in the form of F_{1s}, and C_{1s} peaks.

Substrates were cleaned under one of three oxygen conditions for 15 minutes at temperatures increasing in increments of 150°C. Each sample was loaded into the MBE chamber and ramped to the desired temperature it was then exposed to the Oxygen/Plasma/Ozone for 15 minutes at which point oxygen flow was cut off and the sample was cooled to room temperature. Between each oxygen exposure hi-res XPS scans of the core levels were taken. Figure VI-2 plots the area of the Carbon C_{1s} and Fluorine F_{1s} peaks as a ratio of the Oxygen O_{1s} peak area. The peaks are plotted as ratios to remove systematic error that could stem from small misalignments in sample position during successive XPS scans. A clear trend is observed for the Carbon on the surface, as cleaning temperature increases more and more of the carbon is removed from the surface until complete carbon removal occurs at 750°C -900°C. Ozone may be slightly more effective, than plasma or oxygen, however, all of the oxygen cleaning methods are viable. The trend for Fluorine is not as clear, in part due to the low signal of this peak, but Fluorine coverage does seem to decrease with temperature with complete removal occurring at ~750°C. The presence of fluorine on the surface as surprising as it is not

typically a contaminant associated with exposure to atmosphere, it is believed the source is due to the flouroware transport container samples were stored in.

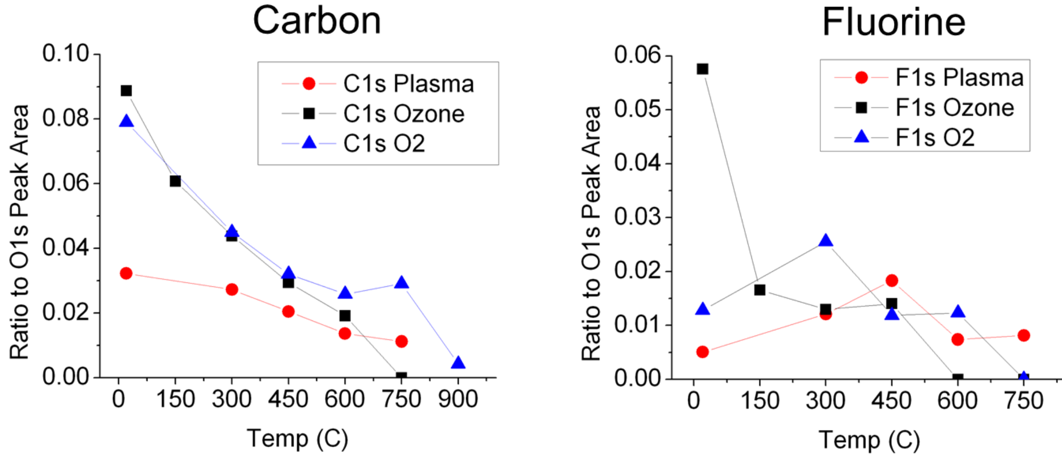

Figure VI-2 Carbon and Fluorine 1s peak area plotted as a fraction of Oxygen 1s peak area plotted as a function of annealing temperature in three different oxygen environments; oxygen plasma, ozone, and O_2.

In addition to the surface contaminants observed in the survey scan a careful study of the O_{1s} core level peak reveals the presence of a high binding energy shoulder, Figure VI-3. In literature this shoulder is related to a hydrogen surface termination of the Oxygen atoms on the sapphire surface.[72] This is particularly interesting because Hydrogen has been cited as a potential source of TLS as it shifts between two slightly different positions in the crystal.[13] The area of this shoulder was tracked by fitting a pair of Gaussian functions to the O_{1s} peak, the spacing between the Gaussians was always fixed during the fitting process. A similar decrease in peak area for the H-O bond shoulder was observed with increasing oxygen cleaning temperature shown in Figure VI-3 with complete removal of the high binding energy shoulder occurring between 600°C-750°C.

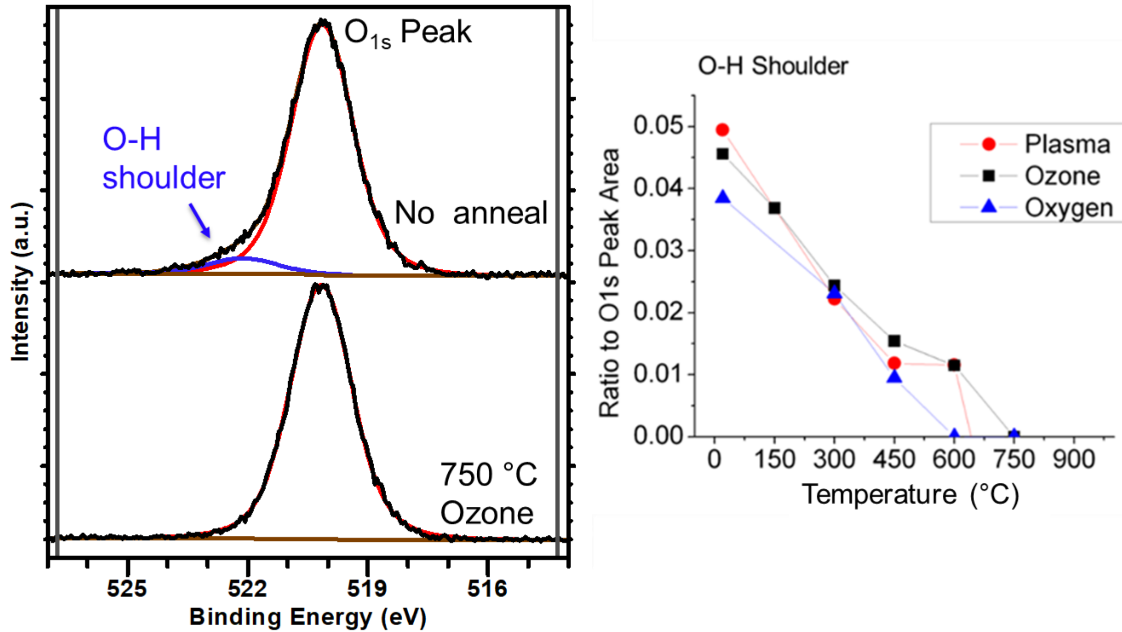

Figure VI-3 (Left) Hi-res XPS spectra showing the presence of a high binding energy shoulder on the O_{1s} core level indicative of O-H bonding. (Right) Plot of the O-H shoulder area to O_{1s} peak area as a function of cleaning temperature for several different oxygen environments.

The results indicate that the surface of the sapphire wafer is changed by the in-situ cleaning by removing carbon and fluorine from the surface, while simultaneously breaking the OH bond on the surface and removing the hydrogen. All of these contaminants are removed by similar cleaning procedures in oxidizing environments, this result is beneficial for implementing a process for qubit fabrication but leaves some confusion as to the precise source of TLS.

XPS of a sapphire(001) surface subjected to only a high temperature anneal without oxygen present is shown in Figure VI-4. It can be seen that a high temperature anneal results in the removal of the high binding energy shoulder of the O_{1s} peak that corresponds to O-H bonding, but leaves carbon still present at the interface. Given the clear observed difference in resonator performance between a high temperature clean

with and without oxygen shown in Figure II-5 this result is suggestive that carbon located at the interface plays a significant role in TLS formation.

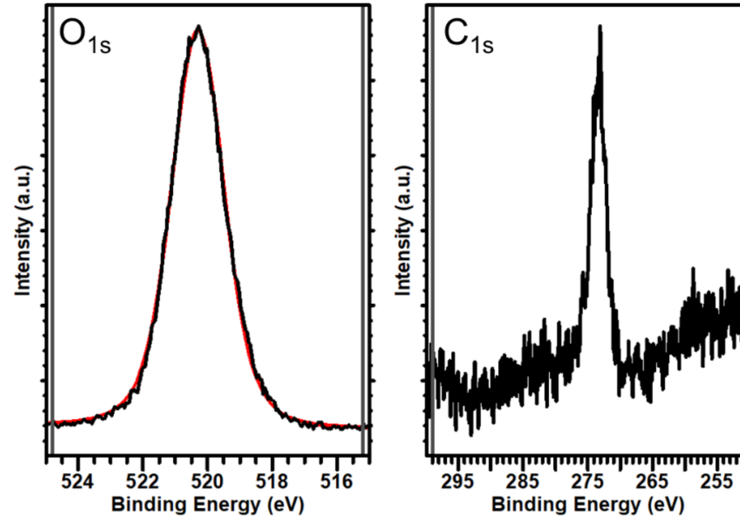

Figure VI-4 Hi-res XPS scan of a sapphire(0001) surface annealed to 750°C without the presence of Oxygen. (Left) O_{1s} peak with a Gaussian fit (red) overlapping the experimental data indicating the lack of a high binding energy shoulder, showing that O-H bands have been removed from the surface. (Right) C_{1s} core level indicating the presence of carbon on the surface.

The exact nature of the TLS is still somewhat undetermined and it may be helpful to view contaminants as falling into two categories, whether the contaminant is itself a source of TLS, or if the contaminant creates an environment conducive to TLS formation. An environment conducive to TLS formation is in reference to the disordered local crystal structure required for the energy level splitting of the double well potential. Both of these categories may in fact result in the formation of the same TLS. The presence of carbon on the growth surface typically results in contaminants between the substrate and deposited film, these contaminants may result in local disorder at the interface creating a suitable location for TLS to exist. On the other hand hydrogen is unlikely to disrupt epitaxial or textured growth but may commonly find itself sitting within the crystal lattice in vacancies or interstitials. The UHV environment of MBE is primarily limited by the

presence of hydrogen, the absolute bottom pressure achievable is typically in the 10^{-12} torr range and higher vacuum is limited by the diffusion rate of hydrogen atoms through metal seals. This implies that hydrogen is always present in some form within the MBE chamber and, if given a sufficiently disordered location may find itself present and contributing to the population of TLS. The OH on the sapphire surface if not removed by an in-situ clean may increase TLS density by supplying an additional hydrogen source which can be used to populate disordered areas.

One of the desirable properties for a surface clean would be to remove the requirement of an in-situ UHV environment and instead rely on an ex-situ process that would allow the entire fabrication process to occur in a typical clean room. Unfortunately this seem to be unfeasible. Figure VI-5, shows the C_{1s} core level of a sapphire substrate before it was loaded into the system, after an in-situ oxygen clean, and a third time after the sample was exposed to air for five minutes to simulate an ex-situ transfer that might occur in a clean room. Even after a short exposure to air a significant component of the carbon originally detected on the surface has returned. This demonstrates that to truly create a pristine interface between the superconductor and the dielectric, an in-situ clean within the growth chamber is required as any sort of air exposure results in Carbon build up on the surface.

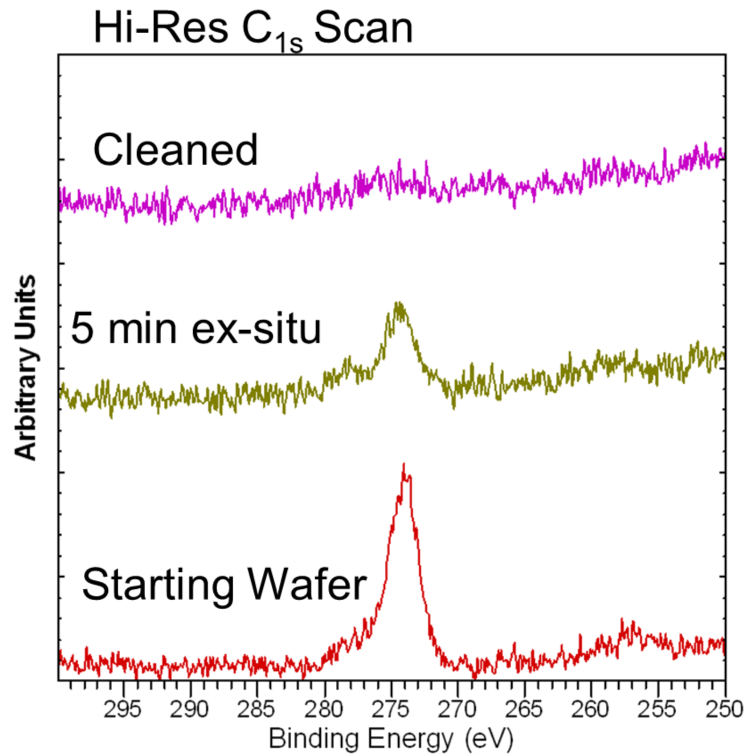

Figure VI-5 Hi-res XPS spectra of a (0001) sapphire surface as loaded into the system (red/bottom), after an in-situ ozone clean (purple/top), and after 5-min exposure to air (middle/tan).

B. Ex-situ preparation of Si (001) surface

The massive investment by the semiconductor industry into Si makes it an extremely attractive substrate material for use as a dielectric. Resonators fabricated on silicon are able to take advantage of extensive fabrication processes already developed by the industry and are easily integrated into current technology. Initial tests of resonators fabricated within the Martinis group show quality factors on Si (001) surfaces that are equivalent or better than resonators fabricated on sapphire. These results motivated a similar study of the effects of various cleaning procedures on the Si (001) surface.

Silicon is fundamentally different from sapphire due to its instability in air. Sapphire is an oxide and inert in an oxidizing environment, unlike silicon which forms a native oxide a few angstroms thick upon exposure to air at room temperature. This results in more varied ex-situ surface treatments resulting in multiple possible starting surfaces for the in-situ cleaning procedure. The silicon surfaces possible include the native oxide terminated surface, a thermally grown oxide surface, and the hydrogen terminated silicon surface. Of these the thermally grown oxide surface was quickly discounted as desorption of SiO_2 does not occur in vacuum until ~1200°C, a temperature that at the time of the study was just out of range of our substrate heater. SiO on the other hand, which is present in the native oxide, is much more volatile in vacuum and will desorb at lower temperatures ~700°C.[73] Thus focus was instead on the native oxide and hydrogen terminated surface.

The hydrogen terminated surface is what is typically used in the semiconductor industry. The surface is achieved by etching the Si wafer in a buffered hydrofluoric acid (HF), and this etch terminates dangling Si bonds on the surface with H.[74] The specific etch used in this work is a two-step process, the first etch is in nanostrip, a commercial solution that removes organic material similar to piranha, for 10 minutes. After organic removal the Si wafers were etched in buffered hydrofluoric acid (BHF) for 20-30 seconds, the Si (001) surface was confirmed to be hydrophobic after each etch by rinsing in DI water which balled up on the surface, indicating a hydrogen terminated surface. The etching process was performed in the UCSB nanofabrication facility, which required samples to be transferred from the nanofab to the MBE system. XPS Survey scans of the hydrogen terminated Si(001) surface can be seen in Figure VI-6 for a

number of transportation methods. This was investigated because, as will be discussed later, carbon on the Si surface is much more problematic to remove in-situ than is the case for the sapphire surface, and any method that limits initial carbon contamination is beneficial. The different methods of wafer transportation included, plastic containers, glass containers, submerged in DI water, and vacuum sealed in the cleanroom. For all of the transportation methods, XPS shows clear peaks for both C_{1s} and O_{1s} orbitals indicating carbon and oxygen surface contamination, a few samples show less contamination than others but all show some amount in hi-res scans. The conclusion reached by this is that no process exists that allows for ex-situ processing and loading in of a clean substrate, similar to the sapphire substrates an in-situ clean is required.

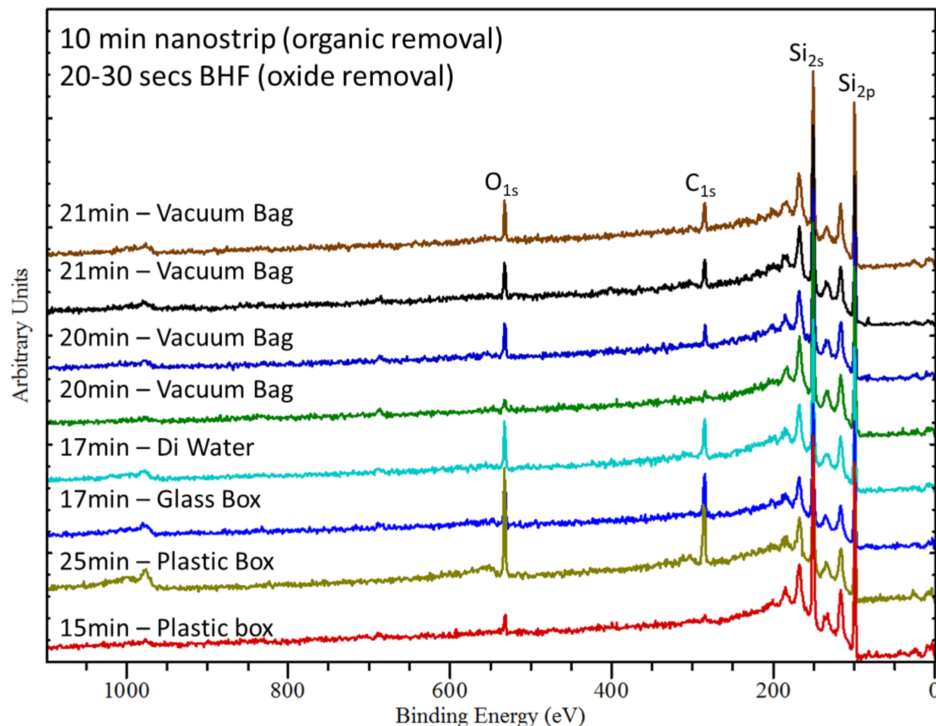

Figure VI-6 XPS survey scans of Si(001) surface after etching in nanostrip, buffered HF and transportation to the MBE system by various methods. Vacuum Bag corresponds to a vacuum sealer located in the nanofab, DI water indicates the sample was submerged in DI water during transportation, glass and plastic boxes were in atmosphere.

C. In-situ cleaning of Si(001) surface

Unfortunately in-situ cleaning of the Si(001) surface has proved much more challenging than the process used for sapphire. Several techniques were tried including in-situ annealing, in-situ ozone anneal, and in-situ atomic hydrogen anneal. The simplest method of in-situ cleaning is a thermal anneal to remove the oxide from the surface, as received epi ready Si wafers have a thin native oxide on the surface formed during the CMP process. Unlike thermally grown SiO_2, this native oxide is removable by an in-situ anneal at 850°C thermocouple temperature. XPS spectra in Figure VI-7 show that annealing Si(001) at 850°C in UHV results in a survey scan with only Si peaks, hi-res scans of the C_{1s} peak show no sign of carbon, and the O_{1s} hi res scan shows oxygen just barely above the noise threshold. These results seem very promising, but it is important to understand the limitations of XPS. As previously discussed electrons are only able to escape from the top few nanometers of the surface this means that if contaminants are condensed into small concentrated areas instead of distributed evenly across the surface a decrease in observed peak area will occur as contaminants at the bottom of the pile will have less of a contribution to the observed XPS signal, to the point that they may not be visible in XPS at all.

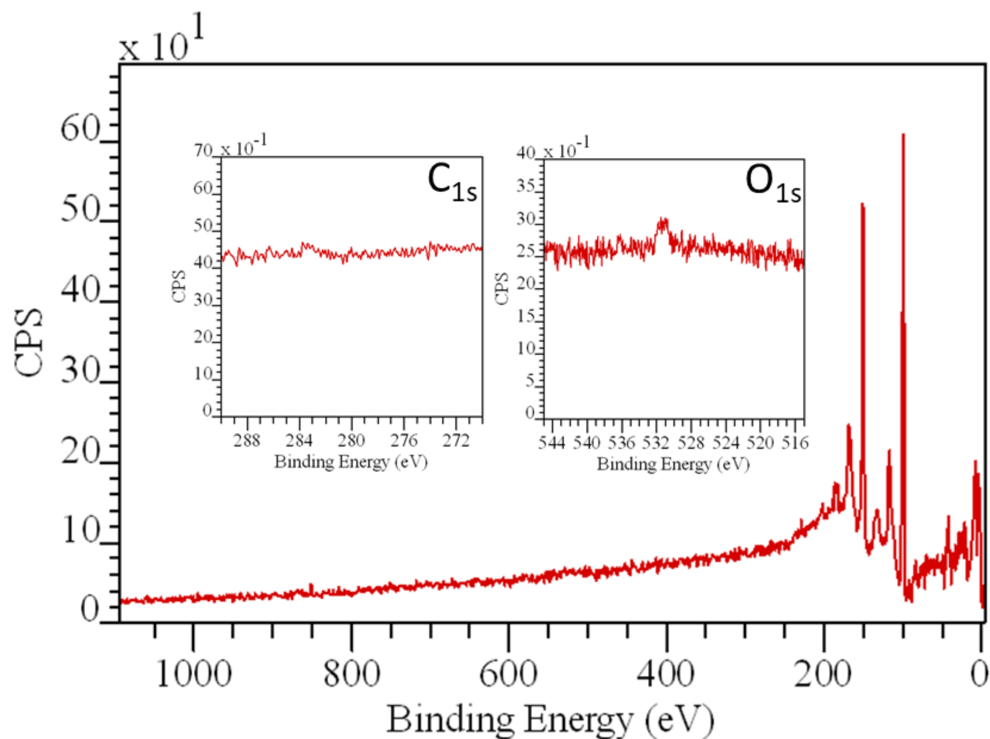

Figure VI-7 XPS Survey Scan and Hi-res scans of the C_{1s} and O_{1s} peaks for an epi-ready Si(001) surface annealed in UHV at 850°C. The lack of carbon and oxygen signal indicate low surface coverage of these contaminants.

In order to confirm the removal of carbon and oxygen from the surface, AFM of sample was performed post anneal. AFM images along with RHEED images of the [100] direction are displayed in Figure VI-8. Several different samples are shown the first sample was a hydrogen terminated surface, prepared by the nanostrip and buffered HF acid etching process previously described. This sample was annealed to 650°C, the minimum temperature needed to observe the RHEED reconstruct to the 2x1 surface reconstruction observed in Figure VI-8. The hydrogen terminated surface is initially a 1x1 reconstruction with no half order streaks observable, and the reconstruction to 2x1

coincides with removal of the hydrogen from the surface and dimer pair formation.[75] The 650°C still shows a carbon C_{1s} peak in XPS.

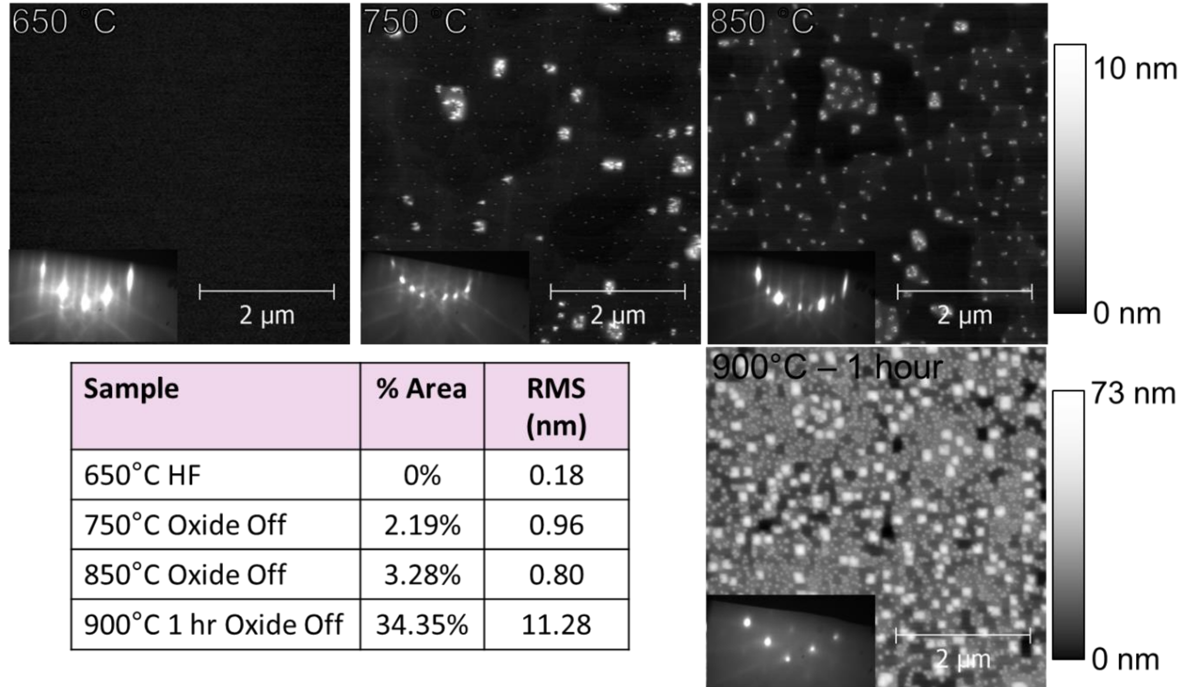

Sample	% Area	RMS (nm)
650°C HF	0%	0.18
750°C Oxide Off	2.19%	0.96
850°C Oxide Off	3.28%	0.80
900°C 1 hr Oxide Off	34.35%	11.28

Figure VI-8 AFM and RHEED images of Si(001) surfaces annealed under different conditions. The 650°C annealed surface is a hydrogen terminated surface, the three other annealing temperatures are from epi-ready surfaces with native oxide still present upon loading into the growth system. RHEED of each surface shows the 2x1 reconstruction associated with Si(001) with the exception of the 900°C surface which shows spots indicative of a rough surface. The table shows calculated surface coverage of the pyramidal structures and RMS values of the surface.

The other AFM images correspond to Si(001) surfaces loaded in with a native oxide that was removed by an in-situ anneal ranging from 750-900°C, all of these surfaces exhibited XPS spectra similar to the one seen in Figure VI-7 which does not show any signal from carbon on the surface. Rough islands are observed to form on the Si(001) surface, with surface coverage ranging from ~2% at the 750°C anneal to ~34% after the sample was annealed at 900°C for 1 hour. This increase in island coverage also corresponds to an increase in surface roughness. Both of these can be seen in the table included in Figure VI-8. Analysis of the literature suggests that island formation and

growth is a result of SiC surface contamination, despite the lack of carbon signal observed in XPS.[76] The discrepancy between the XPS and AFM results is due to the reorientation of carbon on the surface. Originally the carbon contaminants are spread across the surface uniformly. However, upon heating the carbon coalesces into 3D particles, and forms SiC particles with a much lower total surface coverage. This decrease in surface coverage along with the 3D nature of the particles is responsible for the decrease in XPS signal. The island formation is due Si desorption. At these annealing temperatures Si is slowly desorbed from the surface, however, the SiC particles prevent desorption from underneath them resulting in SiC particles forming the apex of faceted pyramidal islands. The increase in island density is not due to a difference in carbon on the surface but rather the increased rate of Si sublimating from the surface which results in larger pyramidal structures beneath the carbon particles at higher temperatures.

The experiments of thermal native oxide desorption revealed that carbon if present on the surface will react to form SiC at temperatures in excess of 700°C, therefore it is necessary to remove the carbon contaminants from the surface without high temperature annealing. Two methods were considered for this the first is a direct extension of the cleaning process found to be effective for the sapphire substrates and consisted of in-situ anneals of Si(001) surface with native oxide still intact at 500°C and 650°C in an ozone environment of ~15% O_3 ~85% O_2 at a background pressure of $5x10^{-6}$-$1x10^{-5}$ torr. The second cleaning method consisted of in-situ anneals at 500°C and 650°C in an atomic hydrogen environment of $5x10^{-6}$. The atomic hydrogen was generated in a hydrogen cracking cell which consists of a hot filament at 1900°C which splits H_2 into hydrogen radicals. This process is known to slowly etch the Si surface and

is effective at removing many semiconducting oxides.[77], [78] The goals of both processes are identical, to remove the carbon contamination before SiC formation occurs. The results of these in-situ anneals are summarized in Figure VI-9, which shows the hi-res C_{1s} spectra for each of the annealed surfaces. The ex-situ etch is a comparison to an unannealed surface that has only undergone an ex-situ nanostrip/BHF etching process this surface has hydrocarbon contaminants present, but should not have SiC formation. The C_{1s} peak position for the unannealed sample lies within the energy range typical for literature values given for carbon contaminants, in contrast the peak positions for the annealed surfaces are shifted to lower binding energies, closer to what is typically seen for SiC bonds in literature.[79]–[82] This is interpreted as the sample only having hydrocarbon contaminants on the surface, which initially do not show any features centered in the 281.3-283.3 eV range associated with SiC. As annealing temperature is increased, reactions between the hydrocarbons and the Si begins to occur, even at temperatures as low as 500°C, resulting in SiC formation and a corresponding shift in the C_{1s} peak position to lower binding energies associated with SiC. The hydrogen anneal is expected to remove the SiO at a lower temperature than that observed with a purely thermal oxide desorption, so it is not unreasonable to assume that this native oxide removal may occur at a temperature below the removal of the carbon contaminants enabling SiC formation. However, the ozone anneal should preserve the native oxide, if not increase the thickness of the native oxide layer. Given that SiC formation is also observed during the Ozone anneal process it appears that SiC formation will occur prior to carbon removal even on a Si native oxide surface. These results show that neither the

ozone, hydrogen, nor thermal anneals are sufficient to remove carbon contamination from the Si(001) surface without the formation of SiC particles occurring on the surface.

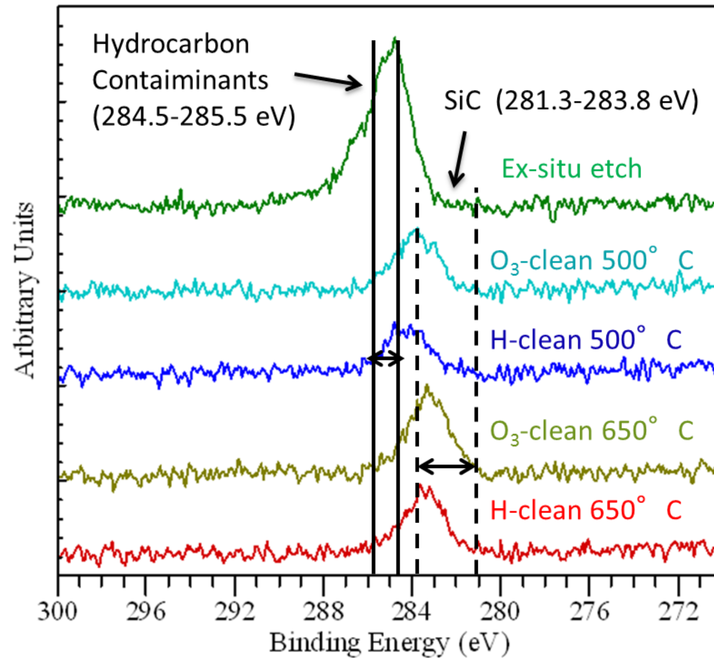

Figure VI-9 Hi-res XPS spectra of the C_{1s} core level showing the shift in peak position to lower binding energies with the application of a high temperature anneal in the presence of hydrogen or ozone. The solid lines represent the peak positions associated with hydrocarbons and the dashed lines represent the range of energies associated with SiC bonding.

D. Conclusions & future Work

The primary goal of this work was to identify the sources of TLS found in sapphire and Si based superconducting resonators. Although, still awaiting direct comparison between some of the substrate preparation methods and resonator quality factors, likely culprits in the form of hydrogen and carbon contamination at the interface were identified. The fact that resonator performance on both Sapphire(0001) and Si(001) substrates corresponds with removal of a hydrogen terminated surface (OH) termination

in the case of sapphire, and the hydrogen passivated surface as a result of an ex-situ BHF etch with Si, makes hydrogen contamination at the substrate/metal interface a likely culprit. Methods for removal of the hydrogen terminated surface have already been put forward, but hydrogen is itself problematic as it is notoriously hard to pump out from a vacuum system and a large fraction of the background pressure in a UHV system is typically hydrogen. For this reason attempts to minimize hydrogen incorporation may only be so effective. It is important to remember that for hydrogen, or in fact any defect, to form a TLS it must be located in a disordered section of the crystal structure with the possibility of accessing two potential wells of slightly different energies. It may prove that the more effective means of limiting TLS formation may be to remove the sources of disorder in the crystal structure at the metal substrate interface, which as shown in these studies is typically comprised of carbon based contamination. In fact the best results in literature for sapphire based resonators correspond to when the high temperature oxygen plasma cleaning process discussed here is employed. This process appears to have opened the pathway to TLS densities of <1 per qubit or resonator.[83]

The problem arises with the transition to Si substrates, where carbon removal prior to SiC formation has been shown to be quite difficult. Carbon on sapphire(001) substrates was found to be the limiting difference between a high temperature anneal and a high temperature anneal in an oxygen environment, suggesting that it plays a critical role in TLS formation. One method unexplored in this work is the use of Si flash anneals typically used for Si samples prepared for STM measurements. A flash anneal raises the temperature of the Si substrate to temperatures of ~1150°C at these temperatures SiC particles have increased diffusion rates and are found to diffuse into

the Si substrate leaving a smooth pristine Si(001) surface.[84] This may be beneficial as it would move regions of disorder further away from resonators resulting in weaker coupling between TLS and the electric fields present from the resonators. Unlike sapphire the process for in-situ growth of Si(001) on Si(001) by MBE is well understood, and with an elemental Si source with a sufficiently large flux a significant buffer layer could be grown in-situ.[85] Alternatively, the initial carbon contamination of the hydrogen terminated surface may be further reduced with the use of a clean glove box directly on the load lock of the MBE system allowing organic removal and final BHF etches to be performed in the glove box and samples directly loaded into the system.

As research continues towards scaling up the number of qubits present in the system it will be important to monitor the statistics of the number of TLS present in larger populations of qubits. There exist several possibilities to improve potential TLS of Si based resonators if it is required.

VII. Interfacial control of the metal to insulator transition in $RNiO_3$

As discussed in chapter III, $RNiO_3$ are an intriguing material system to study. They exhibit a number of interesting properties due to the physics brought about the correlated electron-electron interactions present within them. In this chapter the growth of $RNiO_3$ by MBE will be discussed. Thin films will be characterized in-situ using XPS, and STS illuminating the nature of a thin film MIT. Lastly control of the transport properties of $LaNiO_3$ layers will be demonstrated by altering superlattice structures.

A. Growth of $RNiO_3$ by MBE

The growth of ternary oxide materials by MBE is significantly more challenging than the growth of typical III-V semiconductors. This is for several reasons including lack of a growth window enabling self-limited growth,[86], [87] the oxidizing environment, and growth temperatures. The lack of self-limiting growth refers to both the transition metals and the oxygen present in the crystal structure. Two of the elements in the perovskite oxide structure are transition metals, both of which during MBE growth have a sticking coefficient of nearly one. This makes the growth very sensitive to variations in the elemental flux from the effusion cells. Additionally the two transition metals do not occupy interchangeable sites in the crystal structure, thus variations in composition result in defects such as additional phases, in contrast to the case of III-V ternaries where group III elements are interchangeable on the same lattice site. When dealing with oxygen many materials have multiple oxidation states available to them, so simply saturating the substrate in oxygen during growth may not result in the desired crystal

structure. Some perovskite oxides are able to overcome this and access growth windows through the use of metal-organic precursors, such as titanium tetraisopropoxide (TTIP) in growth of the titanates.[86] Similar growth processes for other oxide materials are very desirable. Some experimentation with a nickel containing precursor of Nickel acetylacetonate was done for the growth of $RNiO_3$, without success here. Instead all samples were grown using elemental k-cells which implies extreme sensitivity to fluxes as no growth window was available.

In order to achieve oxidation of the material during growth at the low chamber pressures required for MBE growth, an activated oxygen source is required. A schematic diagram of the growth system may be seen in Figure VII-1. Activated oxygen was originally in the form of oxygen radicals formed by a radio frequency (RF) plasma cell. These are typically used in both oxide and nitride MBE and fit in a standard k-cell port on the growth chamber. The downside to the plasma cell used here was a limited operation range and inconsistencies with maintaining a lit plasma under a wide range of chamber pressures. For this reason an ozone system was installed which continually generates a mixture of ~15% Ozone 85% Oxygen at a rate of 2-10 sccm. The vast majority of this flows past the vacuum chamber and is deconstructed, but a small amount is bled into the chamber through the use of a piezo leak valve. This enables control of the oxidizing environment in the MBE system from 10^{-9} to 10^{-4} torr an increase of three orders of magnitude from the plasma cell previously used.

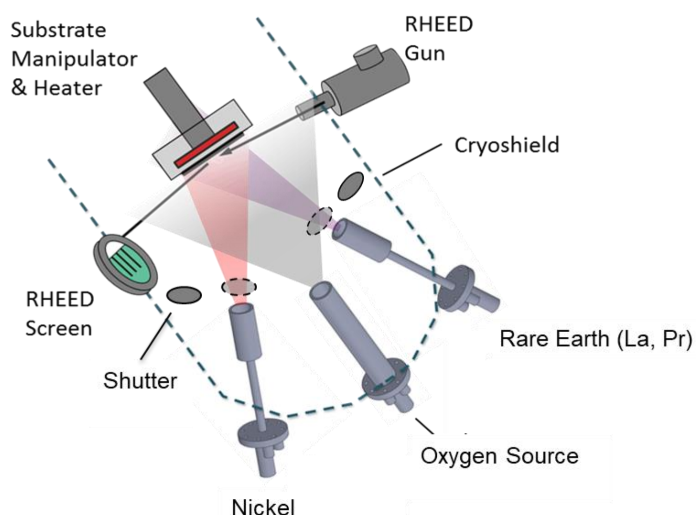

Figure VII-1 Schematic of the MBE system used to grow $RNiO_3$ materials. Shuttered growth from elemental sources was used in an activated oxygen overpressure.

The oxidizing environment in the MBE system is itself harmful to the various components of the growth system, particularly filaments or other components at elevated temperatures. This resulted in a number of changes to the hardware used in the oxide MBE chamber. Normal high temperature k-cells have significantly reduced lifespans due to oxidation at oxygen overpressures of 10^{-5} torr needed for $RNiO_3$ growth to occur. Previous work in the group showed that attempts at replacing these sources with e-guns, which can operate at higher chamber pressures, resulted in inferior crystal quality.[88] As a result high-temperature oxygen resistant k-cells were installed, as well as a high-temperature oxygen resistant substrate heater made from SiC.

Growth of all the perovskite oxides shown here was done by a shuttered growth mode. Shuttered growth entails single monolayer control of elemental fluxes. This was achieved through a combination of Rutherford backscattering spectroscopy (RBS) measurements and RHEED oscillations. RBS samples were grown for La, Al, Ni, and Pr

containing films with known deposition times, the spectra received from the RBS measurement gives quantitative analysis of the number of atoms of each element present in the film which in combination with the known growth times allows for calculation of a flux rate to within a few percent. Fine tuning of the composition was than accomplished by using RHEED oscillations and observation of the onset of a 2x2 surface reconstruction on Ni layers.

Substrates were perovskites, either $SrTiO_3$, $LaAlO_3$, or $(LaAlO_3)_{0.3}(Sr_2TaAlO_6)_{0.7}$ (LSAT), with the growth surface corresponding to (001) surface. A schematic of a $LaNiO_3$ film on a $LaAlO_3$ buffer grown on the (001) surface can be seen in Figure VII-2, the crystal structure consists of alternating layers of the A and B sites in the perovskite along with oxygen, in this case layers of LaO, and NiO. Prior to growth of the perovskite oxide an ozone/oxygen gas was bled into the chamber to a background pressure of 10^{-6} torr for growth of $LaAlO_3$ and 10^{-5} torr for growth of $RNiO_3$ as measured by an ion gauge not in direct line of sight to the oxygen source. After oxygen was present growth was achieved by opening the shutter of either the transition metal or rare earth and depositing a single monolayer on the substrate, the shutter was then closed and a monolayer of the other metal was deposited, i.e. for $LaNiO_3$ alternating monolayers of La and Ni were deposited. Substrate temperatures were 650°C thermocouple temperature for $LaAlO_3$ growth and 550°C thermocouple temperature for $RNiO_3$ growth, the true substrate temperature during growth is cooler than the thermocouple temperature by an estimate of ~50-100°C. Fluxes were typically such that individual monolayer shutter times were on the order of 20-60 seconds.

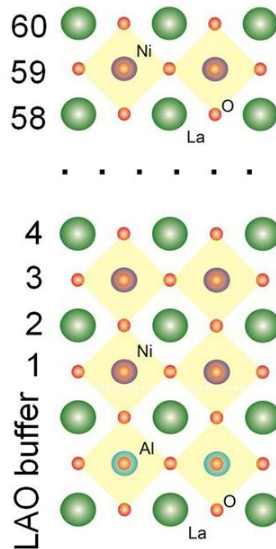

Figure VII-2 A model depicting the crystal structure of a $LaAlO_3$ substrate and buffer layer with a $LaNiO_3$ film, monolayers are numbered and each monolayer corresponds to a single shutter operation during growth.

Growth was monitored in-situ by RHEED, oscillations were frequently observed with maxima and minima corresponding to La, and Ni monolayers. Additionally, high quality growth of $RNiO_3$ material coincided with the formation of a 2x2 reconstruction in the RHEED along the [100] and [010] directions. The difference in the RHEED between a La monolayer and a Ni monolayer is shown on the left of Figure VII-3, with the red arrows showing the 2x2 reconstruction. XRD for a 30 unit cell thick film of $LaNiO_3$ on $LaAlO_3$ and $SrTiO_3$ substrates is shown on the right side of Figure VII-3. The $LaAlO_3$ substrate has an in-situ buffer layer of 30 unit cells of $LaAlO_3$ grown prior to $LaNiO_3$ deposition burying the interface, since we are unable to grow $SrTiO_3$ in our MBE system the $LaNiO_3$ film grown on $SrTiO_3$ is grown directly on the as received substrate.

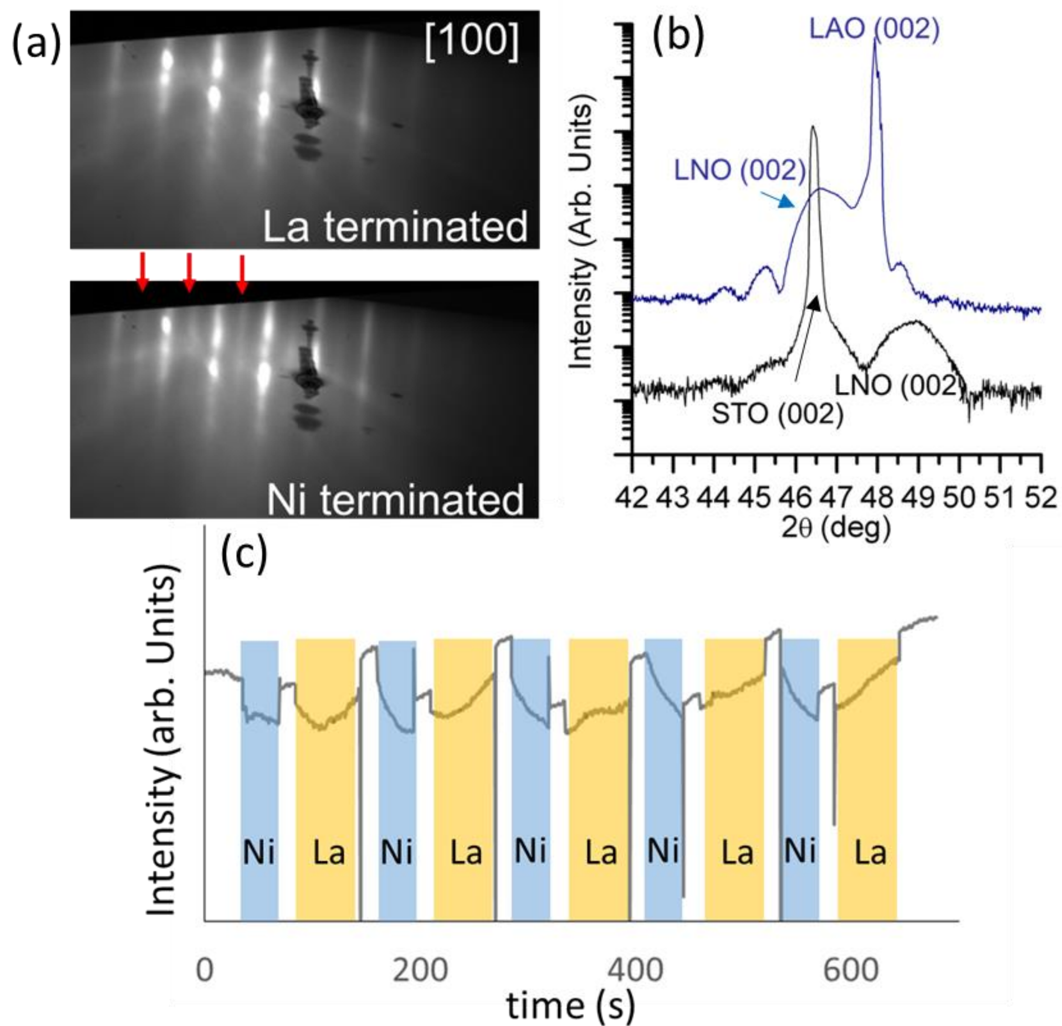

Figure VII-3 (a) RHEED images along the [100] direction showing the unreconstructed diffraction pattern of a $LaNiO_3$ film when terminated with a La layer and the 2x reconstruction associated with Ni terminated layers. (b) An XRD 2θ-ω scan showing the (002) reflection of both the $LaAlO_3$ substrate and the $LaNiO_3$ film. (c) Intensity vs time of the specular spot in a RHEED pattern for a $LaNiO_3$ film during growth, intensity is observed to increase on La monolayers and decrease on Ni monolayers

The presence of thickness fringes on either side of the primary $LaNiO_3$ peak for the $LaAlO_3$ substrate is indicative of a high quality interface and are in good agreement with our expected film thickness. The lack of thickness fringes on the $SrTiO_3$ substrate show that the best quality films are grown on $LaAlO_3$ substrates. This is in part due to the buffer layer of $LaAlO_3$, but also due to the substrate strain. Of the three substrates used,

$LaAlO_3$ is the only one which induces compressive strain in the $LaNiO_3$ and $PrNiO_3$ films, and this compressive strain is beneficial in stabilizing the correct phase. This results in streaky RHEED indicative of good crystal quality on LAO substrates. But RHEED for films on STO was faded and of poor quality for initial layers, only developing streaky RHEED after several monolayers had been deposited, see top part of Figure VII-4. Although, it is not possible to grow a $SrTiO_3$ buffer layer like $LaAlO_3$, it is possible to implement ex-situ preparation methods that result in a better initial growth surface, of atomic steps with TiO termination.[89] $SrTiO_3$ substrates were prepared by soaking in DI water for 20 minutes followed by an aqua regia etch for ~10 minutes until bubbling from the surface had ceased. After a solvent clean the substrates were then annealed in air at 1000°C for an hour resulting in a $SrTiO_3$ surface with atomic steps and a Ti surface termination. With a known surface termination, growth can begin with the Rare Earth containing monolayer resulting in a more ordered interface.

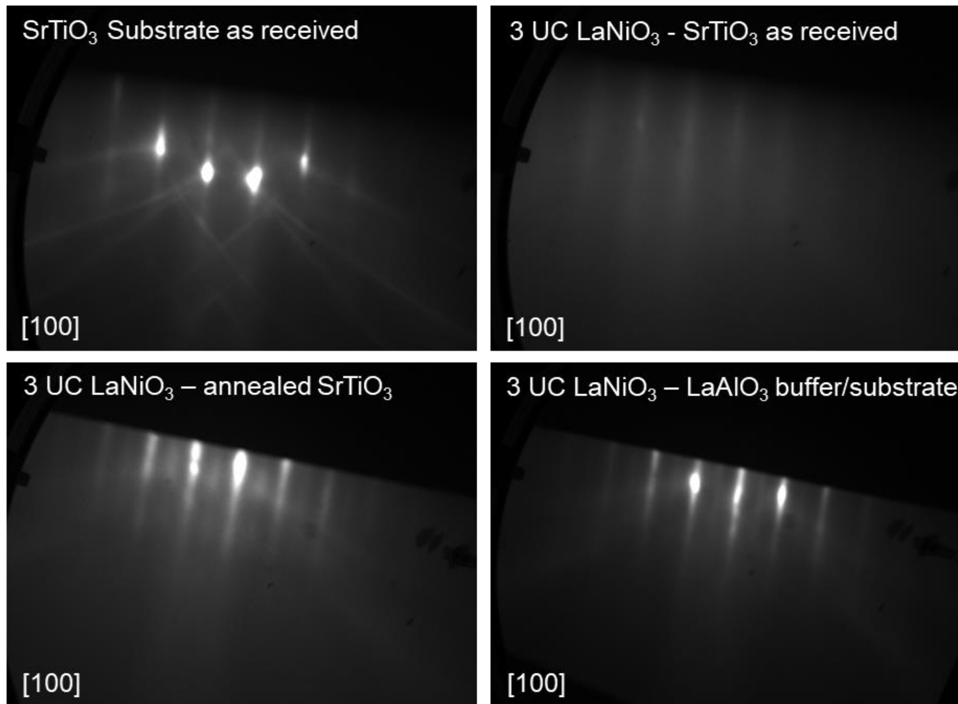

Figure VII-4 RHEED images along the [001] direction of the $SrTiO_3$ substrate and 3 unit cell thick films of $LaNiO_3$ grown on an as received $SrTiO_3$ substrate, an annealed $SrTiO_3$ substrate with a stepped surface and a $LaAlO_3$ substrate with a $LaAlO_3$ buffer layer. RHEED of $LaNiO_3$ on an annealed $SrTiO_3$ surface is significantly improved though still shows broader diffraction streaks than that of $LaAlO_3$ buffer substrates.

The results of this process are clearly observed in RHEED as shown in the bottom two images of Figure VII-4, which compares a 3 unit cell thick film of $LaNiO_3$ grown on both a $SrTiO_3$ substrate after ex-situ annealing and a $LaAlO_3$ substrate with 30 unit cell $LaAlO_3$ buffer layer. Both films have comparable RHEED with clear streaks observed and the 2x reconstruction seen on high quality films although some additional broadening appears to be present in the film grown on $SrTiO_3$, possibly indicating a slightly more disordered surface. AFM of the annealed $SrTiO_3$ substrate can be seen in Figure VII-5, along with AFM of a five unit cell thick $LaNiO_3$ film grown on an annealed $SrTiO_3$ substrate. The steps on the $LaNiO_3$ films show that the films are continuous even for small thicknesses. It was observed that some steps correspond to 2 unit cell heights due to merging of step trains on the surface.

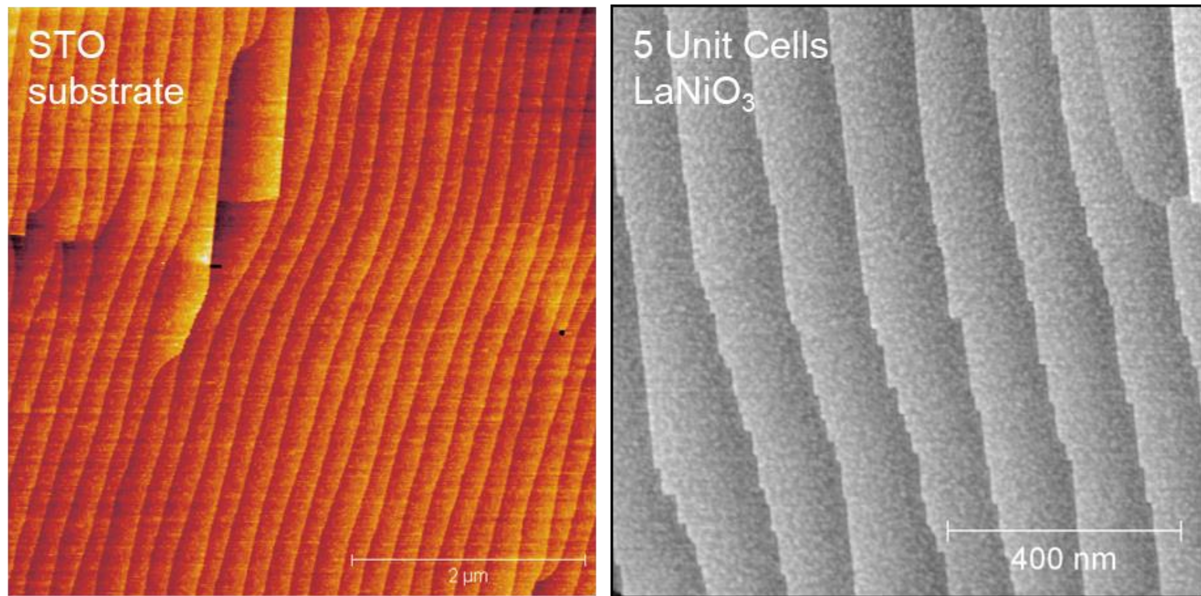

Figure VII-5 (Left) AFM of an annealed $SrTiO_3$ substrate showing the stepped surface consisting of single and double unit cell step heights. (Right) AFM of a 5 unit cell thick $LaNiO_3$ film grown on a stepped $SrTiO_3$ surface a stepped surface is still present indicating continuous film growth.

XRD for $LaNiO_3$ films grown on etched and annealed $SrTiO_3$ substrates also reveals an increase in interface quality. Figure VII-6 shows an out of plane 2θ-ω scan. The $LaNiO_3$ peak position corresponds to an out of plane lattice constant of 0.382 nm, indicating the film has not relaxed and is under tensile strain from the substrate. In comparison to the XRD shown for unannealed $SrTiO_3$ substrates shown in Figure VII-3, these films have much better interfacial quality as evidenced by the thickness fringes surrounding the $LaNiO_3$ peaks.

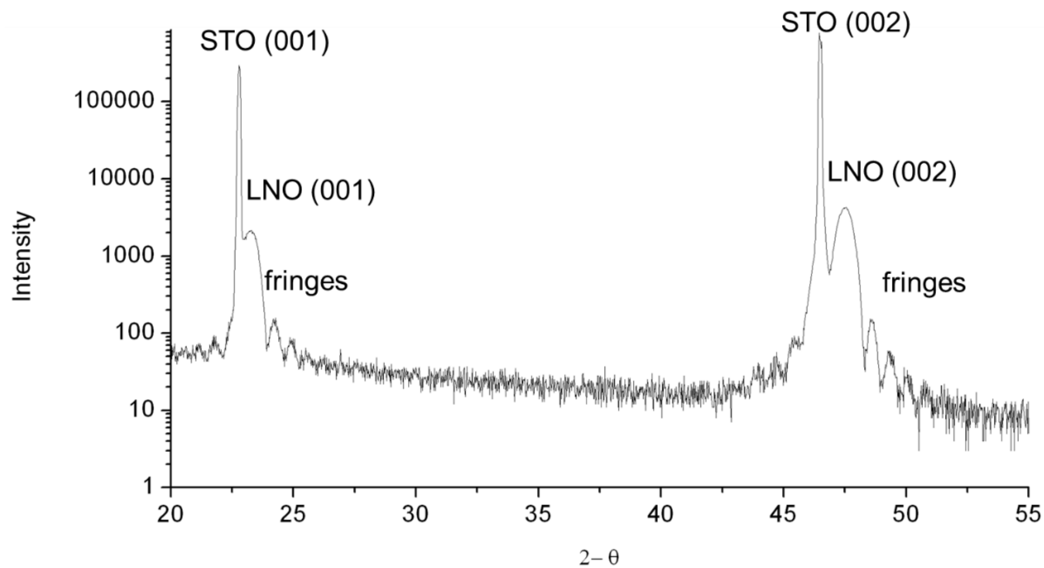

Figure VII-6 XRD of a 30 unit cell thick $LaNiO_3$ film on an annealed $SrTiO_3$ substrate. Thickness fringes surrounding the $LaNiO_3$ peaks are present indicating a sharp high quality interface. No additional phases are observed

It has been shown that high quality films of $LaNiO_3$ can be grown via MBE, however, the bulk properties of $LaNiO_3$ are metallic at all temperatures with no MIT observed. Given that the goal is to incorporate the MIT transition into devices it is necessary to grow other $RNiO_3$ which do possess a MIT. For this reason thin films were grown by the same shuttered growth mode for both $PrNiO_3$ and $GdNiO_3$. $PrNiO_3$ films were shown to grow at similar growth conditions as $LaNiO_3$, however, $GdNiO_3$ films did not result in epitaxial films at any combination of oxygen pressure, and substrate temperature. Typical RHEED for $GdNiO_3$ films can be seen in Figure VII-7 for two substrates, $LaAlO_3$ and $SrLaAlO_4$. $GdNiO_3$ has a lattice constant of 0.376 nm, this means that unlike the other $RNiO_3$ previously gown $GdNiO_3$ experiences a tensile strain of 0.8% when grown on a $LaAlO_3$ substrate. However, $GdNiO_3$ is almost exactly lattice matched to $SrLaAlO_4$, with a compressive strain of -0.13%, and growth on both substrates was explored. Ultimately, while streaks in RHEED persist to slightly greater film thicknesses

on the $SrLaAlO_4$ substrates epitaxial growth was not achieved for either substrate as evidenced by the RHEED patterns shown in Figure VII-7. Even growth of solid solutions in the form of $La_{0.76}Gd_{0.24}NiO_3$ were unsuccessful, resulting in polycrystalline RHEED patterns with additional phases.

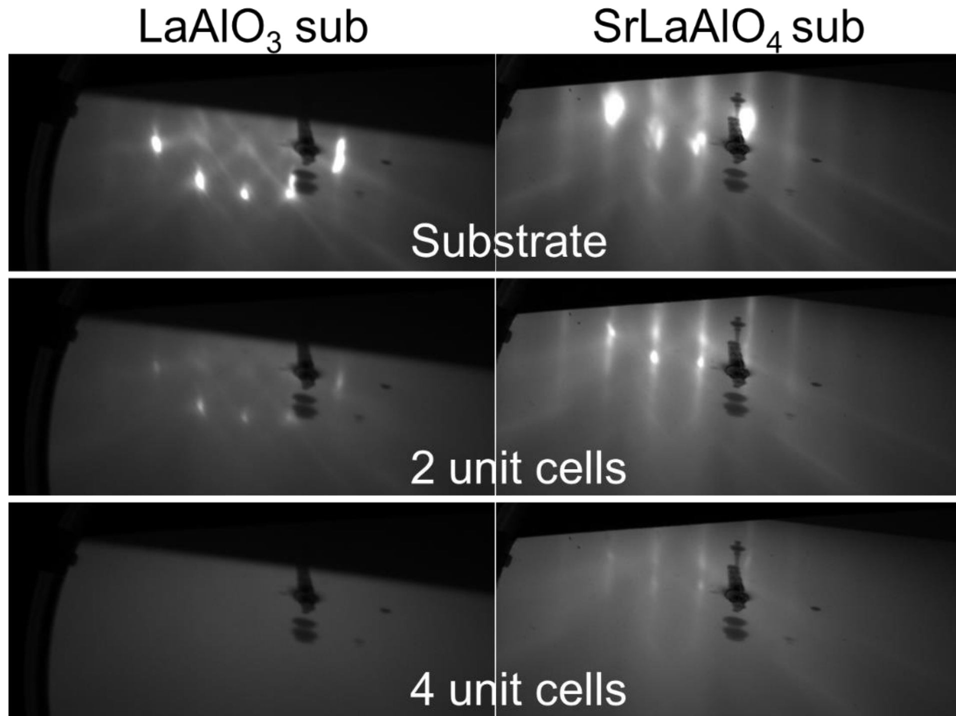

Figure VII-7 RHEED of $GdNiO_3$ film growth on a $LaAlO_3$ substrate and a $SrLaAlO_4$ substrate. RHEED pattern quickly becomes diffuse indicative of poor crystalline quality and a disordered surface.

The difficulty with growing $GdNiO_3$ thin films in comparison with the $PrNiO_3$ and $LaNiO_3$ films can be explained by examining the heat of formation for similar materials. Figure VII-8 shows heat of formation for rare earth cobaltates, manganates, and the nickelates. All of these material families show a similar trend in increasing energy of formation with heavier rare earth elements. The heat formation of $LaNiO_3$ has been overlaid on the chart, it is readily observed that the $RNiO_3$ are much less stable than the other families and only $LaNiO_3$ appears to actually have favorable formation energy. MBE

is able to grow materials outside of thermodynamic equilibrium due templating effects from epitaxial growth on a substrate, which explains why films of $PrNiO_3$ are achievable despite a positive formation energy. However, experimentally it was determined that MBFE is unable to overcome the thermodynamic barrier to $GdNiO_3$ formation at the oxygen pressures achievable in the system. This analysis of the poor film quality of $GdNiO_3$ caused our focus to shift to $PrNiO_3$ and $LaNiO_3$, with the goal of achieving a MIT in those materials.

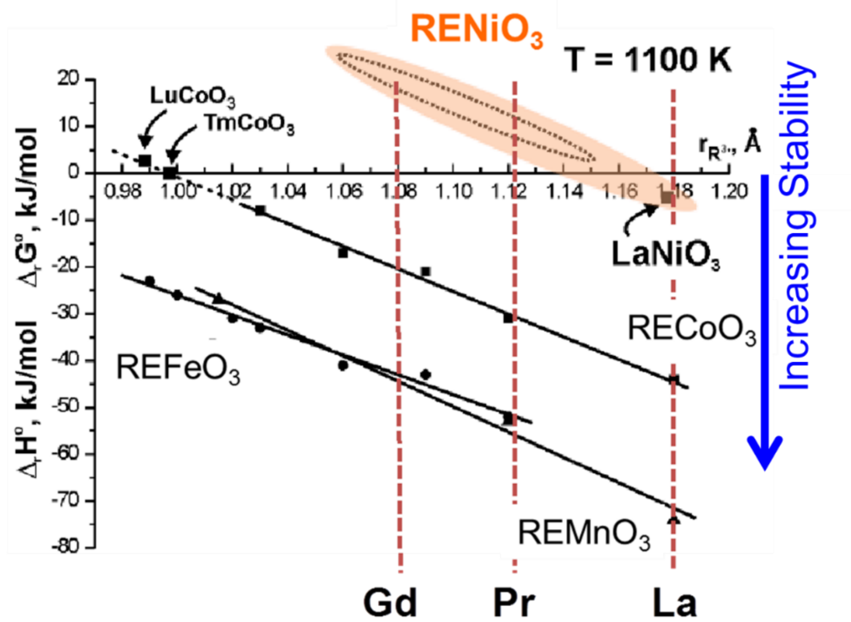

Figure VII-8 Chart of Formation energies for several rare earth transition metal oxides at temperature of 1100K. The family of $ReNiO_3$ is shown to have a positive heat of formation for all members except for $LaNiO_3$ indicating the increasing difficulty of growing thin films with heavier rare earth elements. Reprinted with permission from A. Kaul, O. Gorbenko, I. Graboy, M. Novojilov, A. Bosak, A. Kamenev, S. Antonov, I. Nikulin, A. Mikhaylov, and M. Kartavtzeva, "Epitaxial Stabilization in Thin Films of Oxides," MRS Proc.*, vol. 755, no. 6, pp. 4026–4043, 2002.. Copyright 2002 American Chemical Society.*

B. Transport properties of $RNiO_3$ thin films

Electrical properties of $RNiO_3$ thin films were characterized using a 10K hall setup. Samples were measured in a Van der Pauw geometry and contacts were made by indium dots on the corners of the samples, all contacts were ohmic indicating good contact had been made to the conducting film even for films with an insulating layer grown on the surface.

$PrNiO_3$, unlike $LaNiO_3$ will continue oxidizing once exposed to air, thus films are not stable in atmosphere. To prevent this reaction from occurring, $PrNiO_3$ films were capped with thin layers of 5-10 unit cells of $LaAlO_3$ to act as a barrier to oxidation. When the first $PrNiO_3$ films were wired up for electrical characterization they were found to be so resistive that none of our equipment was able to accurately measure I/V characteristics. Upon investigation it was discovered that $LaNiO_3$ films when capped with $LaAlO_3$ as part of growth also exhibited increased resistivity when compared to uncapped samples of similar film thickness. The hypothesis for this behavior is that when overgrown by $LaAlO_3$ the $RNiO_3$ films will give up oxygen to help oxidize the $LaAlO_3$ layer. This can be rectified by an ex-situ anneal in an oxygen atmosphere at 700°C for two hours, this brings $RNiO_3$ resistivity back to expected values. This anneal occurs at a temperature higher than the thermocouple reading of the substrate during growth and introduces concerns that anneal may induce other diffusion and phase changes beyond simply reoxidizing the $RNiO_3$ film. While exact knowledge of the microscopic process is unknown, electrical measurements show that uncapped $LaNiO_3$ films subjected to the same oxygen anneal do not show changes in resistivity compared to before the annealing process. Films of $PrNiO_3$ were characterized by XRD before and after the ex-situ anneal.

Figure VII-9 shows XRD diffraction for 30 unit cell thick layers of $PrNiO_3$ grown on a $LaAlO_3$ substrate with a buffer layer and grown directly on the substrate for LSAT and $SrTiO_3$. Measurements were performed before and after ex-situ anneal with the exception of the $SrTiO_3$ substrate which was cleaved for electrical measurements before a post anneal XRD scan was performed. The x-ray scans show the expected strain behavior for each substrate; compressive strain of -0.8% on LAO, and tensile strain of 1.3% and 2.2% for LSAT and STO. The films which had XRD scans before and after ex-situ anneal show an increase in film quality after anneal with smaller full width half max of the $PrNiO_3$ peak and more easily distinguished thickness fringes in the case of the $LaAlO_3$ substrate. No other peaks or phases were observed in the larger range of 2θ (not shown) indicating that the ex situ anneal did not change the crystal structure of the films. This result in, addition to the insensitivity of the electrical properties in uncapped films to the annealing process, implies that the annealing process is not introducing additional phases to the $RNiO_3$ film.

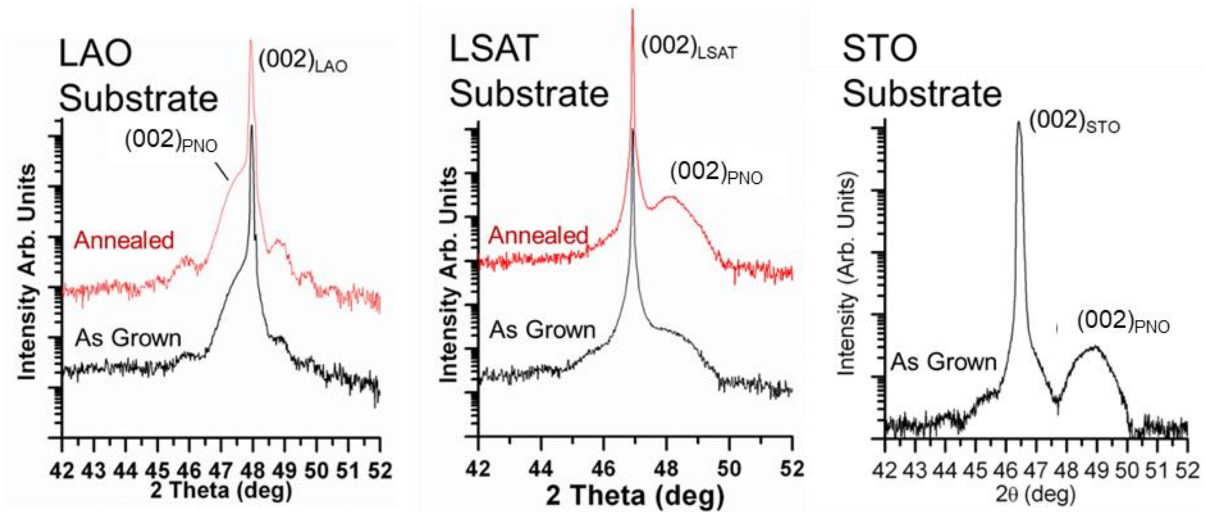

Figure VII-9 XRD of the (002) reflection for thin films of $PrNiO_3$ grown on $LaAlO_3$ (left), LSAT (middle), and $SrTiO_3$ (Right) substrates. Black curves are as grown samples without an ex-situ anneal, red curves are from samples after an ex-situ anneal at 700°C for 2 hours.

$PrNiO_3$ based on bulk measurements is expected to possess a MIT at ~140K,[27] Figure VII-10 depicts resistivity as a function of temperature for 30 unit cell thick films of $PrNiO_3$ on several substrates, none of which show a bulk like MIT. Characterization of the best quality films, as determined by XRD, grown on the compressively strained $LaAlO_3$ substrate show metallic behavior similar to $LaNiO_3$ for all temperatures. In contrast films grown under tensile strain on LSAT show a transition from metallic like behavior to insulating behavior at a temperature of ~110K. It should be noted that this MIT results in a very small change in resistivity when compared to bulk samples whose resistivity changes by several orders of magnitude.[24] Films grown on $SrTiO_3$ have the largest tensile strain and show insulating behavior at all temperatures with no metallic region. The strain dependence observed here is present in many of the $RNiO_3$ films seen in literature.[90]–[93]

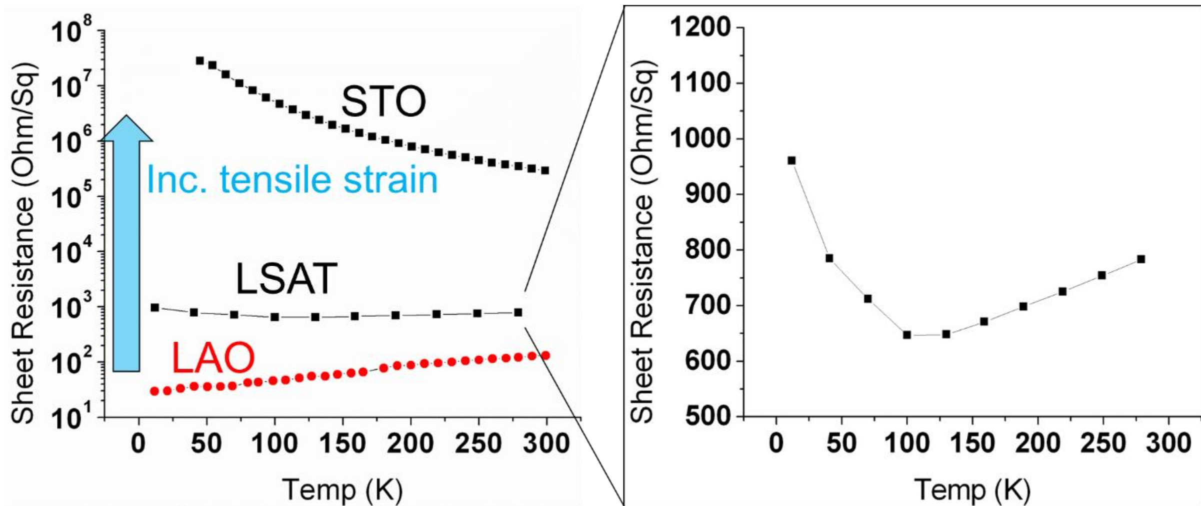

Figure VII-10 Sheet resistance plotted for 30 unit cell thick $PrNiO_3$ films grown on $LaAlO_3$, LSAT, and $SrTiO_3$ substrates. $LaAlO_3$ imparts a compressive strain, while LSAT and $SrTiO_3$ impart tensile strain. (Right) is a blow up of the resistance of $PrNiO_3$ on LSAT highlighting the minima in resistance observed at ~110K.

The bulk properties of $RNiO_3$ predict that $LaNiO_3$ should be a metal at all temperatures, and for thick films that is in fact the observed behavior. Figure VII-9 shows $LaNiO_3$ films on $LaAlO_3$ substrates (left) and $SrTiO_3$ substrates (right). $LaNiO_3$ films grown on $LaAlO_3$ show metallic behavior, decreasing resistance with decreasing temperatures indicative of a decrease in electron scattering from phonons, for films of thickness four unit cells or more. However, once $LaNiO_3$ films are a thickness of 3 unit cells or less, insulating behavior is observed, with increasing resistance with decreasing temperature. The same trend exists for $LaNiO_3$ films grown on $SrTiO_3$ substrates but the transition happens at a critical thickness between five and seven unit cells. This behavior is seen in literature as well, but the critical thickness observed on films grown by MBE is smaller than other growth methods such as sputtering or pulsed laser deposition (PLD).[94], [95] This transition seems to differ from the transition observed in 'thick' $PrNiO_3$ films of 30 unit cells due to substrate strain and implies that the much more interface dependent transition observed for thin films of $LaNiO_3$ is likely not due to strain

from the substrate. It seems likely that there is a longer range effect from substrate strain and a shorter range effect limited to a few unit cells from the interface possibly due to a shorter range octahedral tilt imparted from the substrate. This result is in agreement with TEM results in literature which examine the octahedral tilts near the interfaces in $LaNiO_3/SrTiO_3$ superlattices.[96]

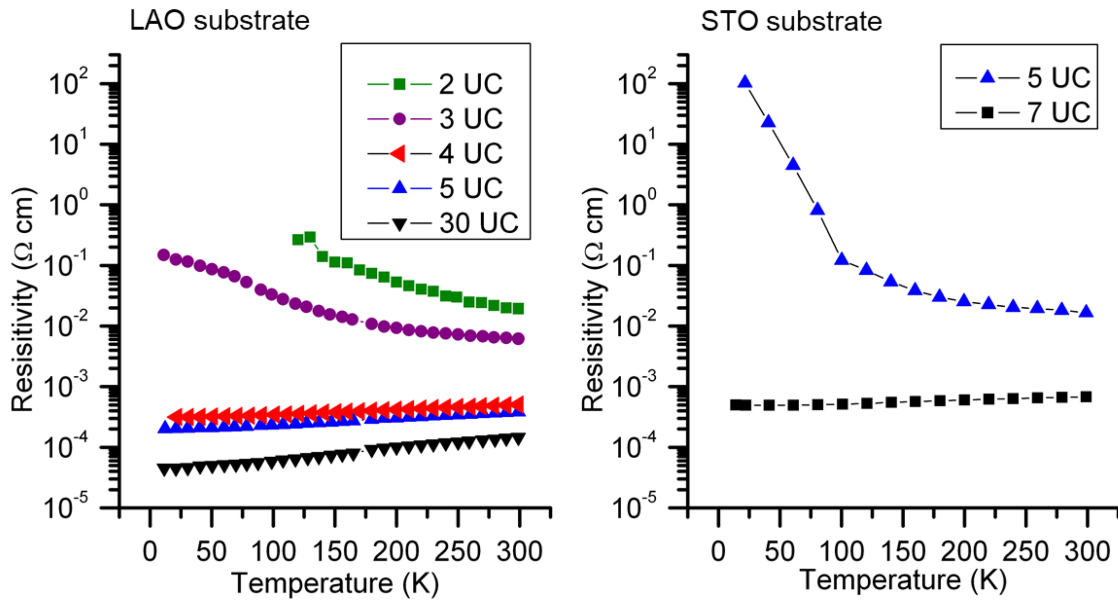

Figure VII-11 (Left) resistivity plotted as a function of temperature for $LaNiO_3$ thin films grown on $LaAlO_3$ substrates of several different thicknesses, a transition from metallic behavior to insulating behavior is observed at a critical thickness of 3 unit cells (UC). (Left) Resistivity vs temperature for $LaNiO_3$ thin films grown on $SrTiO_3$ substrates plotted for several film thicknesses the transition between metallic and insulating behavior is shifted to thicker films between 5-7 unit cells (UC).

The presence of an insulating phase for $LaNiO_3$ is intriguing as it suggests that the normally metallic $LaNiO_3$ may be induced into a MIT by the interface for thin films. The question remains what form does this MIT take, and answering this will be one of the primary goals of the experiments discussed in the next two sections.

C. XPS of $LaNiO_3$ heterostructures

One of the most important properties for semiconducting heterostructures is the band alignment of materials in the heterostructure. Band alignments affect the formation of quantum wells, tunnel barriers, insulating gate materials, and every other aspect of an electronic device and thus it is imperative that the band alignment is well understood for any pair of materials used in a heterostructure. One method of determining band alignment is to use XPS to measure the valence band and core levels in both materials on either side of the interface.[97]

XPS measurements were made using a monochromatic Al $k_{\alpha 1}$ x-ray source in a Surface Science Laboratories SSX-100 ESCA system with an emission angle of 55°. The spectrometer has a pass energy of 148 eV resulting in a system resolution of 1.7 eV as calibrated from a Au standard.

The experimental procedure consists of three separate XPS measurements of the heterostructure; two measurements of thick films and a measurement of the interface. To begin with the bottom layer of the heterostructure is grown, here $LaAlO_3$, the positon of the valence band and a distinctive core level are noted, and the energy spacing between the core level and the valence band is determined. The position of the core levels is chosen as the center of a Gaussian peak. The valence band position is measured as the intersection of the background signal and a linear regression fitted to the leading edge of the valence band. After XPS has been performed on the thick bottom layer, a small amount of the second layer in the heterostructure is deposited so that the electron escape depth (a region of a few nanometers) includes both layers of the heterostructure, from

this the spacing between the two core levels is calculated. Finally growth of the second layer is continued until it is thick enough that the entire electron escape depth lies within it and XPS is used to find the energy between the valence and core level peak. From these three values, the spacing between the valence band and the core level for each material and the offset between the two core level peaks at the interface, it is simple to calculate the resulting offset of the valence bands for the materials. This process is annotated in Figure VII-12 which shows the XPS scans for thick $LaAlO_3$, thick $LaNiO_3$, and an interface layer of 2 unit cells of $LaNiO_3$ on $LaAlO_3$. The measured valence band offset places the $LaNiO_3$ valence band 0.95 eV above the $LaAlO_3$ valence band as shown schematically on the right side of Figure VII-12. A band offset of 0.95 eV is reasonable when compared to other materials studied in literature. The $LaAlO_3/SrTiO_3$ band offset is reported as 0.2 eV, which implies a band offset of 1.15 eV between $LaNiO_3$ and $SrTiO_3$, which falls within reported values of 1.02-1.5 eV.[98], [99]

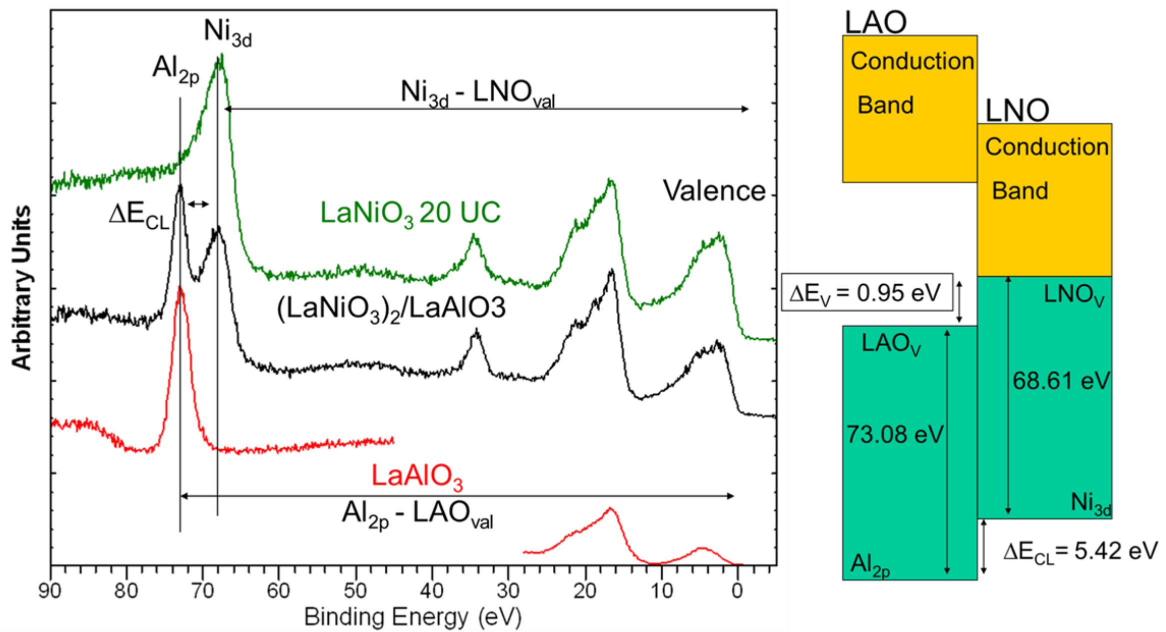

Figure VII-12 (Right) XPS spectra of a $LaAlO_3$ film, 3 unit cell $LaNiO_3$ film on $LaAlO_3$, and a thick 20 unit cell thick $LaNiO_3$ film. Lines indicate the values used to calculate the band offset. (Left) Diagram illustrating the calculated band offset, and values measured valence to core level spacing.

XPS peaks correspond to the elastic excitation of electrons from the core levels of the sample. Inelastic excitations also occur where an x-ray first drives a band to band transition or a plasmon before excitation of a core level electron out of the sample, these interactions are responsible for the increase in background intensity observed at higher binding energies after a peak in the XPS spectra is observed. This interaction means that the energy spacing between a core level and the onset of increased background intensity observed on the higher binding energy side of a peak is equivalent to the smallest energy excitation in the system. For many materials this may be a plasmon but, in dielectric materials the energy associated with plasmons is typically much greater than the energy of the band gap required to create an electron-hole pair in the conduction and valence bands.[100] An estimate of the bandgap in dielectric materials, including $LaAlO_3$, is then possible by determining the onset of background intensity after the O_{1s} peak.[101] This

analysis can be seen in Figure VII-13 and results in a measured band gap for $LaAlO_3$ of 5.87 eV. This value is in close agreement with literature which reports bandgaps of 5.5 - 6.5 eV, and is indicative that the $LaAlO_3$ layers grown by MBE display the expected insulating behavior without the need for an ex-situ anneal seen by the $RNiO_3$ materials. [102]–[104]

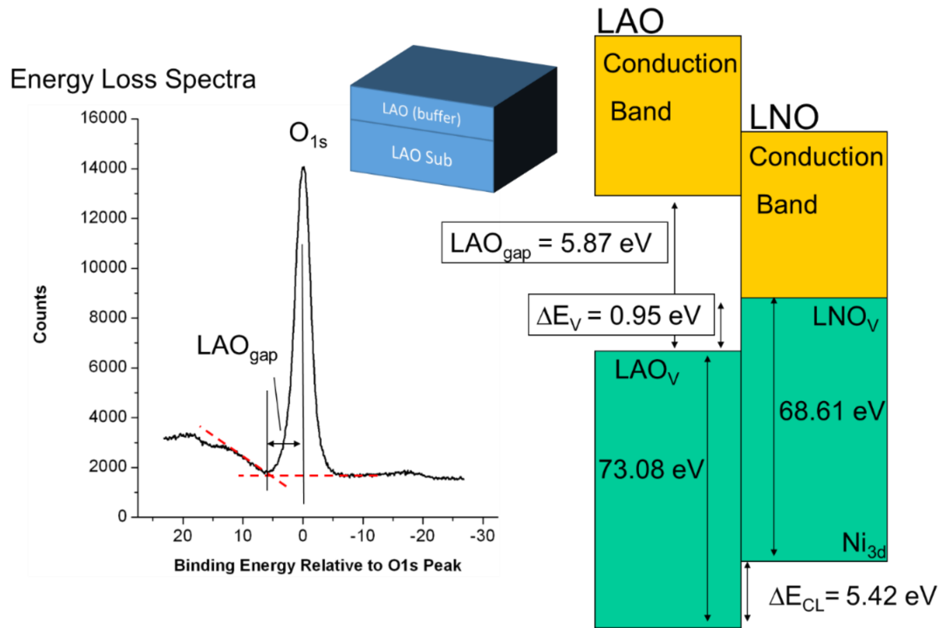

Figure VII-13 (Left) XPS used to calculate the energy loss spectra of $LaAlO_3$, intersection between peak background noise and post peak background increase is shown for the O_{1s} core level. (Right) calculated $LaAlO_3$ bandgap in comparison to previously calculated band offset.

The nature of the MIT observed in ultrathin films of the $RNiO_3$ has been a subject of interest in the literature. Many studies focusing on the electrical transport measurements comment on the relation between insulating behavior and the semi-classical Ioffe-Regel limit. This limit represents when the mean free path of an electron is shorter than the interatomic spacing, leading to Anderson localization and a transition to insulating behavior.[95], [105] Anderson localization on its own is associated with localization of electrons spatially but a continuous population in the density of states is

observed, as evidenced by optical measurements of the 3D Anderson insulator in $Li_{0.89}Fe_7Se_8$,[106] or in impurity state bands such as Mn:GaAs.[107] With this in mind, conflicting results on the nature of the thin film MIT have been published with one ARPES study claiming to observe a Fermi surface at all film thicknesses indicating Anderson localization,[108] whilst others see no Fermi surface in ARPES for the thinnest films,[109] or a suppression of spectral weight at the Fermi level in XPS, attributed to formation of a gap,[110], [111] indicative of a different form of MIT as might be expected from a Mott transition.

The $LaNiO_3$ ultrathin MIT transition was explored by in-situ XPS, with the hope of resolving a shift in the relative valence band position if a Mott transition is in fact the origin of the ultrathin film insulating state. Three unit cell thick samples were grown in an oxide MBE chamber under the standard growth conditions previously outlined for $LaNiO_3$. After growth the sample was moved to the in-situ XPS without breaking ultra-high vacuum. XPS was performed on the ultrathin $LaNiO_3$ films which were then transferred back to the oxide growth chamber where subsequent $LaNiO_3$ layers were grown followed again by XPS characterization. This process was repeated with initial $LaNiO_3$ film thicknesses below the critical thickness for insulating behavior and subsequent growths increasing film thickness until well within the range of metallic behavior. The advantages of this process is that the same sample and transport block are used for all the measurements, ideally leading to a minimization of experimental error. It is important to note that since the sample is insulating with no known calibration material on the sample surface it is impossible for the absolute position of the Fermi level to be known. Spectra were aligned by core level position and spacing between peak

positions were compared an analysis which is not dependent on knowledge of the true Fermi level. If the MIT is due to band width modulation than an insulating state should correspond to a narrowing in the O_{2p} states, which would be seen as a decrease in the distance between the valence band edge and La peaks.[24] The XPS results for the valence band and first few core levels of the $LaNiO_3$ layer on $LaAlO_3$ are shown in Figure VII-14. The purple line is a guide to eye for zero binding energy and the black lines are guides to the eye for various peak positions. The valence band composed of O_{2p} and Ni_{3d} is likely intermixed between the two and the labeling of the positions of these states may not be accurate. The $LaAlO_3$ substrate clearly has a valence band positioned below the Fermi level as expected given its large band gap. The three unit cell thick film of $LaNiO_3$ does not show any obvious gap near the Fermi level and indeed when the valence band La_{5p} energy spacing is compared to that of the four unit cell and 20 unit cell thick films, both of which are metallic, no shift is observed.

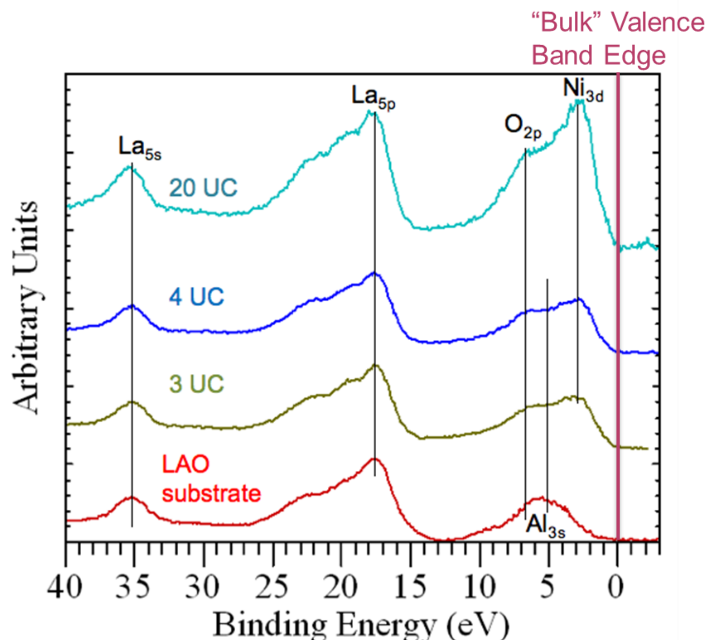

Figure VII-14 XPS of the valence band and La 5_p and 5_s orbitals for $LaAlO_3$ buffer layer, 3 unit cell thick $LaNiO_3$ which is insulating, 4 unit cell thick $LaNiO_3$ which is metallic, and 20 unit cell thick $LaNiO_3$ films grown on $LaAlO_3$. Lines are a guide to the eye, and bulk valence band edge is from the 20 unit cell thick film, and not directly measured by a gold standard. No significant suppression of spectral weight occurs at the Fermi level for thin $LaNiO_3$ films.

The experiment was repeated for $LaNiO_3$ films grown on $SrTiO_3$. This was in part due to the $LaNiO_3$ critical film thickness being larger and to have a comparison for STM samples. Figure VII-15 shows the results. The substrate is once again the only film with an obvious gap, however, it appears by eye that the Sr_{4s} and Sr_{4p} may be shifting to higher binding energy with increasing film thickness. To evaluate this the valence band edge was calculated for each film thickness by fitting a linear regression to the leading edge near the Fermi level and taking the intersection between the regression line and zero as the valence band position. Peak positions were calculated by fitting Gaussian shapes to the experimental data. The $SrTiO_3$ substrate peaks were fitted with one Gaussian for the Sr_{4s}, and two Gaussians for the Sr_{4p} and the full width half max were noted for the Sr peaks on the pure $SrTiO_3$ as well as the spacing between the pair of Sr_{4p} peaks. When

fitting the components for the other films the fitted Gaussians for the Sr components were constrained to the same full width half max and spacing used for the pure $SrTiO_3$ substrate.

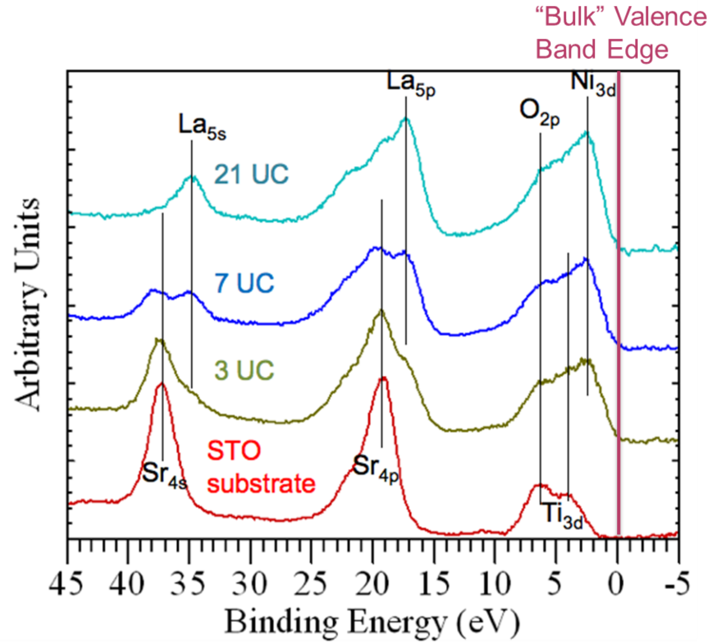

Figure VII-15 XPS of the valence band and La 5_p and 5_s orbitals for $SrTiO_3$, 5 unit cell thick $LaNiO_3$ which is insulating, 7 unit cell thick $LaNiO_3$ which is metallic, and 21 unit cell thick $LaNiO_3$ films grown on $SrTiO_3$. Lines are a guide to the eye, and bulk valence band edge is from the 21 unit cell thick film, and not directly measured by a gold standard. No significant suppression of spectral weight occurs at the Fermi level for thin $LaNiO_3$ films.

The change in energy spacing between valence band and peak positions was calculated for the Sr_{4s}, Sr_{4p}, La_{5s}, and La_{5p} peaks, the results did not show a significant change in spacing. The spacing between the Sr_{4s} peaks and the valence band edge showed an increase of 0.2 eV, but the spacing between the Sr_{4p}, La_{5s}, and La_{5p} and the valence band edge saw a decrease of -0.2 eV. This small energy spacing may be beyond the resolution limit of the lab source used for the XPS measurements, the resolution as measured from the fwhm of a Au standard is 1.7eV although peak positions are measureable to greater accuracy ~0.5 eV. In addition the assumption that the valence

band will broaden and not change position may not be correct, thus an instrument with higher resolution is needed to accurately probe the band edge.

D. STS of $LaNiO_3$ MIT

The solution for a higher resolution probe of the band edge in insulating thin films of $LaNiO_3$ lies with the in-situ low temperature STM. Using STS it is possible to analyze density of states with a resolution of ~20-40 meV, dependent on the amplitude used for the lock-in signal during the measurement. Samples for STS measurement were grown in a similar method to the ones used in the XPS study, but on Nb doped $SrTiO_3$ substrates. The first sample had an initial $LaNiO_3$ film of 3 unit cells deposited. STS was done at 4K for the constant tip height measurements, and 77K for the variable tip height measurements in the STM both using a lock in amplifier with a signal amplitude of 10 mV. After measurement the film was then returned to the growth chamber where ozone was introduced prior to heating the substrate to growth temperature. Two additional unit cells of $LaNiO_3$ were deposited and the sample was returned to the STM. This was repeated for 5, and 7 unit cell thicknesses.

The sample surface appears rough on a size scale smaller than a single monolayer ~1Å , as seen in Figure VII-16, this is due to the lack of ordered atoms observed in the STM, it is unknown why the surface appears disordered with no observable reconstruction, this is not an uncommon feature in STM of oxides, and appears even when the sample has streaky RHEED as shown in Figure VII-16. The same is true in literature where $SrTiO_3$ atomic surfaces are observed only when the sample has been significantly reduced. However, while the atomic features on the surface are disordered, the overall

roughness is very low, with height range of the image < 1.4 nm deviation, and no individual feature being larger than expected for a single unit cell, as seen by the clearly observable step height for the five unit cell thick film.

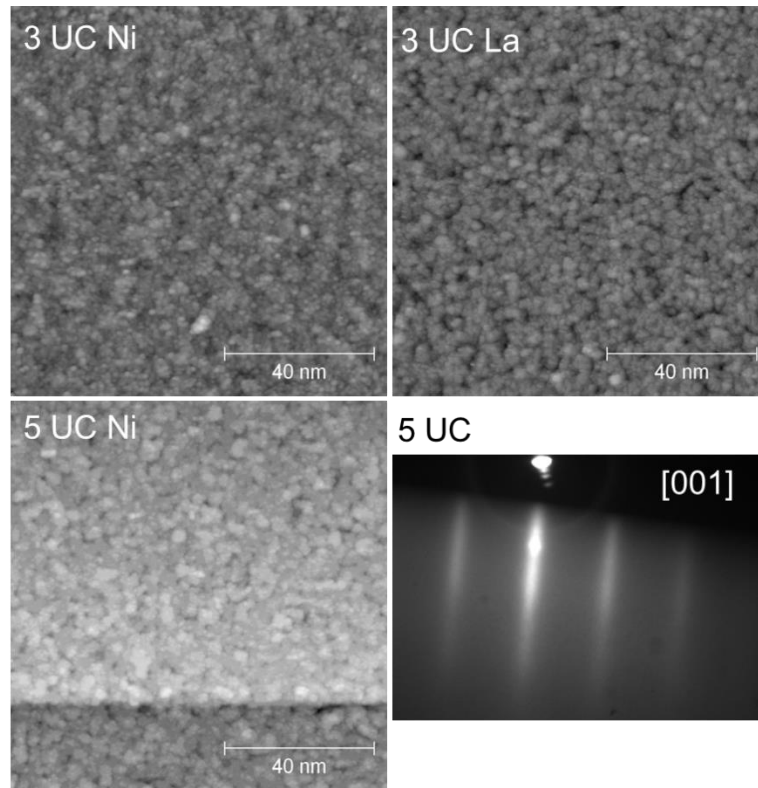

Figure VII-16 STM image taken at 77K which shows the typical $LaNiO_3$ surface at 3 unit cells for both La and Ni termination and 5 unit cell thick Ni terminated thin films. The Ni terminated 5 unit cell thick film shows a monolayer step parallel to the bottom edge of the frame that corresponds to a height 0.39 nm. RHEED (Bottom Right) shows a streaky pattern for the 5 UC thick film. STS for these surfaces is reported in Figures Figure VII-18 - Figure VII-19

STS on each of the surfaces was performed using a fixed tip positon, the results of this can be seen in Figure VII-17. The 3 unit cell thick film appears to show a large gap although it is difficult to resolve both the gap and the band edge on the +V side simultaneously, and lack of a hard gap at the bottom indicates that tip positon may have been too far from the sample to resolve the bottom edges of the band gap. The five unit cell thick film clearly shows the band edges. Linear fits have been performed and the

band gap calculated by the intersection of the linear fits with zero, resulting in a measured band gap is 1.22 eV. After the film reaches seven unit cells thick the film appears to become almost metallic with essentially a gap of zero, but a significant drop in density of states still present. The results clearly show a change in the density of states from an insulator with a gap to a more metallic state.

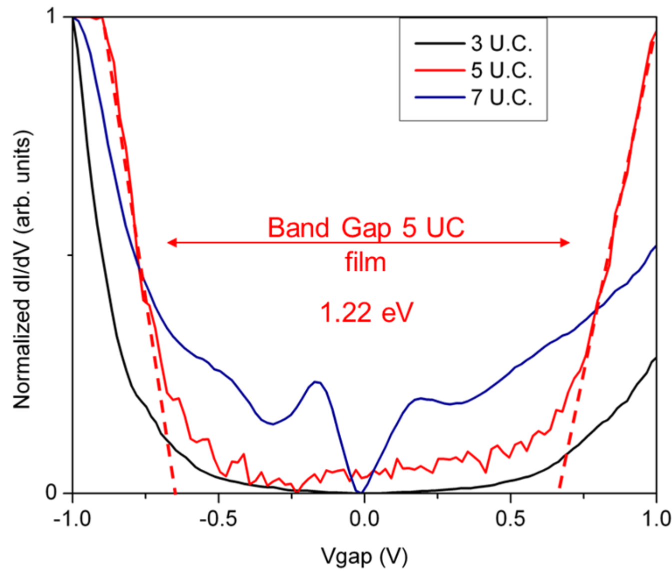

Figure VII-17 STS spectra at constant tip height taken at 4K for $LaNiO_3$ films of 3, 5, and 7 UC thicknesses. Band gap for 5 unit cell thick film is calculated by fits to the linear portion of the band edges and extrapolated to zero, process is illustrated by the dashed lines. The 7 unit cell film corresponds to the onset of conductivity for $LaNiO_3$ on $SrTiO_3$. Spectra have been normalized to conductance at -1 V.

This measured gap appears to be quite large, making it surprising that it was not able to resolved in the XPS studies, and much greater than the tens of meV gaps typically reported in literature from transport measurements of the nickelates. It was pointed out that a variable tip height method of STS is often used to increase the effective range of the lock in without saturation, and the study was repeated for insulating films of thickness 3 unit cells (Ni terminated layer), 3.5 unit cells (La terminated), and 5 unit cells (Ni terminated) with a variable tip height mode. Surface termination is assumed to be

the same as the final monolayer of material deposited during shuttered growth. STS was performed at a number of random locations on each surface, the averaged results are presented in Figure VII-18. Extrapolation of the band edges results in the largest gap, 560 meV, on the 5 unit cell thick film. The 3 unit cell thick films show a smaller band gap despite being more resistive, with a clear band gap of 300 meV for the La terminated surface and the smallest gap of 160meV for the Ni terminated surface. The 160 meV gap for the Ni terminated 3 unit cell film is not as well defined as the gaps for the other cases, this is in part due to a larger variation in gap size across the sample surface which averages out to a non-distinct band edge. The signal does not reach zero for the spectra due to background noise introduced by crosstalk, which is signal generated by capacitive coupling within the STM of the oscillating bias to the tunneling current readout. Crosstalk can be removed by locking in to the cross talk signal with the lock-in which is easily detected as the only signal present when the STM tip is pulled away from the surface, if the lock-in is then rotated 90° out of phase from the crosstalk the background is removed from the measurement. The process for minimizing crosstalk was performed for later STS measurements but was not known at the time of $LaNiO_3$ measurments. This should not have a large impact on the calculated band gaps as the intersection between true zero and the linear fit to the gap sidewalls not the background level was used in the determining the band gap. The error associated with the gap for the Ni terminated three unit cell film is greater due to the unclear area to fit the linear regression, different fits will result in different band gaps. This is due to greater variation of STS results across the surface of the sample resulting in a smeared gap edge after averaging. The increased

variability for 3UC Ni termination maybe indicative of higher disorder near the interface, as RHEED intensity was observed to increase with increasing film thickness.

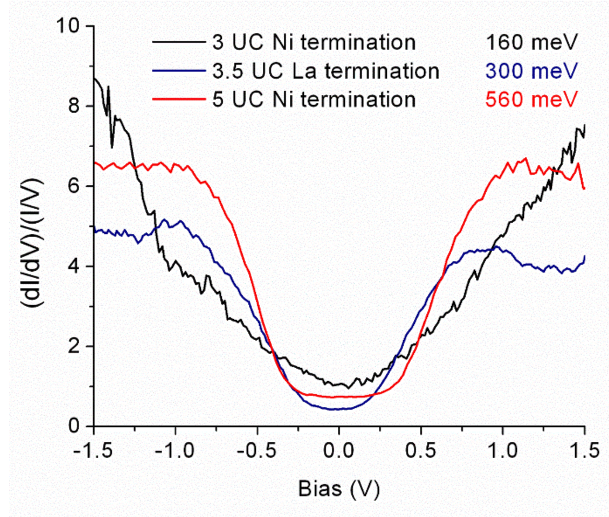

Figure VII-18 STS spectra taken with variable tip height at 77K for La and Ni terminated films of 3 unit cells on Nb:$SrTiO_3$, and a Ni terminated 5 unit cell thick film on Nb:$SrTiO_3$. Spectra are the averaged shape of several locations on each surface. Reported band gaps are calculated by fits to the linear region of the band edges.

Given that some variation in tunneling behavior is observed for different positions on the film we report the values for the smallest tunneling gaps observed in Figure VII-19. This is done as many other measurement techniques which measure a large area will most likely be dominated by signal from the areas with the smallest bandgap given the exponential relationship between tunneling and barrier height. Tip induced band bending may be present but it is difficult to characterize, or identify it's presence for $LaNiO_3$ in the thin film extreme as the true band gap is uncharacterized. While the measurement clearly shows a bandgap is present there is still some uncertainty in its magnitude. Other effects may shrink the band gap and include the resolution set by the lock-in and thermal broadening both of which are known in this case given that the lock

in amplitude was 10 meV and temperature either 4K or 77K and are small in comparison to the size of the reported gap.

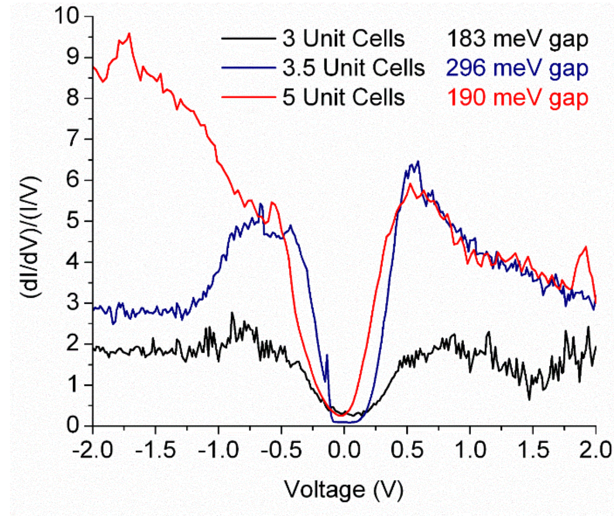

Figure VII-19 Minimum observed band gaps measured via variable tip height STS on $LaNiO_3$ films grown on Nb:$SrTiO_3$ for 3 unit cell thick films with Ni (3 unit cells) and La (3.5 unit cells) termination, and a 5 unit cell thick film with Ni termination. Band gaps are calculated by fits to the linear region of the band edges.

The smallest gaps observed for the different thicknesses were approximately 180-190 meV for the Ni terminated surfaces, and 300 meV for the La terminated surface. This energy scale is closer to the magnitude reported for the Mott MIT reported in similar materials. The gap seems to have sharper edges for the La terminated surface, this may be indicative of surface states on the Ni terminated surface not present on the La surface, though given this is not reflected in all STS measurements and may be due to variations on the sample surface. Although there is some uncertainty as to the exact width of the gap seen in ultrathin $LaNiO_3$ films all the samples do show a clear gap in the density of states, this is an important result as it clearly shows that the thin film MIT is not Anderson localization as a result of disorder but rather another form of MIT. Anderson localization is typically associated with insulating behavior without a gap in the density of states.

Theory does predict that a gap can form when disorder is present in a system with correlated electrons, as is the case in the nickelates, however, this behavior takes the form of $G(V) = G_0[1 + \left(\frac{V}{\Delta}\right)^{\frac{1}{2}}]$ where G_0 is the zero bias conductance, and Δ is a constant.[112]–[115] This model predicts a sharp pointed minima at zero bias with a $V^{1/2}$ dependence. The gaps seen here have a discernible width, and do not show the voltage dependence necessary to be a result of disorder in a correlated electron system.

E. Superlattice structures

In the previous section it was shown that the thin film MIT transition observed in $LaNiO_3$ films results in a gap in the density of states of a width on par with other Mott insulators. However, to be useful in a device the films must be grown in a heterostructure, allowing for depositon of barrier materials and contacts. Additionally, if the MIT observed for extremely thin $LaNiO_3$ is to be used in a device it may be beneficial to grow several conducting $LaNiO_3$ layers in a superlattice to enable greater conductivity while maintaining thin film properties. For this reason superlattices of alternating layers of $LaNiO_3$ and $LaAlO_3$ were grown and characterized.

Super lattice specimens were grown with the same shuttered growth method previously used. $LaAlO_3$ layers were grown at 650°C and 10^{-5} torr ozone. This is a higher oxidizing pressure than previously used for $LaAlO_3$ but allows for constant ozone pressure throughout growth of the entire superlattice structure. $LaNiO_3$ layers were grown at a substrate temperature of 550°C and 10^{-5} torr ozone, the $LaNiO_3$ layers were heated up to a temperature of 650°C when overgrown with $LaAlO_3$. The oxidizing environment in the MBE was maintained until substrate temperature was <300°C.

Similar to the capped $PrNiO_3$ samples, superlattices show extremely large resistivity values due to overgrowth of the $LaAlO_3$ layers, thus all samples were subjected to an ex-situ oxygen anneal of 700°C for two hours. XRD for two superlattice structures consisting of five unit cell thick bilayers of $LaAlO_3$ and $LaNiO_3$, repeated three and five times, is shown in Figure VII-20. Peaks corresponding to the superlattice spacing are clearly observed, as well as in the case of the five repeat structure thickness fringes corresponding to the thickness of a five unit cell thick film, further evidence that even after the ex-situ anneal sharp interfaces are maintained.

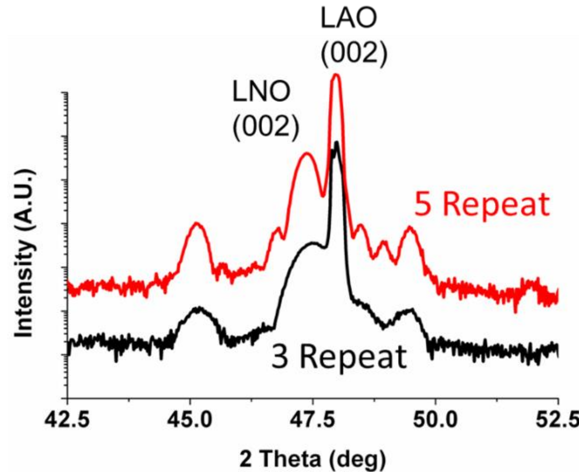

Figure VII-20 XRD scans of the (002) reflection for superlattice structures with 3 and 5 superlattice repeats. A single superlattice layer consists of 5 unit cells of $LaNiO_3$ and 5 unit cells of $LaAlO_3$. Films were grown on $LaAlO_3$ substrates. Fringes correspond to the superlattice period, with the smaller fringes of the 5 repeat sample are thickness fringes for individual layers.

Transmission electron microscopy (TEM) of the superlattice structures was performed by the company TEM Analysis, shown in Figure VII-21. It is difficult to differentiate between the layers of the superlattice, as the La present in both materials dominates the signal. The structure is epitaxial throughout, no defects are observed at the interfaces for the bottom two $LaNiO_3$ layers, although the third $LaNiO_3$ layer near the

surface appears to be looking through two domains shifted by $[\frac{1}{2}, \frac{1}{2}, \frac{1}{2}]$. This is consistent with a defect known as a Ruddlesden-Popper phase which consists of a repeat of LaO, or NiO layer.[116], [117] Typically a Ruddlesden-Popper phase repeats with a periodicity dependent on the composition. The fact that only a single area shows the half unit cell shift implies that it is not a consistent off stoichiometry during growth, but rather appears to be due to a single half-unit cell surface termination at a $LaAlO_3/LaNiO_3$ interface. Since the sample was prepared using a focused ion beam some of the intensity variation may also be a result of damage during sample preparation.

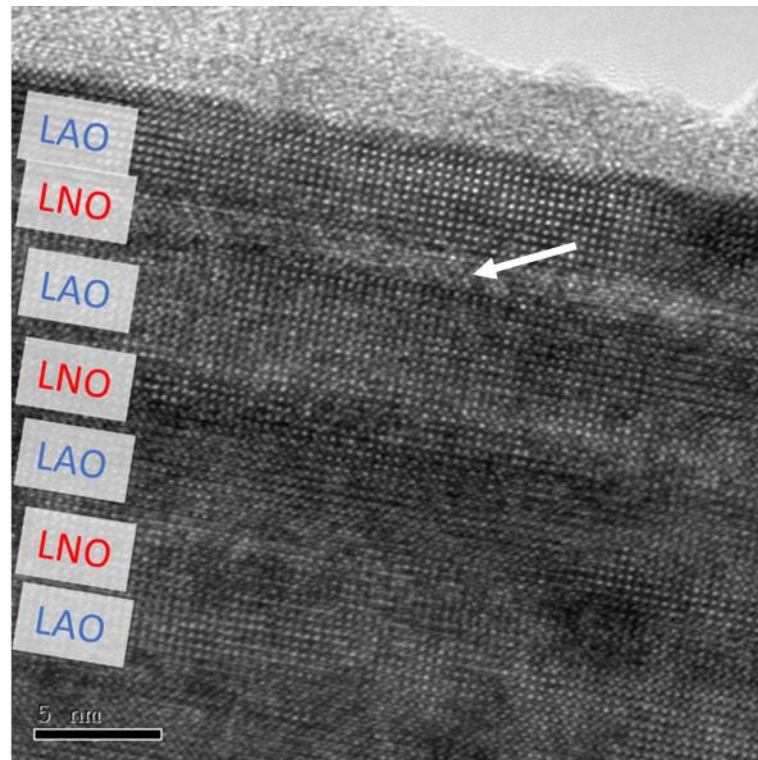

Figure VII-21 STEM of a $LaNiO_3/LaAlO_3$ superlattice structure along the [100]. $LaAlO_3$ layers are 10 unit cells thick while $LaNiO_3$ layers are 5 unit cells thick. The topmost $LaNiO_3$ layer, indicated by the arrow, of the film shows two atomic lattices offset by a unit cell vector of (½,½,½).

Electrical properties of the superlattice samples were measured with a Van der Pauw sample geometry. Contacts were made by scribing the corners of the sample and

placing soldered indium dots on the scribed corners. Resistivity vs temperatures measurements were performed in a custom built 10K Hall setup.

Resistivity for varying sizes of superlattice is plotted as a function of temperature in Figure VII-22. Similar to single layers of $LaNiO_3$, superlattice samples with five unit cell thick layers of $LaNiO_3$ are metallic at all temperatures. Resistivity in the heterostructures decreases with increasing number of superlattice layers, resulting in a decrease in resistivity at 10K of almost an order of magnitude between the superlattice of five repeats and the single layer sample. As previously mentioned, the thin film MIT appears at a thickness much smaller than the critical thickness of the film for strain relaxation, this suggests that strain is not the underlying cause. Other distortions to the crystal structure may operate at much shorter length scales, one such possibility is octahedral distortions. The thin film MIT transition could be explained by changes in octahedral angles induced in the $LaNiO_3$ by the bulk $LaAlO_3$. This model explains the decrease in resistivity with increasing superlattice layers with the premise that the thin $LaAlO_3$ layers in the superlattice do not result in the same octahedral distortions in surrounding $LaNiO_3$ layers as those caused by the thick $LaAlO_3$ substrate. The same mechanism explains single layer films, where octahedral tilts immediately at the interface result in insulating behavior, but as thicker films are grown the octahedral tilts relax to the metallic state. A very similar effect was observed in superlattices of $LaNiO_3$ and $SrTiO_3$ where the idea for this model was developed.[96]

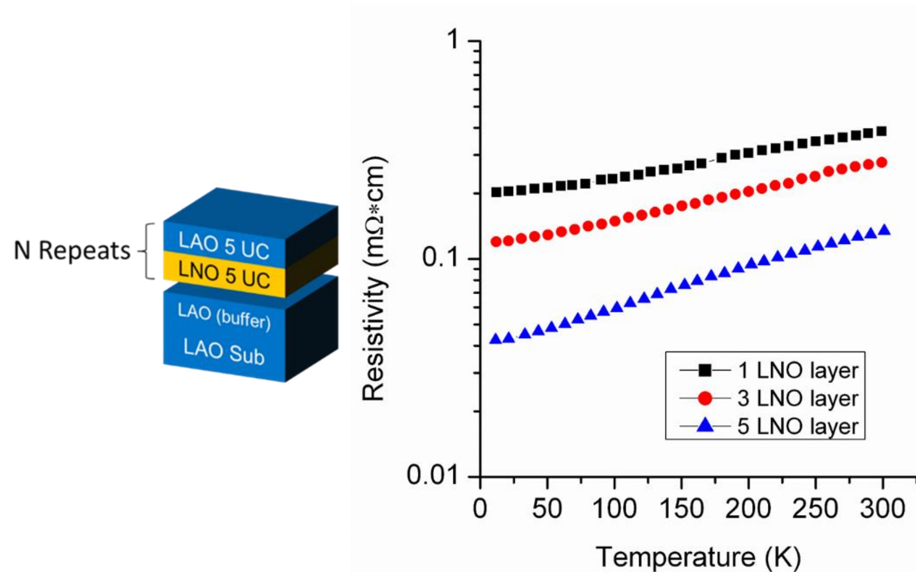

Figure VII-22 Resistivity as a function of temperature for $LaNiO_3/LaAlO_3$ superlattices with 1, 3, and 5 repeats grown on $LaAlO_3$ substrates. Superlattice layers correspond to a 5 unit cell layer of $LaNiO_3$ and a 5 unit cell layer of $LaAlO_3$.

Given that thin $LaAlO_3$ layers used in the superlattice structure do not induce insulating behavior in surrounding $LaNiO_3$ layers like the $LaAlO_3$ susbtrate there must be variation in the octahedra of the $LaAlO_3$ layers as a function of layer thickness. This idea is intriguing as it may result in a mechanism by which to tune the electrical behavior of the surrounding $LaNiO_3$ layers. As $LaAlO_3$ layers increase in thickness a transition back to bulk behavior is expected to occur at some point. Initial experiments with variation of $LaAlO_3$ layer thickness in superlattice structures appear promising. Resitivity as a function of temperature is plotted in Figure VII-23 for a superlattice with 5 and 10 unit cell thick $LaAlO_3$ layers with 5 unit cell thick $LaNiO_3$ layers. As $LaAlO_3$ layer thickness increases an in increase in resistivity of the superlattice structure is also observed. This suggests that thicker $LaAlO_3$ layers induce more insulating behavior.

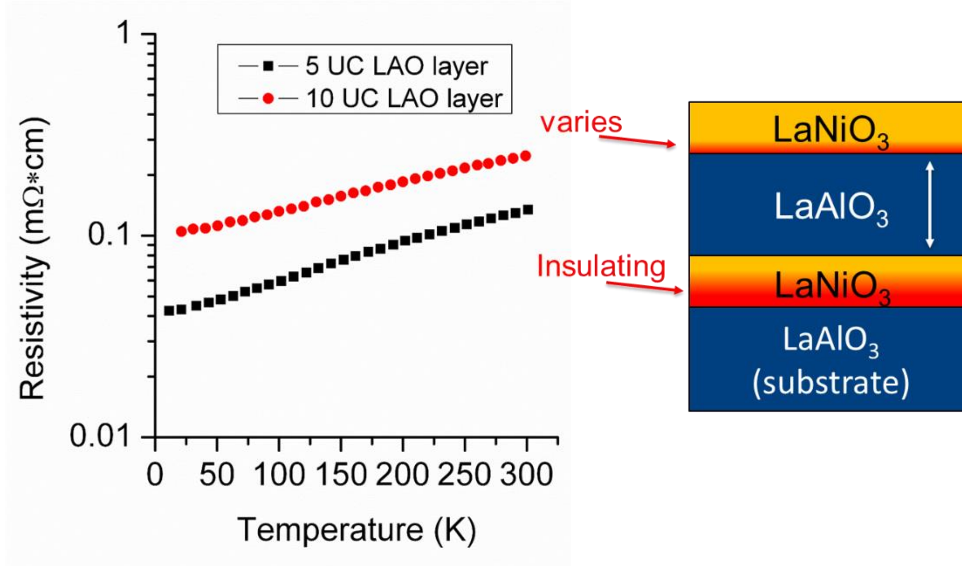

Figure VII-23 Resistivity as a function of temperature for two $LaNiO_3/LaAlO_3$ superlattices with 3 superlattice repeats grown on $LaAlO_3$ substrates. The $LaAlO_3$ layer of each superlattice is varied one superlattice has a $LaAlO_3$ layer of 5 unit cells the other 10 unit cells.

The applications for this are immediately apparent as this behavior allows for fine tuning of the electrical properties beyond what is achievable in single $LaNiO_3$ layers. An example of this is shown in Figure VII-24, which plots the resistivity vs temperature for two superlattice structures where $LaAlO_3$ layer thickness is held constant at five unit cells and $LaNiO_3$ layer thickness is varied. Figure VII-11 shows that for individual $LaNiO_3$ layers on $LaAlO_3$ substrates insulating behavior is observed for thicknesses of three unit cells or less, in contrast $LaNiO_3$ superlattices with a superlattice repeat of three and a $LaNiO_3$ layer thickness of three unit cells show a very mild MIT at a temperature of ~220K. The superlattice with two unit cell thick $LaNiO_3$ layers shows lower resistivity than expected from single layer films, closer to the resistivity reported for three unit cell thick single layer films.

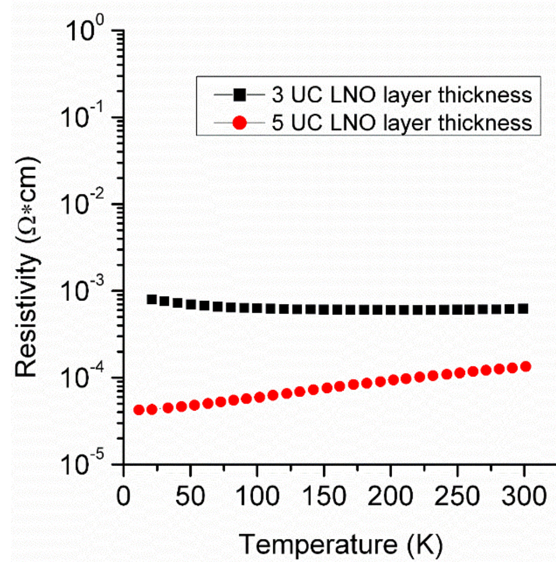

Figure VII-24 Resistivity as a function of temperature for two $LaNiO_3/LaAlO_3$ superlattices with 3 superlattice repeats grown on $LaAlO_3$ substrates. $LaNiO_3$ layer thickness was varied between 2 and 3 unit cells. 3 unit cell thick $LaNiO_3$ layers in a superlattice show a region of metallic behavior despite single layer 3 unit cell thick films of $LaNiO_3$ showing insulating behavior (see Figure VII-11).

F. Conclusion and future work

The growth of thin film $LaNiO_3$, and $PrNiO_3$ was demonstrated by MBE. Thin films of the materials were found to vary significantly in behavior from the bulk properties reported for the rare earth nickelates. Notably substrate strain plays a pronounced role in the onset of the MIT transition in this materials system with tensile strain, shifting the material towards the insulating phase and compressive strain stabilizing the metallic phase. Additionally extremely thin films exhibit a MIT regardless of rare earth used in the nickelate film or substrate material.

The nature of the MIT for extremely thin films of $LaNiO_3$ was characterized. STS measurements of the density of states show a distinct opening of a gap for thin films that is not explainable by a disorder driven transition. This evidence suggests that the thin

film MIT observed in the $RNiO_3$ is instead be due to something else, the obvious inclination is to invoke the Mott transition observed in bulk samples as the cause. However, electrostatic doping of thin films in literature only result in modest shifts in the MIT transition.[94], [118], [119] This is in contrast to what is expected for a pure Mott insulator where an influx of charge carriers should shift the band filling far enough away from half-filled state that the insulating phase collapses and metallic behavior is recovered. This behavior suggests that the MIT may instead be a result of charge ordering in the system as has been observed for small rare earth ion members of the series.[29]

Superlattices of $LaNiO_3$/$LaAlO_3$ were grown and characterized. The behavior of the superlattices indicates that individual layers of $LaNiO_3$ within the superlattice are not uniform. Electrical properties instead vary with distance from the original $LaNiO_3$/$LaAlO_3$ interface. The $LaAlO_3$ layers in the superlattice structures did not induce insulating behavior at 5 or 10 unit cell layer thicknesses, but did result in a measureable change in resistivity. This suggests that $LaNiO_3$ transport behavior may be finely tuned via superlattice structure.

These results suggest that it would be interesting in the future to explore the range of tuning allowed by superlattice growth. Superlattices also open up additional sample space for other experiments. Gating measurements on the system have so far been performed on thin films, which tend towards the thin film MIT discussed in this chapter, as screening effects and large numbers of carriers make it difficult to gate thicker films. A suitable superlattice structure would enable gating experiments to be performed

on a $RNiO_3$ with more bulk like behavior. Additionally, the attempts to induce a cuprate like response in $LaNiO_3$/$LaAlO_3$ superlattices may be heavily influenced by the nature of the octahedral tilts at the interface.

VIII. Formation of In-plane ErSb nanowires

As discussed in chapter IV, the present explanation for the self-assembly of nanoparticles in $Er_xGa_{1-x}Sb$ is unable to explain the transition to stratified in-plane nanowires observed at Er concentrations with $X \geq 0.3$. In this chapter surface morphology will be explored for a number of Er concentrations using in-situ STM. From the STM measurements a model is created that explains the driving force behind in-plane nanowire formation. Kinetic effects are also considered and shown to favor in-plane nanowire formation. Finally an alternate previously unknown low temperature nanowire growth mode is explored.

A. Experimental setup

Samples were grown in an arsenide and antimonide containing III-V VG-V80H molecular beam epitaxy (MBE) chamber with a background pressure of <5x10^{-11} torr. Substrate temperature was measured by a pyrometer, calibrated to 540°C at the GaSb(001) substrate oxide off temperature as observed by reflection high energy electron diffraction (RHEED), it should be noted that the pyrometer is sensitive to Infrared of ~2000nm wavelength most substrates are transparent at this wavelength so the pyrometer measures the indium layer underneath, however, ErSb is a semimetal and not transparent so they substrate temperature will appear to shift as ErSb is deposited.

Each sample was grown with a buffer layer of 100-250 nm of GaSb doped with Be at 5x10^{18} /cm^3 at a substrate temperature of 480°C to ensure a smooth surface before nanowire growth began. For nanowire growth, the substrate temperature was increased to 530°C so that GaSb growth was in a step flow regime.[120] Nanowires were grown by

codeposition of Er and Ga from elemental sources along with an overpressure of Sb_2. The nanostructures were initially characterized *in-situ* by scanning tunneling microscopy (STM), imaging the growth surface without any oxidation or contamination. The STM measurements were performed at 77K with a tungsten tip and a tunneling current of 30 pA, tip bias varied from -2V to 2V dependent on if the surface was primarily GaSb (negative bias) or ErSb (positive bias). Scanning tunneling spectroscopy (STS) was performed using a variable tip height method by applying an additional AC voltage on the STM tip and measuring the resulting AC signal with a lock-in amplifier. STS data was processed and normalized to approximate local density of states in the manner described by Feenstra.[71]

B. Characterization of nanowires

An embedded growth mode, was confirmed by depositing 0.15 monolayers of Er on a GaSb surface, Figure VIII-1(a). Embedded nucleation is apparent as ErSb has only

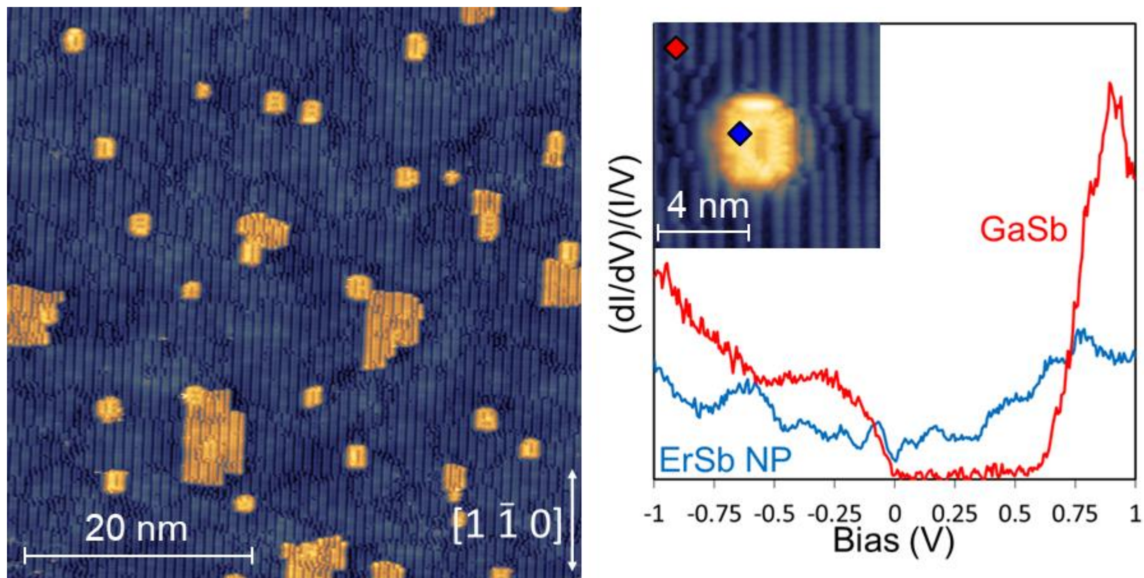

Figure VIII-1 (a) STM of 0.15 monolayers of ErSb deposited on GaSb(001) surface, -0.3V bias. (b) STS of ErSb nanoparticle, red is GaSb and shows clear gap in density of states, blue is ErSb and is a metallic density of states.

3.7% surface coverage instead of 15%, consistent with four monolayer thick nanostructures, the ErSb nanostructures appear to be one monolayer high implying three of the monolayers are embedded in the GaSb matrix, in agreement with the previously observed embedded growth mode.[53] Figure VIII-1(b) shows typical STS spectra of the sample where a metallic density of states is observed at the ErSb nanoparticles, while the GaSb matrix shows a gapped semiconducting density of states. Identification of surface reconstructions on later samples was performed by comparing STS to the ErSb and GaSb results from this known surface.

Previous work has shown that codeposited $Er_xGa_{1-x}Sb$ with Er concentrations of X=0.1 – 0.25 results in ErSb nanowires oriented out of plane, out-of-plane nanowires grow as ErSb preferentially deposits on previously nucleated ErSb particles elongating ErSb particles in the out of plane direction.[53] Figure VIII-2 displays STM topography images for $Er_xGa_{1-x}Sb$ for X=0.2, 0.25, 0.3 the surfaces for $Er_{0.2}Ga_{0.8}Sb$ closely match the expected surface for out-of-plane nanowire growth and is characterized by the ends of out-of-plane ErSb nanowires terminating on the surface at the bottom of pits in the GaSb matrix. As the Er content is increased to $Er_{0.75}Ga_{0.25}Sb$ vertical nanowires are still observed although pits are noticeably larger and deeper. At $Er_{0.3}Ga_{0.7}Sb$ the transition to in-plane nanowires has occurred and in addition to the change in nanowire orientation the pits around the nanowires have disappeared resulting ErSb nanowires lying in plane with the GaSb(001) surface.

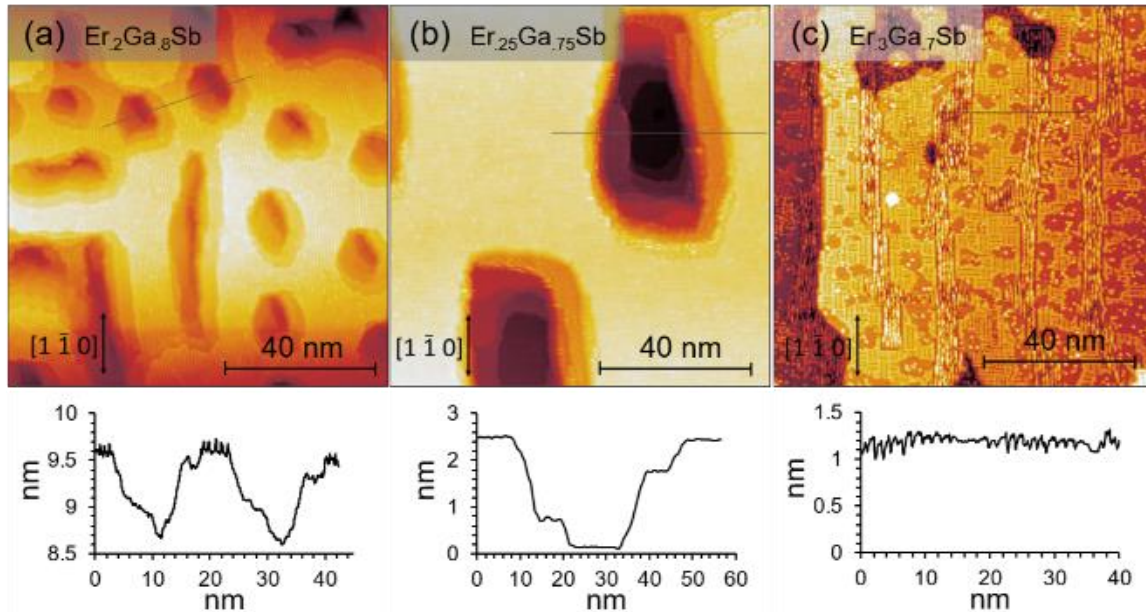

Figure VIII-2 STM and line scan of (a) Er0.2Ga0.8Sb(001) surface ErSb particles at base of pits, (b) Er0.25Ga0.75Sb(001) surface ErSb particles at base of pits and (c) Er0.3Ga¬0.7Sb(001) surface ErSb nanowires lie in plane of surface.

At X=0.3 multiple macrosteps on the order of 7 nm are observed on the surface. The scanning electron microscope (SEM) image in Figure VIII-3(a) shows the overall macrostep structure which in addition to straight step edges is also comprised of spiral features, these features are reminiscent of spiral crystal growth modes observed in a wide range of materials.[121] However, the spiral features seen here are unlike typical spiral growth as the macrostep height of 7nm is much greater than the burgers vector associated with a screw dislocation nominally associated with spiral growth.

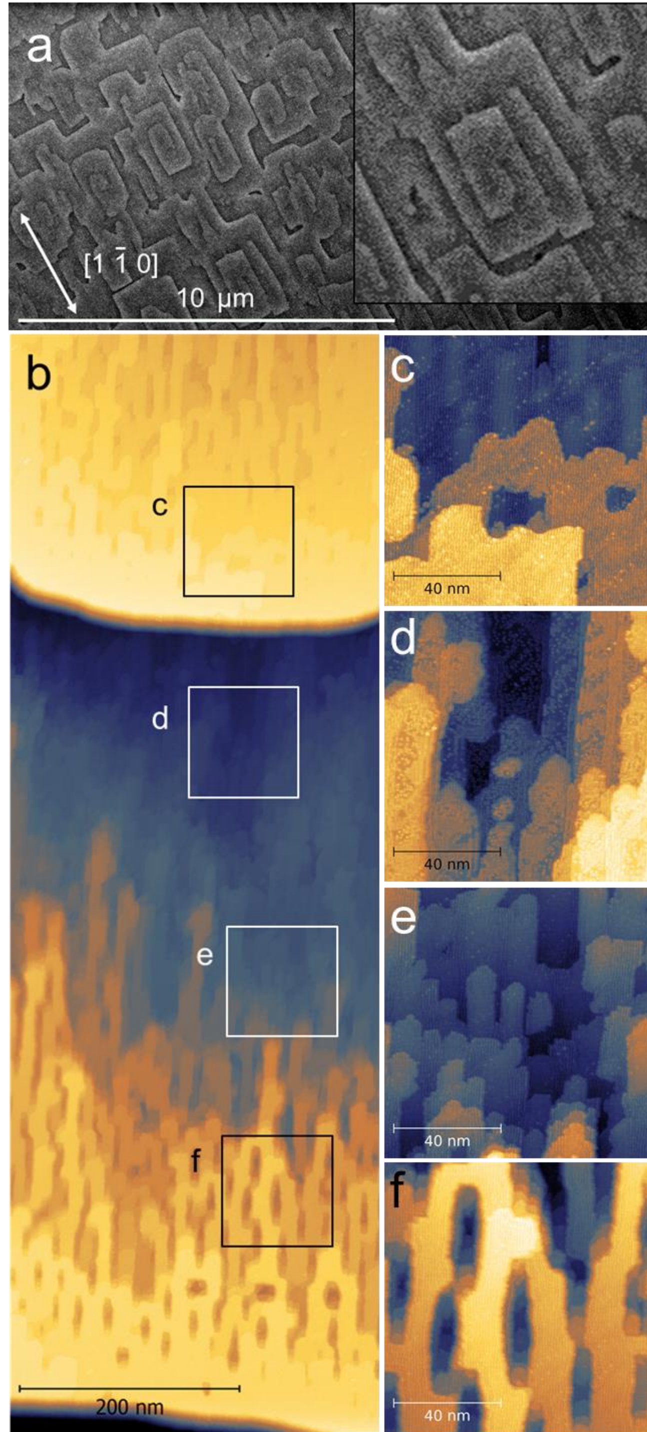

Figure VIII-3 (a) SEM of Er0.3Ga0.7Sb(001) surface, inset shows a blowup of one of the spiral macrostep features. (b) STM depicting a pair of macrosteps and the changing surface morphology across the terrace between them. Highlighted areas show positions of higher resolution images used to calculate ErSb surface coverage (c) 14% ErSb, (d) 88% ErSb, (e) 70% ErSb, (f) 5% ErSb.

Two different examples of surface reconstruction can be seen on the ErSb nanowires the first is a 1x1 reconstruction which was observed on the nanoparticles in Figure VIII-1, the second is a smooth surface interspersed with small bumps, both exhibit metallic density of states when probed by STS, these two surface reconstructions are in agreement with the reconstructions seen on 10 monolayer ErSb thin films.[54]

STM topography at several points along a macrostep is shown in Figure VIII-3(b-f) and shows a change in ErSb concentration based on position within the terrace. Areas near the bottom of a macrostep, Figure VIII-3(d), exhibit very large concentrations of ErSb (88%) while areas near the top edge of a macrostep, Figure VIII-3(c), show a much lower ErSb surface coverage of 14%. This morphology can be explained by stepflow of the macrosteps during growth. Surfaces near the top edges of macrosteps are relatively young as the macrostep has just recently overgrown the area while areas near the base of the macrostep have been exposed to Er adatoms for longer periods of time and are about to be overgrown resulting in the difference of observed ErSb coverage.

In order to confirm macrostep flow during growth cross-sectional high angle annular dark field scanning transmission electron microscopy (HAADF-STEM) was performed on an additional $Er_{0.3}Ga_{0.7}Sb$ sample grown under identical conditions to the sample shown in Figure VIII-3. The sample had ~25 nm of amorphous AlO_x deposited in situ via e-beam deposition to preserve macrostep features on the surface, the low average atomic number and amorphous nature of the AlO_x results in a large contrast with

the crystalline material beneath in the TEM . Figure VIII-4(a, c) show a macrostep looking down the [110] and [1$\bar{1}$0] direction respectively. When viewed along these directions the zincblende crystal structure appears as dumbbells whereas the rocksalt structure fills in the gaps between the dumbbells, this in addition to the high Z of ErSb nanoparticles makes them easily distinguishable as the lighter areas. Macrosteps oriented along the [110] and [1$\bar{1}$0] directions both show an uninterrupted nanowire containing layer underneath them indicating that macrosteps grow across the surface as a stationary macrostep should coincide with a discontinuity in the underlying nanowire layers.

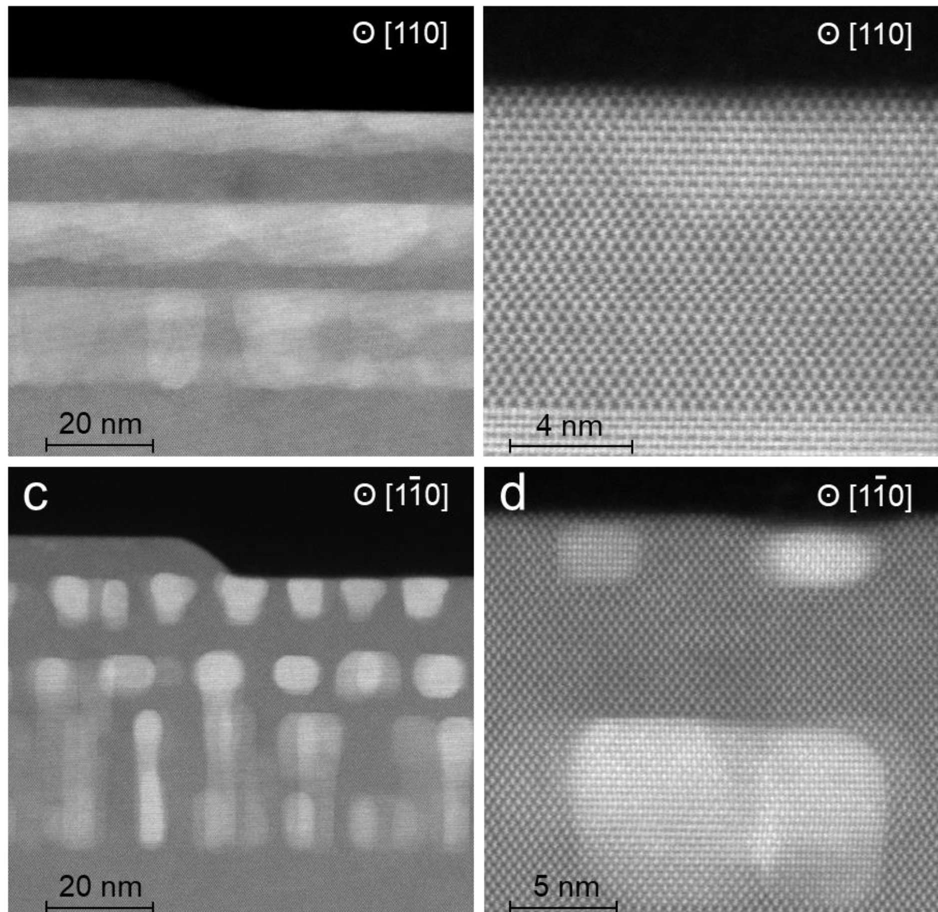

Figure VIII-4 HAADF-STEM of Er0.3Ga0.7Sb samples capped with amorphous AlOx. Lighter regions correspond to ErSb nanowires. (a) Image along the [110] direction perpendicular to the long axis of the nanowires. (b) First observable nanoparticles on the surface of the macrostep in (a) ~100nm from the

macrostep edge. (c) Image along the [11̄0] direction parallel long axis of nanowires. (d) First observable nanoparticles on the macrostep seen in (c) ~15nm from step edge. TEM done by Stephan Kraemer.

Figure VIII-4(b, d) show the first observable nanoparticle on top of the macrostep, for the [1̄10] facing macrostep (Figure VIII-4(a)) the ErSb is 100nm from the step edge, in contrast the [110] facing macrostep (Figure VIII-4(b)) shows nanoparticles within 15 nm of the step edge. This implies that macrostep growth is much faster along the [1-10] direction as would be expected from the asymmetric diffusion rates along the GaSb(001) surface[54] and in agreement with the observed asymmetry in the nanowires and macrosteps observed in Figure VIII-3.

It is not known what the spiral nature seen in some of the macrosteps shown in Figure VIII-3(a) is due to, a screw dislocation does not provide a large enough burger's vector to generate the observed macrostep height, but it is possible another form of defect is responsible perhaps an interaction involving nucleation of a twinned islands as seen in GaAs growth on planar ErAs layers.[122] To identify any dislocations or twinning in the surface electron channeling contrast imaging (ECCI) was performed. The 25nm thick AlO_x capping layer was sufficiently thick to prevent electron channeling during the measurement. Hence, a 25 nm $Er_{0.3}Ga_{0.7}Sb$ without a capping layer was grown for characterization by ECCI. ECCI is sensitive to displacements of atoms in the crystal structure such as the strain fields in dislocations. Figure VIII-5 shows an ECCI image of the surface of an $Er_{0.3}Ga_{0.7}Sb$ film, a misfit dislocation can be seen rising up to the surface at the top of the image and appears as a line vertically along the center of the image, a few other misfit dislocations were observed using ECCI but no other defects were seen. This implies that there is no defect present at a density similar to that of the macrosteps on the surface responsible for their formation. However, it should be noted that spiral

macrosteps were not observed on this sample despite the clear presence of macrosteps and horizontal nanowires, macrostep and horizontal nanowire formation is therefore independent of the spiral structures previously observed in SEM (Figure VIII-3(a)). It may be that the macrostep structure varies due to small changes in growth temperature or initial growth surface but the presence of macrosteps and horizontal nanowires appears to be independent of macrostep shape. This is in agreement with work done in the ErAs/GaAs system which found the shape of GaAs islands nucleated on ErAs was sensitive to growth temperature.[122]

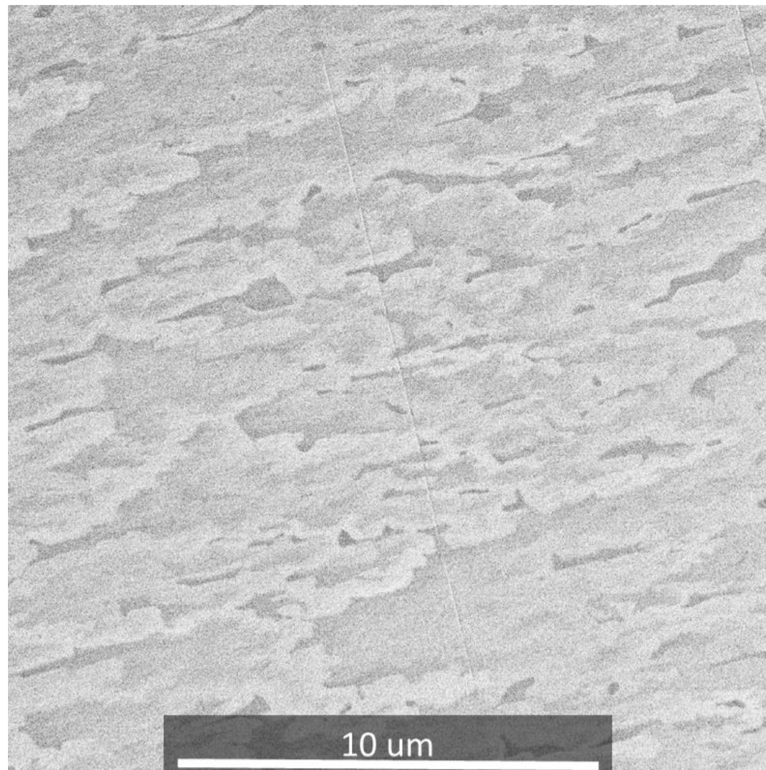

Figure VIII-5 ECCI image of a 25nm $Er_{0.3}Ga_{0.7}Sb$ film grown on a GaSb substrate. The only defects with observable strain fields on the sample are misfit dislocations, one of which can be seen in the center of the image. The spiral macrostep structure is not observed on this surface. ECCI performed by Patrick Callahan

One benefit of the ECCI measurement is that the backscattered electrons in the measurement clearly show the high Z ErSb nanowires. Figure VIII-6 shows SEM images

taken in the ECCI channeling conditions Figure VIII-6(a), backscatter mode Figure VIII-6(b), and secondary electron mode Figure VIII-6(c). Since the ErSb is a very similar crystal structure to the GaSb many of the channeling conditions work for both phases as a result the ECCI image only shows ErSb nanowires directly on the surface before channeling is occurring, deeper nanowires are invisible due to the channeling effect, in contrast the backscatter image shows all nanowires throughout the 25nm thick layer, and the secondary electron image primarily shows the shape of the macrostep. The ECCI image in Figure VIII-6(a) clearly shows that the surface nanowires near areas of recent growth such as the macrostep edge and the notch feature in the top right are smaller and less dense, this agrees nicely with the results from STM and TEM which suggest macrostep flow occurs during growth, and nanowire coverage is a function of exposure time. There is potentially a defect located in the center of the macrostep in Figure VIII-6, however, the small white point is clearly observed in both backscatter and secondary

electron images as well indicating it is a surface feature and not a buried defect responsible for macrostep nucleation.

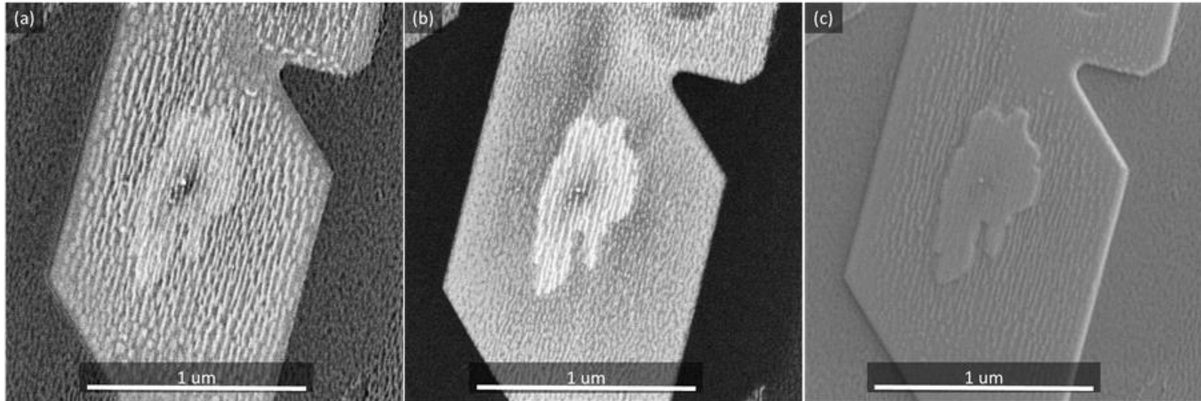

Figure VIII-6 A macrostep on a 25nm $Er_{0.3}Ga_{0.7}Sb(001)$ surface imaged in three different modes, (a) ECCI electron channeling effects hide nanowires within the sample only nanowires lying on the surface are clearly visible, regions of new growth near the notch feature and macrostep edges are observed to have smaller and less dense nanowires. (b) Backscatter electron image tilted 2.5° out of the channeling condition used for figure (a), nanowires from layers beneath the surface are clearly visible. (c) Secondary electron image showing surface features of the macrostep. ECCI performed by Patrick Callahan.

C. Surface Energy Model

Previously the nanowire surface energy was given as a possible explanation for the driving force responsible for the changes in nanowire morphology as a function of Er concentration.[53] However, this hypothesis fails to explain the initial growth of $Er_{0.3}Ga_{0.7}Sb$ consisting of out-of-plane nanowires with horizontal growth beginning after the first layer is terminated by a macrostep. We postulate that it is not the surface energy of the nanowires driving the transition but instead the total surface area of the GaSb{110} surface. This driving force can be easily explained by a simple model which compares the surface energy of the GaSb in the vertical nanowire (VNW) growth regime, where excess GaSb grows around nanoparticles creating a porous structure with GaSb{110}

sidewalls, and horizontal nanowires, where the excess GaSb which previously formed the pits around the nanoparticles is condensed into a single large rectangular macrostep on the surface, a schematic of these two surface morphologies is shown in Figure VIII-7(a).

The total surface energy of a surface is given by

$$(1)\ E = \sum s_{GaSb\{110\}}\,\gamma_{GaSb\{110\}} + \sum s_{GaSb(001)}\,\gamma_{GaSb(001)} + \sum s_{ErSb(001)}\,\gamma_{ErSb(001)} + \sum s_{\frac{ErSb}{GaSb(001)}}\,\gamma_{\frac{ErSb}{GaSb(001)}}$$

The $S_{GaSb\{110\}}$, $S_{GaSb\{001\}}$, $S_{ErSb(001)}$, $S_{ErSb/GaSb(001)}$, terms in equation (1) represent the surface areas of the GaSb{110}/vacuum, GaSb(001)/vacuum, ErSb(001)/vacuum surfaces and the buried GaSb(001)/ErSb(001) interface formed when a macrostep overgrows a nanowire, the $\gamma_{GaSb\{110\}}$, $\gamma_{GaSb(001)}$, $\gamma_{ErSb(001)}$, $\gamma_{ErSb/GaSb(001)}$, terms represent the surface energies of the GaSb{110}/vacuum, GaSb(001)/vacuum, ErSb(001)/vacuum surfaces and the buried GaSb(001)/ErSb(001) interface. The buried interfaces between the ErSb nanowires and GaSb matrix not explicitly shown in equation 1 have equivalent surface areas in both horizontal and vertical nanowire morphologies. In this model it is assumed that the surface area of GaSb(001) and ErSb(001) is unchanged directly before and after the transition occurs, and that when calculating ΔE, the difference between the total surface energy of the in-plane nanowires ($E_{/\!/}$) and the total surface energy of the vertical nanowires ($E_{\perp}$) cancel resulting in equation (2).

$$(2)\ \Delta E = E_{\parallel} - E_{\perp} = \sum s_{GaSb\{110\}}\,\gamma_{GaSb\{110\}} + \sum s_{\frac{ErSb}{GaSb\{001\}}}\,\gamma_{\frac{ErSb}{GaSb\{001\}}} - \sum s'_{GaSb\{110\}}\,\gamma_{GaSb\{110\}}$$

Where the $S_{GaSb\{110\}}$ and $S_{ErSb/GaSb\{001\}}$ terms represent the in-plane nanowire surface and the $S'_{GaSb\{110\}}$ represents the out-of-plane surface. The transition between surfaces occurs when ΔE = 0 which results in the ratio shown in equation 3.

$$(3)\ \frac{E_{\parallel}}{E_{\perp}} = 1 = \frac{\sum s_{GaSb\{110\}}\gamma_{GaSb\{110\}} + \sum s_{\frac{ErSb}{GaSb\{001\}}}\gamma_{\frac{ErSb}{GaSb\{001\}}}}{\sum s'_{GaSb\{110\}}\gamma_{GaSb\{110\}}}.$$

Substituting for particle and macrostep dimensions, assuming square-based pits around vertical nanowires, and square macrostep features results in the expression

$$(4)\ \frac{E_{\parallel}}{E_{\perp}} = C_1\frac{\sqrt{(1-x)}}{x} + C_2(1-x).$$

$$C_1 = \frac{h_{ms} l_{pit}\sqrt{\frac{Ah_{pit}}{h_{ms}}}}{h_{pit}A},\ C_2 = \frac{\gamma_{GaSb/ErSb}}{\gamma_{GaSb\{110\}}}\frac{l_{pit}}{4h_{ms}},$$

Where h_{ms} is the height of the macrostep, l_{pit} and h_{pit} are the base length and height of a vertical nanowire pit, x is the Er content where x = 1 is pure ErSb, A is the total surface area contributing to macrostep formation. This model is plotted in Figure VIII-7, values of h_{ms}=7nm, l_{pit}=4nm, and h_{pit}=1.5nm were estimated from STM measurements, the surface energy component of C_2 is unknown, a value of $\frac{\gamma_{GaSb/ErSb}}{\gamma_{GaSb\{110\}}} = 8$ was used as it results in a crossover similar to what is observed in experiment, however, the C_2 term is not dominant and changes merely shift the position of the HNW/VNW crossover without impacting the overall shape of the plot. Several different values of A can be seen plotted in . A represents the area of the surface contributing GaSb to a single macrostep and

would vary based on the temperature-dependent diffusion length of Ga on the surface. The model predicts that the Er content required to reach the critical threshold of macrostep formation will monotonically decrease as substrate growth temperature increases. This theory provides a clear driving force for macrostep formation motivated from the better surface to volume ratio achieved for GaSb{110} surfaces at higher Er concentrations.

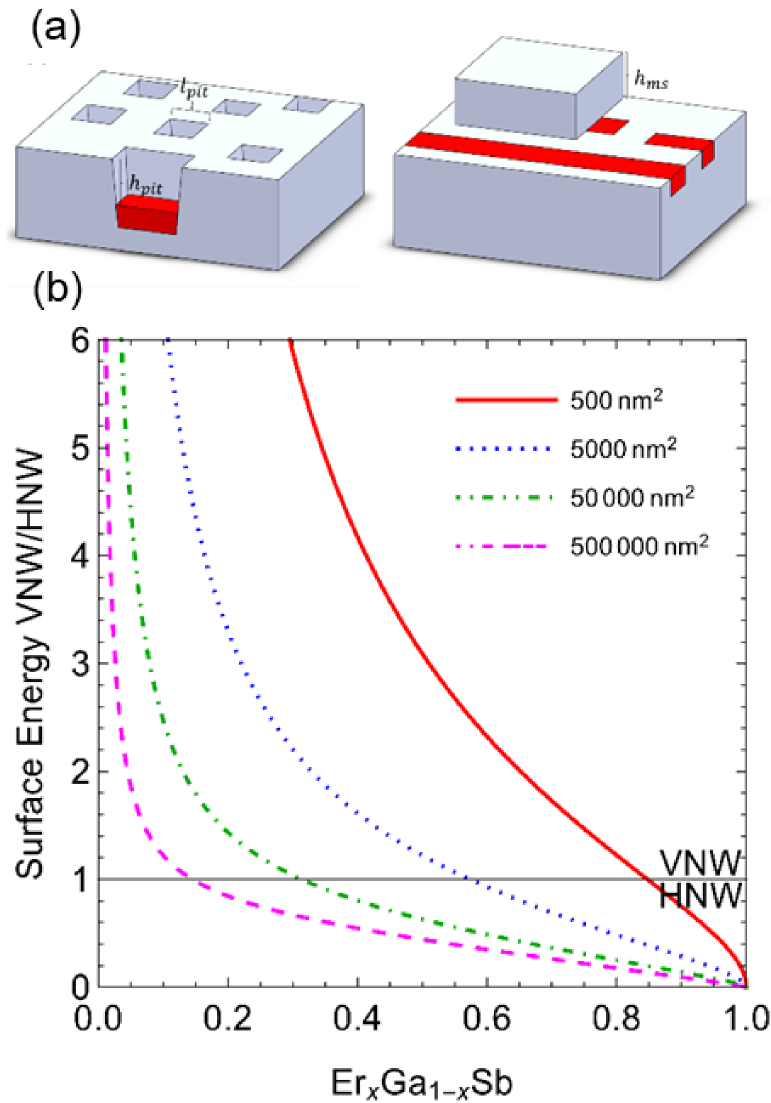

Figure VIII-7 (a) Diagram showing the two surface configurations used in the model. The macrostep on the right is comprised of the GaSb above the nanoparticles (hpit). (b) Plot of equation 2 showing the ratio of surface energies between vertical nanowire and horizontal nanowire surface morphologies. The transition occurs at lower Er concentrations as surface area contribution to a single macrostep increases. The different lines represent different values for the area parameter A.

D. Horizontal nanowire formation mechanism

A thermodynamic driving force for macrostep formation has been established, however, there remains a number of surface features that are unexplainable by thermodynamics implying that the surface is heavily influenced by kinetics as well, as would be expected since MBE growth is not an equilibrium process. The model assumes

a constant height of 7nm for the macrosteps based on the STM images, however, the GaSb(001) surface has a greater surface energy than the GaSb{110} or GaSb{111} indicating that either taller macrosteps or some form of faceting would be more energetically favorable if surface energies were the only consideration.[123] Other features only explainable by kinetics include macrosteps forming more complex structures than large islands on the growth surface, and the elongation of nanoparticles to horizontal nanowires.

Horizontal nanowire formation can be explained if the surface energy of the ErSb{110}/vacuum interface is much larger than the ErSb(001)/vacuum interface and rather than extending a vertical nanowire above the GaSb plane the ErSb instead prefers to diffuse to the edge of a nanowire and embed itself in the GaSb matrix. This situation only arises when macrostep formation has removed the pits that surround ErSb particles at lower Er content. The elongation of nanoparticles is due to the assymetric diffusion rates of the (2x6) reconstructed GaSb(001) surface which has an easy diffusion direction down the dimer rows along the [1$\bar{1}$0], a feature seen on similar surface reconstructions in GaAs.[124]

Macrostep morphology is more difficult to explain but may be related to changes in step flow growth brought about by ErSb particles lying in plane with the surface. Typically during stepflow growth diffusion rates are high enough that no attachment on the terrace occurs, Ga adatoms will diffuse all the way to a step edge where bonding is more favorable before bonding. The type of step-flow growth can be characterized by the probability of an adatom attaching to an upstep versus a downstep: when the upstep

is more favored terrace growth is driven towards equally spaced terraces and is the growth mode seen in step flow growth of pure GaSb,[87] but if the down step is favored, large terraces outgrow smaller terraces and step bunching occurs.[87] Here it is proposed that a shift in attachment rate at step edges occurs during ErSb growth due to the presence of dense ErSb coverage observed at the base of macrosteps. This can be considered schematically in Figure VIII-8(a), the arrows indicate the proposed motion of Ga adatoms across the surface. In this growth model Ga adatoms do not adhere at the base of a macrostep due to the ErSb present, growth instead occurs at the downstep of a macrostep. Evidence of this can be seen in Figure VIII-3(b), from the STM images a the consequences of a Schowebel barrier are observed at the downstep,[125] this reduces the number of Ga adatoms moving over the macrostep edge. The Schowebel barrier is responsible for the single monolayer steps growing backwards from the downstep, however, no similar monolayer step growth is observed from the base of the macrostep indicating that Ga adatoms are almost completely reflected at that barrier and that growth must occur almost entirely at the macrostep with a small amount of Ga adatoms depositing on the surface near the macrostep edge due to the Schowebel barrier. Figure VIII-8(b) shows a ball and stick model of the unfavorable atomic bonding that would occur as a GaSb step overgrows an ErSb nanoparticle.[126]

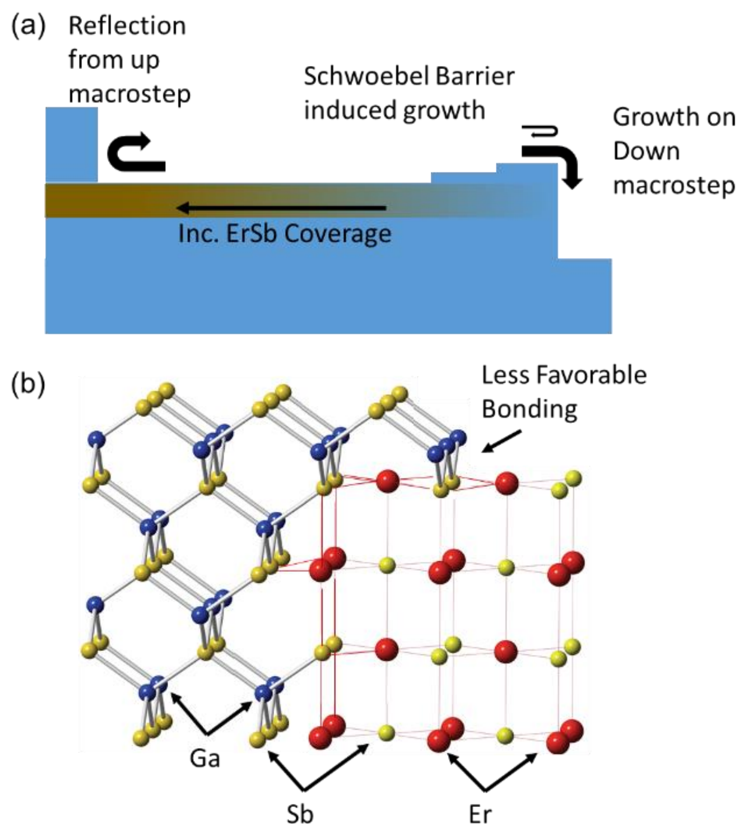

Figure VIII-8 (a) Diagram showing the growth model for Ga adatoms diffusing along the surface. Ga adatoms reflect from the bottom of a macrostep, majority of growth occurs from the top edge of a macrostep, some growth occurs on the leading edge of the macrostep due to the Schwoebel barrier. (b) Ball and stick model showing overgrowth of an ErSb nanoparticle by GaSb.

Some similarities to this suggested growth mode are observed in other material systems, most notably the growth of $Si_{.985}C_{.015}$ by MBE on a (118) Si substrate.[127] Kinetic Monte Carlo simulations predict step bunching to occur when an added impurity reduces the binding energy of the adatoms thereby increasing their diffusivity,[128] an interaction observed here due to Ga adatoms preference to avoid nucleating on ErSb particles. The large difference in the observed threshold concentration needed to form macrosteps, 1.5% C in Si[127] and 30% Er in GaSb can be explained by the presence of ErSb in pits during vertical nanowire growth Figure VIII-2, where the pits counteract the increase in diffusivity the ErSb would otherwise generate, once nanoparticles lie in plane

with the surface the change in surface diffusivity further favors macrostep growth. The beginning of the transition to horizontal nanowires can be seen in Figure VIII-9. Observed step bunching may indicate the beginning of macrostep formation, simultaneously ErSb particles are observed to be located just one monolayer below the growth surface, instead of recessed in pits, as expected from the proposed mechansim.

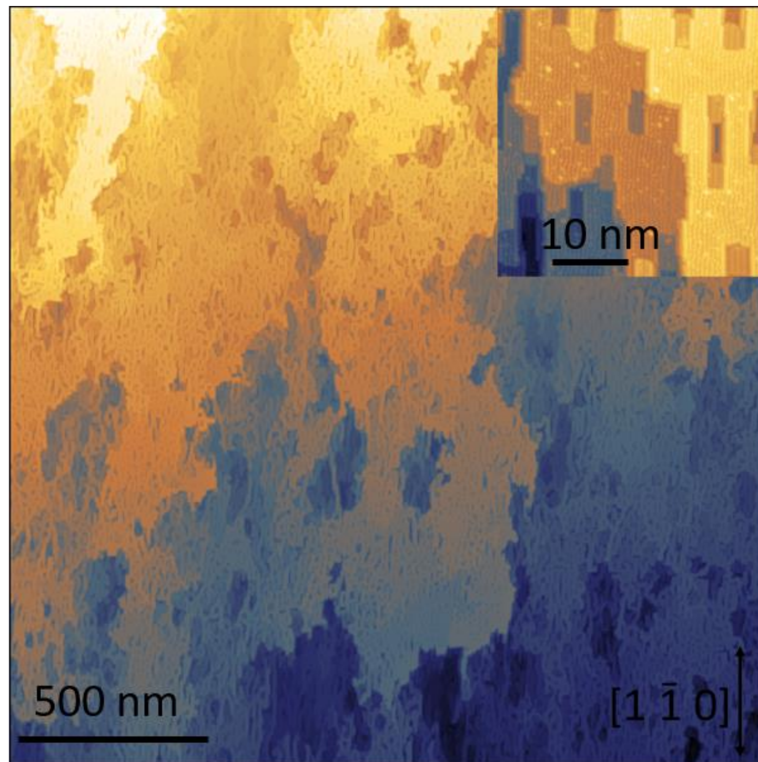

Figure VIII-9 STM of 7.5 nm of $Er_{0.3}Ga_{0.7}Sb(001)$ the beginning of step bunching can be seen. Inset shows ErSb nanoparticles are present one monolayer below the growth plane.

E. Low temperature growth mode

During the exploration of horizontal nanowire growth one of the parameters adjusted was the substrate temperature during growth, this led to an unexpected discovery, a low temperature nanowire growth mode previously unobserved. The new

low temperature growth mode also results in horizontal nanowires, see Figure VIII-10 which shows low temperature nanowires grown at a substrate temperature of 480°C with codeposition of $Er_{0.15}Ga_{0.85}Sb$. In order to differentiate the low temperature nanowires from the horizontal nanowires grown by the high temperature growth mode the low temperature nanowires will be referred to as nanofilaments in reference to their smaller size.

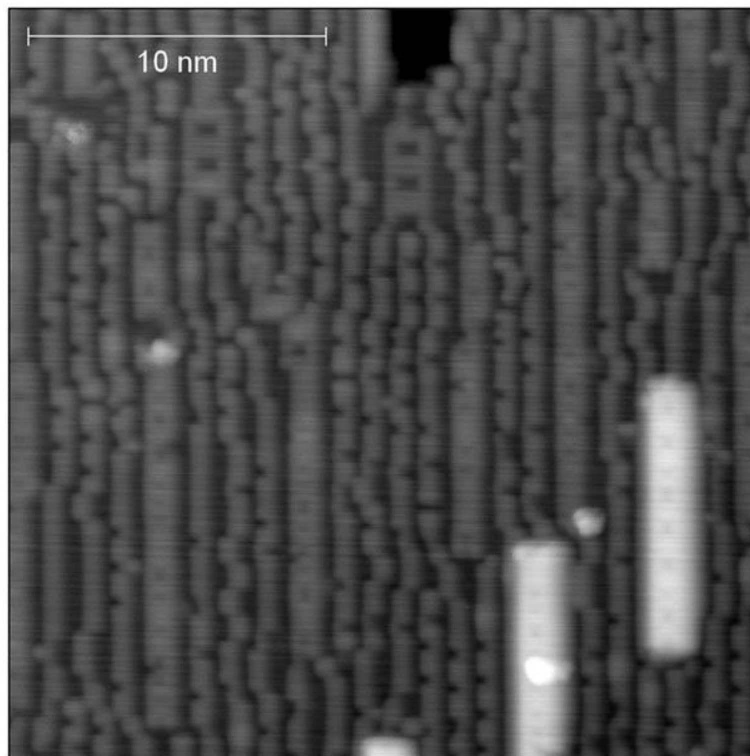

Figure VIII-10 STM image showing horizontal nanowires grown at a substrate temperature 480°C. Sample was grown by codeposition of $Er_{0.15}Ga_{0.85}Sb$. STM image taken at 77K with a -2V tip bias.

The nanofilaments are particularly interesting as they do not grow by the embedded growth mode observed at higher temperatures. The difference in growth mode is easily observed in Figure VIII-11, which shows the deposition of 0.15 monolayers of Er onto a GaSb buffer layer with an Sb overpressure at two different temperatures. For

Figure VIII-11(a) the substrate was at 480°C and the formation of nanofilaments is clearly seen across the surface. In Figure VIII-11(b) the substrate was at 520°C and a much less dense coverage of ErSb particles is observed. This result shows that at 520°C the embedded growth mode is at work. ErSb surface coverage is 3.7% a value consistent with the embedded growth mode where 3 monolayers of ErSb are embedded beneath the surface, giving an equivalent ErSb coverage of 14.8% very close to the deposited amount of Er. In contrast the surface coverage of the 480°C samples has ErSb surface coverage of 15.75% indicating that no ErSb has embedded itself and all of it is lying directly on the surface.

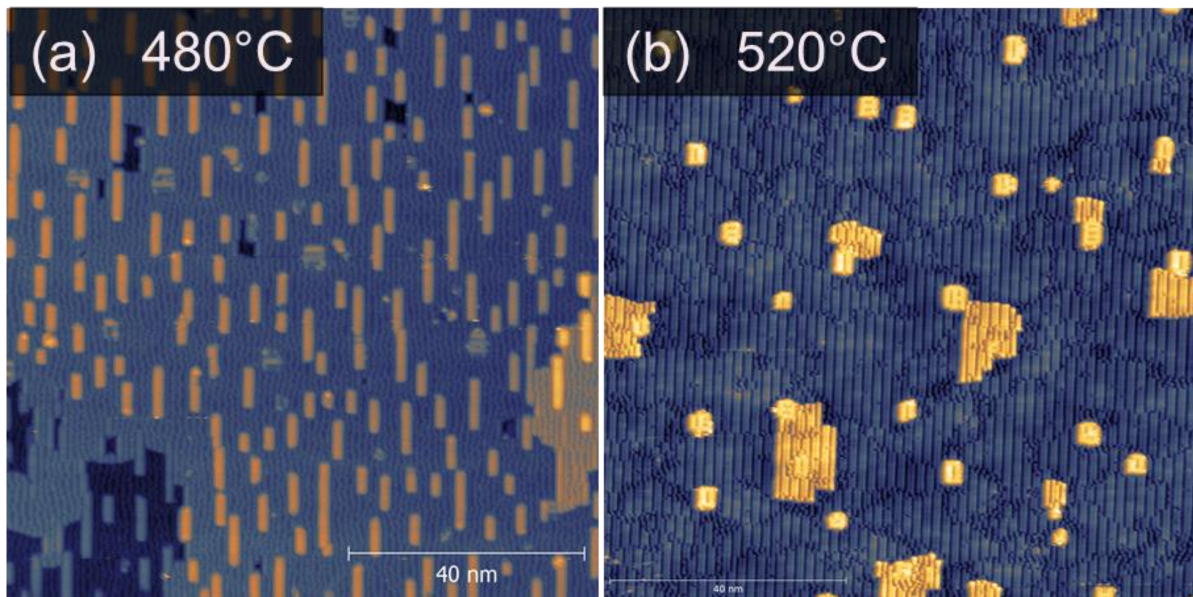

Figure VIII-11 STM topographic images showing 0.15 monolayers of ErSb deposited at a temperature 480°C (a) which shows no embedded growth and a surface coverage of 14.8%, and 520°C (b) which shows the expected embedded growth mode and a surface coverage of 3.7%.

The transition appears to occur between 480°C-520°C when the sample is grown on an STM adapter block. In order to get a better idea of the nanowire structure in the out of plane direction a sample was grown with a normal VG growth block (substrate

temperature behaves slightly differently on VG blocks vs STM blocks) with a superlattice structure of 20nm thick nanowire layers spaced by ~100 nm layers of GaSb. The first layer was grown at 520°C and each successive layer was grown at a temperature 20°C cooler, the layers for temperatures from 460°C to 400°C can be seen in Figure VIII-12. In contrast to the nanowires seen in STM all of the nanowires seen in STEM correspond to the larger embedded nanowires seen at higher temperatures. The difference in temperature between the two types of substrate blocks STM and VG only corresponds to a temperature difference of a few 10's of degrees at most, not enough to explain the lack of nanofilament formation at 400°C when nanofilaments were clearly observed at 480°C on STM samples. While it is possible that the nanofilaments somehow coalesce to form larger nanowires, the more likely explanation involves Sb overpressure. Immediately after growth of the sample shown in Figure VIII-12 it was discovered that the Sb source in the MBE chamber had a blockage drastically limiting the Sb flux on the sample this would imply that the transition between nanowires and nanofilaments is partly due to temperature and partly due to Sb overpressure.

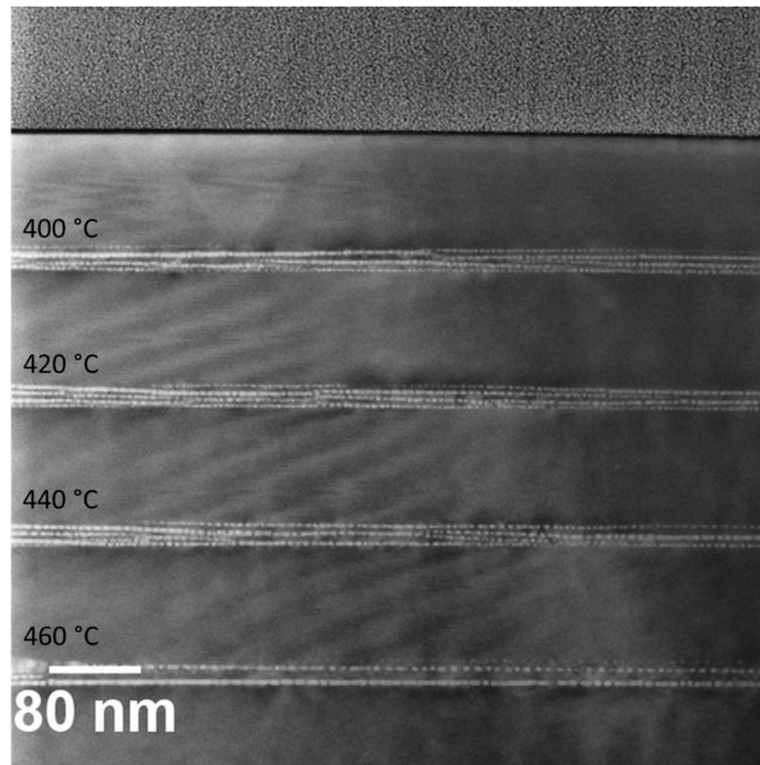

Figure VIII-12 STEM image showing ErSb nanowires grown at several varying temperatures with GaSb buffers between each layer. Large embedded growth mode nanowires are observed at all temperature likely due to a decrease in Sb pressure identified after growth. Image taken by Dan Pennachio.

A dependence on Sb overpressure is logical given that it is known from the embedded growth mode that Er will react with GaSb. It stands to reason that the way of preventing this reaction is to slow it down by decreasing temperature and to provide an alternate source of Sb for ErSb formation. This also helps to explain a discrepancy seen between the work presented in this thesis and previous work in our group by Jason Kawasaki, which showed the embedded nanowire formation occurring at temperatures well below where the transition to nanofilaments is observed in this work.[53] This discrepancy is due to a change in Sb source where the Sb cell and cracker was upgraded on the MBE system allowing for much higher Sb flux and growth rates. To explore this 0.15 monolayers of Er was deposited on a GaSb (001) surface with a decreased Sb

pressure at 480°C, unfortunately due to a broken flux gauge a true quantitative comparison of the Sb flux in each case is not possible but an estimate from GaSb growth rates suggests that this sample was grown at ~1/10 the Sb overpressure typically used. The surface of the low Sb pressure nanowire sample can be seen in the STM shown in Figure VIII-13, while nanofilament formation is observable on the surface ErSb coverage is 7.8% indicating that at least some of the ErSb is growing by the embedded growth mode. Nanofilaments lying within the plane of the GaSb can also be observed in the leading edge of the step seen in the bottom right corner, this would be consistent with GaSb stepflow growth caused by Ga kicked out during the embedded growth mode and growing around nanofilaments on the surface, the dashed line indicates an approximate edge for the initial step location based on the transition between embedded nanofilaments and filaments lying on the surface.

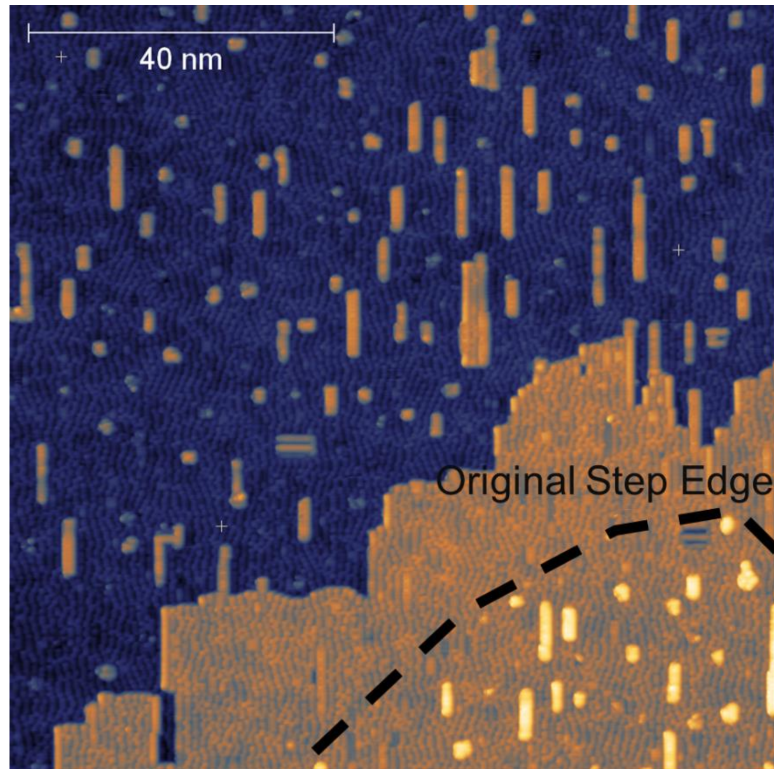

Figure VIII-13 STM image showing a GaSb(001) surface with 0.15 monolayers of Er deposited on top of it in an Sb overpressure ~1/10 the Sb overpressure typically used for nanowire growth. The dashed line indicates an estimate for the original position of the GaSb step shown in the image, growth is thought to have occurred from ejected Ga atoms.

One of the interesting uses for the nanofilament growth mode is a result of the different size scale of the nanoparticles. Figure VIII-14 shows an STM image of the nanofilaments with a to scale inset of the smallest nanoparticles observed with the embedded growth mode. The nanofilaments are approximately half the width of the previously observed smallest nanoparticles with nanofilament width seemingly dependent on the spacing between the GaSb dimer rows. If this is true it would suggest that nanofilaments form when diffusion across the dimer rows is inhibited and nucleated ErSb particles grow when Er flux diffuses along the dimer rows making contact with the nanoparticles only along the $[1\bar{1}0]$ direction. As already mentioned the nanofilaments do not grow by an embedded growth mode this implies that they are thinner than

embedded nanowires which by default form with a minimum thickness of 4 monolayers (~1.2 nm) while the nanofilaments are only 1 monolayer (~0.3 nm) thick.

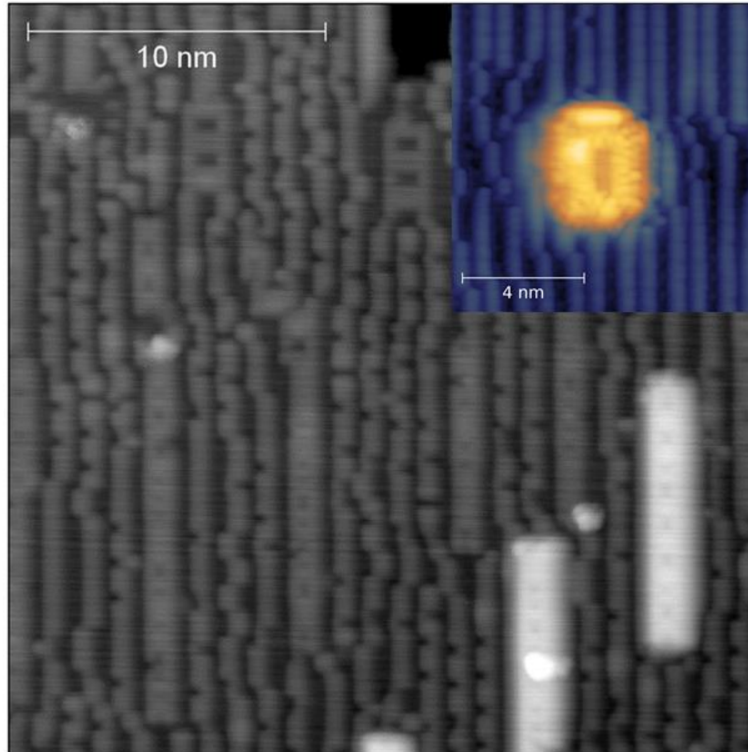

Figure VIII-14 STM topographic image of the nanofilament growth mode observed during codeposition of $Er_{0.3}Ga_{0.7}Sb$ *at a substrate temperature of 480°C. (Inset) a to scale STM image of one of the smallest nanoparticles observed in the embedded growth regime.*

Work has already been done on the larger ErSb nanoparticles which investigated the response of nanowires to terahertz radiation, it was found that plasmons on the nanowires were present and enabled the structures to act as polarizers. Given the dependence of plasmon frequency on nanoparticle size and the smaller size of the nanofilaments they may produce interesting changes in plasmon response.[129] Also while not observed in the ErSb/GaSb material system smaller nanoparticles will enhance confinement effects in material sys tems with sufficiently large band offsets.

F. Conclusions and Future Work

It was shown that the transition from vertical to horizontal nanowires in the ErSb/GaSb system is the result of a new growth mode brought about by a change in surface morphology. This change is characterized by the presence of large macrosteps and in-plane, rather than recessed ErSb nanoparticles. The orientation of horizontal nanowires is due to the asymmetric diffusion rates of Er on the GaSb (001) surface, resulting in preferential elongation along the [1-10] direction. Vertical structures are prevented from forming due to macrostep growth. The formation of macrosteps is shown to be energetically favorable upon reaching a critical composition of Er, and their presence explains the observed stratification of horizontal nanowires observed in cross-sectional STEM. Knowledge of this macrostep mediated growth mode implies that care must be taken when integrating horizontal nanowires into device heterostructures, especially near sensitive layers. Finally, the underlying mechanism for formation of horizontal nanowires observed here is potentially applicable to any pair of materials with similar diffusion and surface energy properties, other RE-V/III-V pairs are obvious candidates, but others, such as Ge:III-V nanostructures, display similarities as well.

The nanofilaments observed forming at lower growth temperatures have potential applications with terahertz polarizers, their smaller size may shift the plasmon properties of the nanowires. The nanofilaments appear to form without the need of macrostep formation on the surface, possibly enabling nanofilaments to be grown closer to sensitive device layers. Nanofilaments also grow under a wider variety of flux conditions than the embedded growth horizontal nanowires, allowing in-plane nanowire formation at Er concentrations <25%, which was previously not accessible. Finally the

spacing between nanofilaments appears to be small, possibly enabling tunneling conduction at higher Er concentrations which would be useful in creation of a buried contact or back gate.

The next step is to fully characterize the transport properties of the nanowires presented here both for the embedded growth mode and the nanofilaments. It is important to identify transitions between mixed ErSb/GaSb conduction and a potential crossover at high nanowire densities where conduction occurs entirely within the nanowire network. Samples for transport characterization have already begun to be grown and this should be explored shortly.

IX. Summary and Conclusion

In conclusion the examination of three individual materials systems has been presented all of which have key properties that are inherently tied to surfaces or interfaces in the structure.

The presence of two level states, one of the dominating loss factors in the operation of superconducting qubits, is known to be directly related to initial surface of the dielectric material before superconductor deposition. In-situ XPS has been used to identify the possible physical sources of TLS in Al_2O_3/Al and Si/Al superconducting coplanar waveguide structures. Hydrogen was found to be a likely culprit as the removal of O-H bonding on the sapphire surface and a transition from the (1x1) H terminated Si(001) surface to the Si dimer reconstructed (2x2) both coincided with significant improvement in resonator quality factor. Additionally carbon was identified as a possible source of disorder increasing the region suitable for TLS formation at the

superconductor/dielectric interface. A high temperature oxygen anneal of either Ozone, Plasma, or O_2 was shown to be sufficient to remove these contaminants for resonators fabricated on sapphire. However, similar in-situ cleaning procedures for Si resulted in the formation of SiC particles and significant surface roughening. If work is to continue on Si/Al based resonators it was suggested that the feasibility of >1200°C in-situ anneals be explored which would enable diffusion of SiC particles into the substrate and away from the interface. Alternatively an in-situ Si buffer layer could be used to provide a pristine interface layer.

The metal to insulator transition of the $RNiO_3$ material system was explored and shown in the case of $PrNiO_3$ to be controlled by substrate strain. A thin film MIT was observed in $LaNiO_3$ thin films with thicknesses of a few unit cells. In-situ STS was used to probe the density of states of the $LaNiO_3$ in the insulating phase and showed an observable gap, suggesting that the insulating phase is not a purely disorder driven transition. The observed thickness dependent MIT was observed only at the initial $RNiO_3$/substrate interface. When superlattice structures were studied subsequent $LaNiO_3$ layers were observed to be increasingly conductive. This suggests the possibility of tuning properties by superlattice structure exists.

Lastly the growth mechanism for the formation of in-plane nanowires was studied in the $Er_xGa_{1-x}Sb$ material system. The transition was shown to be entirely driven by the morphology of the surface during growth. The presence of pits surrounding out-of-plane ErSb nanowires results in a driving force to reduce surface energy by removing the many pits on the surface and instead forming a fewer number of large macrosteps. The

presence of nanowires on the surface results in nanowire growth transitioning from out-of-plane to in-plane and the stratification of the nanowires is achieved by the overgrowth of the macrosteps. Without in-situ STM the macrosteps and distribution of ErSb across the terraces would have gone unnoticed. A previously unobserved low temperature growth mode was also observed which results in the formation of nanofilaments, extremely narrow nanowires which do not embed themselves in the GaSb surface. Initial studies suggest that the growth mode of the nanofilaments is dependent on the Sb flux and substrate temperature during growth. Formation only occurs when there is sufficient Sb and slow enough kinetics that the ErSb forms before the embedding process has time to occur. Nanofilaments may be ideally suited for use as buried contacts as they occur over a large range of $Er_xGa_{1-x}Sb$ compositions and do not appear to rely on the presence of macrosteps. The general formation of nanowires observed in this material system has the potential to apply to other self-assembled nanoparticles, with obvious analogs to the rest of the RE/V materials but also other potential systems which show some similarities such as Si:Ge nanostructures.

The need for in-situ surface sensitive characterization is only likely to increase in the future, current materials of interest include categories such as topological insulators,[130] and weyl semi-metals.[131] These materials are of interest due to the intriguing surface states they possess which enables Dirac points, scattering protected spin polarization, and Fermi arcs, properties that are of particular importance to the fields of spintronics, and quantum computing. Since these are surface states they all require the use of surface sensitive techniques such as angle resolved photo-emission spectroscopy,[130] or quasi-particle interference maps observed in STM to

characterize.[132] These techniques rely on pristine sample surfaces if the characterization facility is not in-situ it typically requires a sample to be cleaved in vacuum just prior to measurement but this limits the surfaces observable to just cleavage planes for the crystal, which often differ from the surfaces and interfaces used in actual devices.

Unfortunately many of the interesting STM measurements require long scanning periods and very low levels on noise in the system. These requirements are at odds with including the STM as part of a larger growth system, as noise is minimized when the STM is isolated in a separate room. This creates an unfortunate conflict between accessing the greatest number of pristine surfaces and enabling the largest number of possible experiments. This problem exists to a lesser extent with XPS and ARPES techniques. These techniques do not require the same level of low background vibration, but many of the exciting experiments, such as spin polarized ARPES, require a beamline facility. This again means that samples must be exposed to air and are limited to surfaces which can be cleaved, or capped and desorbed.

Luckily, “in-situ” is becoming much larger and cheaper, with the improvements in vacuum technology the Palmstrøm research group, spearheaded by work from Jay Logan, has developed a vacuum suitcase which enables samples to be moved from the growth system to other characterization systems without breaking vacuum. The vacuum suitcase has already successfully transported samples between the growth facility and the Advanced Light Source, a journey in excess of 300 miles, without surface contamination occurring. This same technology allows in-situ STM setups while still

maintaining low noise environments. Technologies such as this will drastically increase the amount of surface characterization available for research groups everywhere ensuring the field will continue to grow in the future as demand for surface sensitive techniques increases.

X. References

[1] H. Kroemer, “Nobel lecture: Quasielectric fields and band offsets: Teaching electrons new tricks,” *Reviews of Modern Physics*, vol. 73, no. 3. pp. 783–793, 2001.

[2] F. Schmidt-Kaler, M. Riebe, and S. Gulde, “Realization of the Cirac – Zoller controlled-NOT quantum gate,” *Nature*, vol. 422, no. March, p. 408, 2003.

[3] M. H. Devoret, A. Wallraff, and J. M. Martinis, “Superconducting Qubits: A Short Review,” p. 41, 2004.

[4] J. J. Pla, K. Y. Tan, J. P. Dehollain, W. H. Lim, J. J. L. Morton, D. N. Jamieson, A. S. Dzurak, and A. Morello, “A single-atom electron spin qubit in silicon.,” *Nature*, vol. 489, no. 7417, pp. 541–5, 2012.

[5] J. R. Petta, “Coherent Manipulation of Coupled Electron Spins in Semiconductor Quantum Dots,” *Science (80-.).*, vol. 309, no. 5744, pp. 2180–2184, Sep. 2005.

[6] A. G. Fowler, M. Mariantoni, J. M. Martinis, and A. N. Cleland, “Surface codes: Towards practical large-scale quantum computation,” *Phys. Rev. A - At. Mol. Opt. Phys.*, vol. 86, no. 3, 2012.

[7] S. Gazibegovic, D. Car, H. Zhang, S. C. Balk, J. A. Logan, M. W. A. de Moor, M. C. Cassidy, R. Schmits, D. Xu, G. Wang, P. Krogstrup, R. L. M. O. het Veld, J. Shen, D. Bouman, B. Shojaei, D. Pennachio, J. S. Lee, P. J. van Veldhoven, S. Koelling, M. A. Verheijen, L. P. Kouwenhoven, C. J. Palmstrøm, and E. P. A. M. Bakkers, “Epitaxy of Advanced Nanowire Quantum Devices,” 2017.

[8] R. Barends, J. Kelly, A. Megrant, D. Sank, E. Jeffrey, Y. Chen, Y. Yin, B. Chiaro, J. Mutus, C. Neill, P. O’Malley, P. Roushan, J. Wenner, T. C. White, A. N. Cleland, and J. M. Martinis, “Coherent josephson qubit suitable for scalable quantum integrated circuits,” *Phys. Rev. Lett.*, vol. 111, no. 8, pp. 1–5, 2013.

[9] P. W. Anderson, B. I. Halperin, and C. M. Varma, “Anomalous low-temperature thermal properties of glasses and spin glasses,” *Philos. Mag.*, vol. 25, no. 1, pp. 1–9, Jan. 1972.

[10] W. A. Phillips, “Tunneling states in amorphous solids,” *J. Low Temp. Phys.*, vol. 7, no. 3–4, pp. 351–360, 1972.

[11] W. A. Phillips, “Two-level states in glasses,” *Reports Prog. Phys.*, vol. 50, no. 12, pp. 1657–1708, Dec. 1987.

[12] K. Agarwal, I. Martin, M. D. Lukin, and E. Demler, “Polaronic model of two-level systems in amorphous solids,” *Phys. Rev. B - Condens. Matter Mater. Phys.*, vol. 87, no. 14, pp. 1–14, 2013.

[13] A. M. Holder, K. D. Osborn, C. J. Lobb, and C. B. Musgrave, “Bulk and surface tunneling hydrogen defects in alumina,” *Phys. Rev. Lett.*, vol. 111, no. 6, pp. 1–5, 2013.

[14] L. Faoro and L. B. Ioffe, “Microscopic origin of critical current fluctuations in large,

small, and ultra-small area Josephson junctions," *Phys. Rev. B - Condens. Matter Mater. Phys.*, vol. 75, no. 13, pp. 1–4, 2007.

[15] L. Faoro, J. Bergli, B. L. Altshuler, and Y. M. Galperin, "Models of environment and T1 relaxation in Josephson charge qubits," *Phys. Rev. Lett.*, vol. 95, no. 4, pp. 1–4, 2005.

[16] J. Wenner, R. Barends, R. C. Bialczak, Y. Chen, J. Kelly, E. Lucero, M. Mariantoni, A. Megrant, P. J. J. O'Malley, D. Sank, A. Vainsencher, H. Wang, T. C. White, Y. Yin, J. Zhao, A. N. Cleland, and J. M. Martinis, "Surface loss simulations of superconducting coplanar waveguide resonators," *Appl. Phys. Lett.*, vol. 99, no. 11, pp. 2009–2012, 2011.

[17] A. Megrant, C. Neill, R. Barends, B. Chiaro, Y. Chen, L. Feigl, J. Kelly, E. Lucero, M. Mariantoni, P. J. J. O'Malley, D. Sank, A. Vainsencher, J. Wenner, T. C. White, Y. Yin, J. Zhao, C. J. Palmstrøm, J. M. Martinis, and A. N. Cleland, "Planar superconducting resonators with internal quality factors above one million," *Appl. Phys. Lett.*, vol. 100, no. 11, 2012.

[18] J. M. Sage, V. Bolkhovsky, W. D. Oliver, B. Turek, and P. B. Welander, "Study of loss in superconducting coplanar waveguide resonators," *J. Appl. Phys.*, vol. 109, no. 6, 2011.

[19] R. J. Cava, B. Batlogg, R. B. van Dover, D. W. Murphy, S. Sunshine, T. Siegrist, J. P. Remeika, E. A. Rietman, S. Zahurak, and G. P. Espinosa, "Bulk superconductivity at 91 K in single-phase oxygen-deficient perovskite Ba2YCu3O9-d," *Phys. Rev. Lett.*, vol. 58, no. 16, pp. 1676–1679, Apr. 1987.

[20] Millis, Shraiman, and Mueller, "Dynamic Jahn-Teller Effect and Colossal Magnetoresistance in La 1-xSrxMnO3.," *Phys. Rev. Lett.*, vol. 77, no. 1, pp. 175–178, 1996.

[21] M. Uehara, S. Mori, C. H. Chen, and S. W. Cheong, "Percolative phase separation underlies colossal magnetoresistance in mixed-valent manganites," *Nature*, vol. 399, no. June, pp. 560–563, 1999.

[22] B. Jalan, S. Stemmer, S. Mack, and S. J. Allen, "Two-dimensional electron gas in δSrTiO3," *Phys. Rev. B*, vol. 82, no. 8, p. 81103, Aug. 2010.

[23] A. Ohtomo and H. Y. Hwang, "Corrigendum: A high-mobility electron gas at the LaAlO3/SrTiO3 heterointerface," *Nature*, vol. 441, no. 7089, pp. 120–120, May 2006.

[24] J. B. Torrance, P. Lacorre, A. I. Nazzal, E. J. Ansaldo, and C. Niedermayer, "Systematic study of insulator-metal transitions in perovskites RNiO3 (R=Pr,Nd,Sm,Eu) due to closing of charge-transfer gap," *Phys. Rev. B*, vol. 45, no. 14, pp. 8209–8212, 1992.

[25] C. Kittel, *Introduction to Solid State Physics*. New York: Wiley, 1996.

[26] N. F. Mott, "The Basis of the Electron Theory of Metals, with Special Reference to the Transition Metals," *Proc. Phys. Soc. A*, vol. 62, pp. 416–422, 1949.

[27] G. Catalan, “Progress in perovskite nickelate research,” *Phase Transitions*, vol. 81, no. 7–8, pp. 729–749, 2008.

[28] J. Zaanen, G. A. Sawatzky, and J. W. Allen, “Band gaps and electronic structure of transition-metal compounds,” *Phys. Rev. Lett.*, vol. 55, no. 4, pp. 418–421, 1985.

[29] U. Staub, G. I. Meijer, F. Fauth, R. Allenspach, J. G. Bednorz, J. Karpinski, S. M. Kazakov, L. Paolasini, and F. D’Acapito, “Direct Observation of Charge Order in an Epitaxial NdNiO3 Film,” *Phys. Rev. Lett.*, vol. 88, no. 12, p. 126402, 2002.

[30] J. Son, S. Rajan, S. Stemmer, and S. James Allen, “A heterojunction modulation-doped Mott transistor,” *J. Appl. Phys.*, vol. 110, no. 8, 2011.

[31] D. Jung, J. Faucher, S. Mukherjee, A. Akey, D. J. Ironside, M. Cabral, X. Sang, J. Lebeau, S. R. Bank, T. Buonassisi, O. Moutanabbir, and M. L. Lee, “Highly tensile-strained Ge/InAlAs nanocomposites,” *Nat. Commun.*, vol. 8, pp. 1–7, 2017.

[32] O. I. Lebedev, J. Verbeeck, G. Van Tendeloo, O. Shapoval, A. Belenchuk, V. Moshnyaga, B. Damashcke, and K. Samwer, “Structural phase transitions and stress accommodation in (La0.67Ca0.33MnO3)1-x:(MgO)x composite films,” *Phys. Rev. B*, vol. 66, no. 10, p. 104421, Sep. 2002.

[33] H. Lu, P. G. Burke, A. C. Gossard, G. Zeng, A. T. Ramu, J. H. Bahk, and J. E. Bowers, “Semimetal/semiconductor nanocomposites for thermoelectrics,” *Adv. Mater.*, vol. 23, no. 20, pp. 2377–2383, 2011.

[34] M. Geoghegan, R. A. L. Jones, R. S. Payne, P. Sakellariou, A. S. Clough, and J. Penfold, “Lamellar structure in a thin polymer blend film,” *Polymer (Guildf).*, vol. 35, no. 10, pp. 2019–2027, 1994.

[35] H. Lu, D. G. Ouellette, S. Preu, J. D. Watts, B. Zaks, P. G. Burke, M. S. Sherwin, and A. C. Gossard, “Self-assembled ErSb nanostructures with optical applications in infrared and terahertz,” *Nano Lett.*, vol. 14, no. 3, pp. 1107–1112, 2014.

[36] D. Leonard, M. Krishnamurthy, C. M. Reaves, S. P. Denbaars, and P. M. Petroff, “Direct formation of quantum-sized dots from uniform coherent islands of InGaAs on GaAs surfaces,” *Appl. Phys. Lett.*, vol. 63, no. 23, pp. 3203–3205, 1993.

[37] J. W. Cahn, “On spinodal decomposition,” *Acta Metall.*, vol. 9, no. 9, pp. 795–801, Sep. 1961.

[38] C. J. Palmstrøm, N. Tabatabaie, and S. J. Allen, “Epitaxial growth of ErAs on (100)GaAs,” *Appl. Phys. Lett.*, vol. 53, no. 26, pp. 2608–2610, 1988.

[39] D. C. Driscoll, M. P. Hanson, E. Mueller, and A. C. Gossard, “Growth and microstructure of semimetallic ErAs particles embedded in an In0.53Ga0.47As matrix,” *J. Cryst. Growth*, vol. 251, no. 1–4, pp. 243–247, 2003.

[40] A. Guivarc’h, A. Le Corre, P. Auvray, B. Guenais, J. Caulet, Y. Ballini, R. Gúcrin, S. Députier, M. C. Le Clanche, G. Jézéquel, B. Lépine, A. Quémerais, and D. Sébilleau, “Growth by molecular beam epitaxy of (rare-earth group V element)/III-V

semiconductor heterostructures," *J. Mater. Res.*, vol. 10, no. 8, pp. 1942–1952, 1995.

[41] E. M. Krivoy, H. P. Nair, A. M. Crook, S. Rahimi, S. J. Maddox, R. Salas, D. A. Ferrer, V. D. Dasika, D. Akinwande, and S. R. Bank, "Growth and characterization of LuAs films and nanostructures," *Appl. Phys. Lett.*, vol. 101, no. 14, p. 141910, Oct. 2012.

[42] A. G. Petukhov, W. R. L. Lambrecht, and B. Segall, "Electronic structure and magnetism of the semimetals ErAs and ErxSc1-xAs," *Phys. Rev. B*, vol. 50, no. 11, pp. 7800–7804, 1994.

[43] W. R. L. Lambrecht, B. Segall, A. G. Petukhov, R. Bogaerts, and F. Herlach, "Spin-orbit effects on the band structure and Fermi surface of ErAs and Er_xSc_1-xAs," *Phys. Rev. B*, vol. 55, no. 15, pp. 9239–9242, 1997.

[44] C. Kadow, J. A. Johnson, K. Kolstad, J. P. Ibbetson, and A. C. Gossard, "Growth and microstructure of self-assembled ErAs islands in GaAs," *J. Vac. Sci. Technol. B*, vol. 18, no. 4, pp. 2197–2203, 2000.

[45] C. Kadow, A. W. Jackson, A. C. Gossard, J. E. Bowers, S. Matsuura, and G. A. Blake, "Self-assembled ErAs islands in GaAs for THz applications," *Phys. E Low-Dimensional Syst. Nanostructures*, vol. 7, no. 1, pp. 97–100, 2000.

[46] H. P. Nair, A. M. Crook, and S. R. Bank, "Enhanced conductivity of tunnel junctions employing semimetallic nanoparticles through variation in growth temperature and deposition," *Appl. Phys. Lett.*, vol. 96, no. 22, p. 222104, May 2010.

[47] R. Koltun, J. L. Hall, T. E. Mates, J. E. Bowers, B. D. Schultz, and C. J. Palmstrøm, "Thermoelectric properties of single crystal Sc1−xErxAs:InGaAs nanocomposites," *J. Vac. Sci. Technol. B Microelectron. Nanom. Struct.*, vol. 31, no. 4, p. 41401, 2013.

[48] Y. Zhang, K. G. Eyink, L. Grazulis, M. Hill, J. Peoples, and K. Mahalingam, "Stacking InAs quantum dots over ErAs semimetal nanoparticles on GaAs (0 0 1) using molecular beam epitaxy," *J. Cryst. Growth*, pp. 1–6, 2017.

[49] C. C. Bomberger, L. R. Vanderhoef, A. Rahman, D. Shah, D. B. Chase, A. J. Taylor, A. K. Azad, M. F. Doty, and J. M. O. Zide, "Determining the band alignment of TbAs:GaAs and TbAs:In0.53Ga0.47As," *Appl. Phys. Lett.*, vol. 107, no. 10, pp. 0–4, 2015.

[50] P. Dongmo, M. Hartshorne, T. Cristiani, M. L. Jablonski, C. Bomberger, D. Isheim, D. N. Seidman, M. L. Taheri, and J. Zide, "Observation of self-assembled core-shell structures in epitaxially embedded TbErAs nanoparticles," *Small*, vol. 10, no. 23, pp. 4920–4925, 2014.

[51] P. F. Miceli, C. J. Palmstrøm, and K. W. Moyers, "X-ray scattering study of lattice relaxation in ErAs epitaxial layers on GaAs," *Appl. Phys. Lett.*, vol. 58, no. 15, pp. 1602–1604, 1991.

[52] A. J. Young, B. D. Schultz, and C. J. Palmstrøm, "Lattice distortion in single crystal rare-earth arsenide/GaAs nanocomposites," *Appl. Phys. Lett.*, vol. 104, no. 7, p. 73114, Feb. 2014.

[53] J. K. Kawasaki, B. D. Schultz, H. Lu, A. C. Gossard, and C. J. Palmstrøm, "Surface-mediated tunable self-assembly of single crystal semimetallic ErSb/GaSb nanocomposite structures," *Nano Lett.*, vol. 13, no. 6, pp. 2895–2901, 2013.

[54] B. D. Schultz, S. G. Choi, and C. J. Palmstrøm, "Embedded growth mode of thermodynamically stable metallic nanoparticles on III-V semiconductors," *Appl. Phys. Lett.*, vol. 88, no. 24, p. 243117, Jun. 2006.

[55] B. D. Schultz and C. J. Palmstrøm, "Embedded assembly mechanism of stable metal nanocrystals on semiconductor surfaces," *Phys. Rev. B - Condens. Matter Mater. Phys.*, vol. 73, no. 24, pp. 1–4, 2006.

[56] S. Andrieu and P. Fréchard, "What information can be obtained by RHEED applied on polycrystalline films?," *Surf. Sci.*, vol. 360, no. 1, pp. 289–296, 1996.

[57] D. Litvinov, T. O'Donnell, and R. Clarke, "In situ thin-film texture determination," *J. Appl. Phys.*, vol. 85, no. 4, p. 2151, 1999.

[58] J. J. Harris, B. A. Joyce, and P. J. Dobson, "Oscillations in the surface structure of Sn-doped GaAs during growth by MBE," *Surf. Sci.*, vol. 103, no. 1, pp. 90–96, 1981.

[59] A. S. Bracker, M. J. Yang, B. R. Bennett, J. C. Culbertson, and W. J. Moore, "Surface reconstruction phase diagrams for InAs, AlSb, and GaSb," *J. Cryst. Growth*, vol. 220, no. 4, pp. 384–392, 2000.

[60] C. Chatillon, J. C. Harmand, and F. Alexandre, "Thermodynamic analysis of GaAs growth by molecular beam epitaxy at the surface structure transition from 3 × 1 to 4 × 2," *J. Cryst. Growth*, vol. 130, no. 3–4, pp. 451–458, 1993.

[61] K. Regiński, J. Muszalski, V. V. Preobrazhenskii, and D. I. Lubyshev, "Static phase diagrams of reconstructions for MBE-grown GaAs(001) and AlAs(001) surfaces," *Thin Solid Films*, vol. 267, no. 1–2, pp. 54–57, 1995.

[62] A. P. Kajdos and S. Stemmer, "Surface reconstructions in molecular beam epitaxy of SrTiO3," *Appl. Phys. Lett.*, vol. 105, no. 19, pp. 1–5, 2014.

[63] V. P. LaBella, M. R. Krause, Z. Ding, and P. M. Thibado, "Arsenic-rich GaAs(0 0 1) surface structure," *Surf. Sci. Rep.*, vol. 60, no. 1–4, pp. 1–53, 2005.

[64] G, "E-IMFP universal-en.svg," *Wikipedia*, 2015. .

[65] "NIST X-ray Photoelectron Spectroscopy Database, Version 4.1," *National Institute of Standards and Technology, Gaithersburg*, 2012. .

[66] M. Schmid, "ScanningTunnelingMicroscopeSchematic.png," *Wikipedia*, 2005. .

[67] J. Tersoff and D. R. Hamann, "Theory of the scanning tunneling microscope," *Phys. Rev. B*, vol. 31, no. 2, pp. 805–813, 1985.

[68] J. Tersoff and D. Hamann, "Theory and application for the scanning tunneling microscope," *Phys. Rev. Lett.*, vol. 50, no. 25, p. 1998, 1983.

[69] J. Bardeen, "Tunnelling from a Many-Particle Point of View," *Phys. Rev. Lett.*, vol. 6, no. 2, pp. 57–59, Jan. 1961.

[70] R. M. Feenstra, J. A. Stroscio, J. Tersoff, and A. P. Fein, "Atom-selective imaging of the GaAs(110) surface," *Phys. Rev. Lett.*, vol. 58, no. 12, pp. 1192–1195, Mar. 1987.

[71] R. M. Feenstra, "Tunneling spectroscopy of the (110) surface of direct-gap III-V semiconductors," *Phys. Rev. B*, vol. 50, no. 7, pp. 4561–4570, 1994.

[72] Q. Fu, T. Wagner, and M. Rühle, "Hydroxylated α-Al2O3 (0001) surfaces and metal/α-Al2O3 (0001) interfaces," *Surf. Sci.*, vol. 600, no. 21, pp. 4870–4877, 2006.

[73] D. C. Streit and F. G. Allen, "Thermal and Si-beam assisted desorption of SiO 2 from silicon in ultrahigh vacuum," *J. Appl. Phys.*, vol. 61, no. 8, pp. 2894–2897, Apr. 1987.

[74] P. Dumas, Y. J. Chabal, and P. Jakob, "Morphology of hydrogen-terminated Si(111) and Si(100) surfaces upon etching in HF and buffered-HF solutions," *Surf. Sci.*, vol. 269–270, pp. 867–878, May 1992.

[75] R. M. Tromp, R. J. Hamers, and J. E. Demuth, "Si(001) Dimer Structure Observed with Scanning Tunneling Microscopy," *Phys. Rev. Lett.*, vol. 55, no. 12, pp. 1303–1306, Sep. 1985.

[76] S. M. Gray, "Nanoscale roughening of Si(001) by oxide desorption in ultrahigh vacuum," *J. Vac. Sci. Technol. B Microelectron. Nanom. Struct.*, vol. 14, no. 2, p. 1043, 1996.

[77] S. M. Gates, R. R. Kunz, and C. M. Greenlief, "Silicon hydride etch products from the reaction of atomic hydrogen with Si(100)," *Surf. Sci.*, vol. 207, no. 2–3, pp. 364–384, 1989.

[78] R. P. H. Chang, "Hydrogen plasma etching of semiconductors and their oxides," *J. Vac. Sci. Technol.*, vol. 20, no. 1, p. 45, 1982.

[79] B. Jφrgensen and P. Morgen, "Surface composition of SiC after ion bombardment, annealing, and exposure to oxygen," *J. Vac. Sci. Technol. A Vacuum, Surfaces Film.*, vol. 4, no. 3, pp. 1701–1704, 1986.

[80] D. N. Belton, S. J. Harris, S. J. Schmieg, A. M. Weiner, and T. A. Perry, "In situ characterization of diamond nucleation and growth," *Appl. Phys. Lett.*, vol. 54, no. 5, pp. 416–417, 1989.

[81] Y. Mizokawa, S. Nakanishi, O. Komoda, S. Miyase, H. S. Diang, C. H. Wang, N. Li, and C. Jiang, "Differences in Auger electron spectroscopy and x-ray photoelectron spectroscopy results on the bonding states of oxygen with β-SiC(100) surfaces," *J. Appl. Phys.*, vol. 67, no. 1, pp. 264–269, 1990.

[82] I. Kusunoki and Y. Igari, "XPS study of a SiC film produced on Si(100) by reaction with a C2H2 beam," *Appl. Surf. Sci.*, vol. 59, no. 2, pp. 95–104, 1992.

[83] J. M. Martinis and A. Megrant, "UCSB final report for the CSQ program: Review of decoherence and materials physics for superconducting qubits," *Arxiv:1410.5793*,

p. 10, 2014.

[84] S. M. Lee, S. H. Lee, M. M. Sung, D. Marton, S. S. Perry, and J. W. Rabalais, "Annealing effects on surface morphology of Si(100)," in *Proceedings of 11th International Conference on Ion Implantation Technology*, pp. 650–653.

[85] D. Eaglesham, H.-J. Gossmann, and M. Cerullo, "Limiting thickness h_{epi} for epitaxial growth and room-temperature Si growth on Si(100)," *Phys. Rev. Lett.*, vol. 65, no. 10, pp. 1227–1230, Sep. 1990.

[86] B. Jalan, P. Moetakef, and S. Stemmer, "Molecular beam epitaxy of SrTiO3 with a growth window," *Appl. Phys. Lett.*, vol. 95, no. 3, pp. 2–5, 2009.

[87] J. Y. Tsao, *Materials Fundamentals of Molecular Beam Epitaxy*. San Diego: Academic Press, Inc., 1993.

[88] L. Feigl, B. D. Schultz, S. Ohya, D. G. Ouellette, A. Kozhanov, and C. J. Palmstrøm, "Structural and transport properties of epitaxial PrNiO3 thin films grown by molecular beam epitaxy," *J. Cryst. Growth*, vol. 366, pp. 51–54, 2013.

[89] M. Kareev, S. Prosandeev, J. Liu, C. Gan, A. Kareev, J. W. Freeland, M. Xiao, and J. Chakhalian, "Atomic control and characterization of surface defect states of TiO2 terminated SrTiO3 single crystals," *Appl. Phys. Lett.*, vol. 93, no. 6, p. 61909, 2008.

[90] M. K. Stewart, J. Liu, M. Kareev, J. Chakhalian, and D. N. Basov, "Mott physics near the insulator-to-metal transition in NdNiO3," *Phys. Rev. Lett.*, vol. 107, no. 17, pp. 1–5, 2011.

[91] Y. Kumar, R. J. Choudhary, S. K. Sharma, M. Knobel, and R. Kumar, "Strain dependent stabilization of metallic paramagnetic state in epitaxial NdNiO3 thin films," *Appl. Phys. Lett.*, vol. 101, no. 13, pp. 1–6, 2012.

[92] E. Mikheev, A. J. Hauser, B. Himmetoglu, N. E. Moreno, A. Janotti, C. G. Van de Walle, and S. Stemmer, "Tuning bad metal and non-Fermi liquid behavior in a Mott material: Rare-earth nickelate thin films," *Sci. Adv.*, vol. 1, no. 10, pp. e1500797–e1500797, Nov. 2015.

[93] A. J. Hauser, E. Mikheev, N. E. Moreno, J. Hwang, J. Y. Zhang, and S. Stemmer, "Correlation between stoichiometry, strain, and metal-insulator transitions of NdNiO3 films," *Appl. Phys. Lett.*, vol. 106, no. 9, 2015.

[94] R. Scherwitzl, S. Gariglio, M. Gabay, P. Zubko, M. Gibert, and J. M. Triscone, "Metal-insulator transition in ultrathin LaNiO3 films," *Phys. Rev. Lett.*, vol. 106, no. 24, pp. 3–6, 2011.

[95] J. Son, P. Moetakef, J. M. Lebeau, D. Ouellette, L. Balents, S. J. Allen, and S. Stemmer, "Low-dimensional Mott material: Transport in ultrathin epitaxial LaNiO 3 films," *Appl. Phys. Lett.*, vol. 96, no. 6, pp. 1–4, 2010.

[96] J. Hwang, J. Son, J. Y. Zhang, A. Janotti, C. G. Van De Walle, and S. Stemmer, "Structural origins of the properties of rare earth nickelate superlattices," *Phys.*

Rev. B - Condens. Matter Mater. Phys., vol. 87, no. 6, pp. 2–5, 2013.

[97] J. R. Waldrop, R. W. Grant, S. P. Kowalczyk, and E. A. Kraut, “Measurement of semiconductor heterojunction band discontinuities by x-ray photoemission spectroscopy,” *J. Vac. Sci. Technol. A Vacuum, Surfaces, Film.*, vol. 3, no. 3, pp. 835–841, May 1985.

[98] S. A. Chambers, M. H. Engelhard, V. Shutthanandan, Z. Zhu, T. C. Droubay, L. Qiao, P. V. Sushko, T. Feng, H. D. Lee, T. Gustafsson, E. Garfunkel, A. B. Shah, J.-M. Zuo, and Q. M. Ramasse, “Instability, intermixing and electronic structure at the epitaxial LaAlO3/SrTiO3(001) heterojunction,” *Surf. Sci. Rep.*, vol. 65, no. 10–12, pp. 317–352, Oct. 2010.

[99] G. Conti, A. M. Kaiser, A. X. Gray, S. Nemšák, G. K. Pálsson, J. Son, P. Moetakef, A. Janotti, L. Bjaalie, C. S. Conlon, D. Eiteneer, A. A. Greer, A. Keqi, A. Rattanachata, A. Y. Saw, A. Bostwick, W. C. Stolte, A. Gloskovskii, W. Drube, S. Ueda, M. Kobata, K. Kobayashi, C. G. Van de Walle, S. Stemmer, C. M. Schneider, and C. S. Fadley, “Band offsets in complex-oxide thin films and heterostructures of SrTiO 3 /LaNiO 3 and SrTiO 3 /GdTiO 3 by soft and hard X-ray photoelectron spectroscopy,” *J. Appl. Phys.*, vol. 113, no. 14, p. 143704, Apr. 2013.

[100] S. Miyazaki, “Photoemission study of energy-band alignments and gap-state density distributions for high-k gate dielectrics,” *J. Vac. Sci. Technol. B Microelectron. Nanom. Struct.*, vol. 19, no. 6, p. 2212, 2001.

[101] Y. Y. Mi, Z. Yu, S. J. Wang, P. C. Lim, Y. L. Foo, A. C. H. Huan, and C. K. Ong, “Epitaxial LaAl O3 thin film on silicon: Structure and electronic properties,” *Appl. Phys. Lett.*, vol. 90, no. 18, pp. 1–4, 2007.

[102] S. G. Lim, S. Kriventsov, T. N. Jackson, J. H. Haeni, D. G. Schlom, A. M. Balbashov, R. Uecker, P. Reiche, J. L. Freeouf, and G. Lucovsky, “Dielectric functions and optical bandgaps of high- K dielectrics for metal-oxide-semiconductor field-effect transistors by far ultraviolet spectroscopic ellipsometry,” *J. Appl. Phys.*, vol. 91, no. 7, pp. 4500–4505, 2002.

[103] L. F. Edge, D. G. Schlom, S. A. Chambers, E. Cicerrella, J. L. Freeouf, B. Holländer, and J. Schubert, “Measurement of the band offsets between amorphous LaAlO3 and silicon,” *Appl. Phys. Lett.*, vol. 84, no. 5, pp. 726–728, Feb. 2004.

[104] Y. Y. Mi, Z. Yu, S. J. Wang, P. C. Lim, Y. L. Foo, A. C. H. Huan, and C. K. Ong, “Epitaxial LaAlO3 thin film on silicon: Structure and electronic properties,” *Appl. Phys. Lett.*, vol. 90, no. 18, p. 181925, Apr. 2007.

[105] N. F. Mott, “Conduction in non-crystalline systems-09-the minimum metallic conductivity,” *Philos. Mag.*, vol. 26, no. 4, pp. 1015–1026, 1972.

[106] T. Ying, Y. Gu, X. Chen, X. Wang, S. Jin, L. Zhao, W. Zhang, and X. Chen, “Anderson localization of electrons in single crystals: LixFe7Se8,” *Sci. Adv.*, vol. 2, no. 2, pp. 4–11, 2016.

[107] J. Okabayashi, A. Kimura, O. Rader, T. Mizokawa, A. Fujimori, T. Hayashi, and M. Tanaka, "Angle-resolved photoemission study of Ga1−xMnxAs," *Phys. Rev. B*, vol. 64, no. 12, p. 125304, Sep. 2001.

[108] H. K. Yoo, S. I. Hyun, L. Moreschini, Y. J. Chang, D. W. Jeong, C. H. Sohn, Y. S. Kim, H.-D. Kim, A. Bostwick, E. Rotenberg, J. H. Shim, and T. W. Noh, "Dimensional crossover of the electronic structure in LaNiO3 ultrathin films: Orbital reconstruction, Fermi surface nesting, and the origin of the metal-insulator transition," *arXiv*, p. 17, 2013.

[109] P. D. C. King, H. I. Wei, Y. F. Nie, M. Uchida, C. Adamo, S. Zhu, X. He, I. Božović, D. G. Schlom, and K. M. Shen, "Atomic-scale control of competing electronic phases in ultrathin $LaNiO_3$.," *Nat. Nanotechnol.*, vol. 9, no. 6, pp. 443–7, 2014.

[110] A. X. Gray, A. Janotti, J. Son, J. M. Lebeau, S. Ueda, Y. Yamashita, K. Kobayashi, A. M. Kaiser, R. Sutarto, H. Wadati, G. A. Sawatzky, C. G. Van De Walle, S. Stemmer, and C. S. Fadley, "Insulating state of ultrathin epitaxial LaNiO3 thin films detected by hard x-ray photoemission," *Phys. Rev. B - Condens. Matter Mater. Phys.*, vol. 84, no. 7, pp. 1–6, 2011.

[111] E. Sakai, K. Yoshimatsu, M. Tamamitsu, K. Horiba, A. Fujimori, M. Oshima, and H. Kumigashira, "Bandwidth-controlled metal-insulator transition in epitaxial PrNiO 3 ultrathin films induced by dimensional crossover," *Appl. Phys. Lett.*, vol. 104, no. 17, 2014.

[112] A. Tiwari, K. P. Rajeev, T. K. Nath, and A. K. Nigam, "Metal–insulator transition in NdNi1−xFexO3−δ," *Solid State Commun.*, vol. 110, no. 2, pp. 109–114, Mar. 1999.

[113] A. K. Raychaudhuri, K. P. Rajeev, H. Srikanth, and R. Mahendiran, "Low temperature studies on normal perovskite oxides: role of correlation and disorder," *Phys. B Condens. Matter*, vol. 197, no. 1–4 pt 3, pp. 124–132, 1994.

[114] A. K. Raychaudhuri, K. P. Rajeev, H. Srikanth, and N. Gayathri, "Metal-insulator transition in perovskite oxides: Tunneling experiments," *Phys. Rev. B*, vol. 51, no. 12, pp. 7421–7428, Mar. 1995.

[115] B. L. Altshuler and A. G. Aronov, "Zero bias anomaly in tunnel resistance and electron-electron interaction," *Solid State Commun.*, vol. 30, no. 3, pp. 115–117, Apr. 1979.

[116] B. V. Beznosikov and K. S. Aleksandrov, "Perovskite-like crystals of the Ruddlesden-Popper series," *Crystallogr. Reports*, vol. 45, no. 5, pp. 792–798, 2000.

[117] S. N. Ruddlesden and P. Popper, "The compound Sr 3 Ti 2 O 7 and its structure," *Acta Crystallogr.*, vol. 11, no. 1, pp. 54–55, 1958.

[118] S. Asanuma, P. H. Xiang, H. Yamada, H. Sato, I. H. Inoue, H. Akoh, A. Sawa, K. Ueno, H. Shimotani, H. Yuan, M. Kawasaki, and Y. Iwasa, "Tuning of the metal-insulator transition in electrolyte-gated NdNiO 3 thin films," *Appl. Phys. Lett.*, vol. 97, no. 14, pp. 3–6, 2010.

[119] J. Son, B. Jalan, A. P. Kajdos, L. Balents, S. James Allen, and S. Stemmer, "Probing the

metal-insulator transition of NdNiO3 by electrostatic doping," *Appl. Phys. Lett.*, vol. 99, no. 19, pp. 3–6, 2011.

[120] S. Chalmers, H. Kroemer, and A. Gossard, "Step-flow growth on strained surfaces:(Al, Ga) Sb tilted superlattices," *Appl. Phys. Lett.*, vol. 57, no. 17, pp. 1751–1753, 1990.

[121] M. Volmer and W. Schultze, "Condensation on Crystals," *Z. phys. Chem.*, vol. 156, p. 1, 1931.

[122] T. Sands, C. J. Palmstr??m, J. P. Harbison, V. G. Keramidas, N. Tabatabaie, T. L. Cheeks, R. Ramesh, and Y. Silberberg, "Stable and epitaxial metal/III-V semiconductor heterostructures," *Mater. Sci. Reports*, vol. 5, no. 3, pp. 99–170, 1990.

[123] J. W. Cahn and R. E. Hanneman, "(111) Surface tensions of III–V compounds and their relationship to spontaneous bending of thin crystals," *Surf. Sci.*, vol. 1, no. 4, pp. 387–398, 1964.

[124] E. Penev, S. Stojković, P. Kratzer, and M. Scheffler, "Anisotropic diffusion of In adatoms on pseudomorphic InxGa1-xAs films: First-principles total energy calculations," *Phys. Rev. B*, vol. 69, no. 11, p. 115335, 2004.

[125] R. L. Schwoebel and E. J. Shipsey, "Step motion on crystal surfaces," *J. Appl. Phys.*, vol. 37, no. 10, pp. 3682–3686, 1966.

[126] P. F. Miceli and C. J. Palmstrøm, "X-ray scattering from rotational disorder in epitaxial films: An unconventional mosaic crystal," *Phys. Rev. B*, vol. 51, no. 8, pp. 5506–5509, Feb. 1995.

[127] E. T. Croke, F. Grosse, J. J. Vajo, M. F. Gyure, M. Floyd, and D. J. Smith, "Substitutional C fraction and the influence of C on Si dimer diffusion in Si1-yCy alloys grown on (001) and (118) Si," *Appl. Phys. Lett.*, vol. 77, no. 9, pp. 1310–1312, 2000.

[128] J. Vollmer, J. Hegedüs, F. Grosse, and J. Krug, "Impurity-induced step interactions: A kinetic Monte Carlo study," *New J. Phys.*, vol. 10, 2008.

[129] S. Link and M. A. El-Sayed, "Size and Temperature Dependence of the Plasmon Absorption of Colloidal Gold Nanoparticles," *J. Phys. Chem. B*, vol. 103, no. 21, pp. 4212–4217, May 1999.

[130] J. A. Logan, S. J. Patel, S. D. Harrington, C. M. Polley, B. D. Schultz, T. Balasubramanian, A. Janotti, A. Mikkelsen, and C. J. Palmstrøm, "Observation of a topologically non-trivial surface state in half-Heusler PtLuSb (001) thin films," *Nat. Commun.*, vol. 7, no. 7, p. 11993, 2016.

[131] S.-Y. Xu, I. Belopolski, N. Alidoust, M. Neupane, G. Bian, C. Zhang, R. Sankar, G. Chang, Z. Yuan, C.-C. Lee, S.-M. Huang, H. Zheng, J. Ma, D. S. Sanchez, B. Wang, A. Bansil, F. Chou, P. P. Shibayev, H. Lin, S. Jia, and M. Z. Hasan, "Discovery of a Weyl Fermion semimetal and topological Fermi arcs," *Science (80-.).*, no. July, p. science.aaa9297-, 2015.

[132] P. Roushan, J. Seo, C. V Parker, Y. S. Hor, D. Hsieh, D. Qian, A. Richardella, M. Z. Hasan, R. J. Cava, and A. Yazdani, "Topological surface states protected from backscattering by chiral spin texture.," *Nature*, vol. 460, no. 7259, pp. 1106–1109, 2009.

[133] F. Cuccureddu, S. Murphy, I. V. Shvets, M. Porcu, H. W. Zandbergen, N. S. Sidorov, and S. I. Bozhko, "Surface morphology of c-plane sapphire (α-alumina) produced by high temperature anneal," *Surf. Sci.*, vol. 604, no. 15–16, pp. 1294–1299, 2010.

[134] D. S. Wisbey, J. Gao, M. R. Vissers, F. C. S. Da Silva, J. S. Kline, L. Vale, and D. P. Pappas, "Effect of metal/substrate interfaces on radio-frequency loss in superconducting coplanar waveguides," *J. Appl. Phys.*, vol. 108, no. 9, 2010.

[135] Glosser.ca, "Bloch Sphere.svg," *Wikipedia*, 2012. .

XI. Appendix A – sapphire surface prep and buffer growth

A. Ex-situ preparation of sapphire (0001) surface

In order to investigate what role cleaning procedures have on the metal-substrate interface we leverage the in-situ characterization capabilities of an interconnected MBE, XPS, and STM. Two different dielectric substrates were studied c-plane sapphire, the same used by our collaborators in the Martinis group in previous works,[17] and Si (001).

Prior to loading into the MBE system the sapphire substrates underwent several ex-situ processes. The sapphire substrates used were prepared from a 3-inch sapphire wafer and diced into 1 cm x 1 cm squares with photoresist spun on the surface to protect the polished surface from damage during the dicing process. As received substrates are chemical mechanical polished (CMP) resulting in a smooth but inconsistently terminated surface. To achieve a more desirable surface the substrates were thermally annealed in air at 1050°C for a minimum of 30 minutes, see Figure XI-1. This results in smooth terraces of 0.22 nm heights corresponding to atomic monolayers of sapphire.[133] The process requires the anneal to be in air, a pure oxygen environment instead results in

faceting of the substrate surface, we postulate that the reason is the presence of water vapor in air enabling OH termination of the sapphire surface.

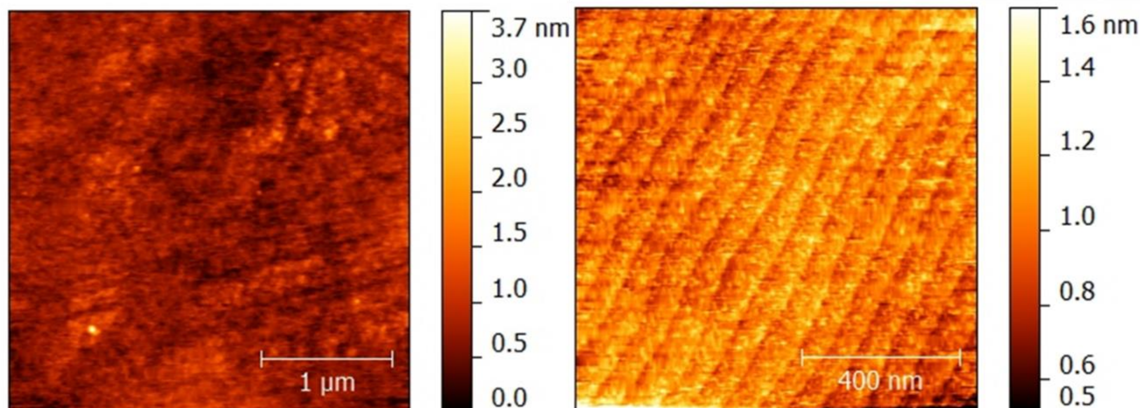

Figure XI-1 AFM micrographs showing (left) an as received CMP sapphire (0001) surface and (right) a sapphire (0001) surface annealed in air at 1050°C for 30 minutes. Step height of the right micrograph correspond to single monolayers with a thickness of 0.22 nm.

Next substrates had several hundred nanometers of Tantalum metal deposited on the back side. This is a standard process used in the Palmstrøm lab for any transparent substrate (most oxides) that must go to high temperatures. Typically molten Indium is used to adhere a substrate to a molybdenum block which acts as a heatsink during growth and a means to move the sample throughout the vacuum system, however, at temperatures >700°C the high vapor pressure of Indium makes this method unsuitable. Instead substrates are held in place via Ta clips, due to poor thermal contact without indium the indium free sample blocks expose the back of the sample directly to the heater, since the substrate material is transparent most of the heat is not absorbed by the substrate material and so the Ta coating on the backside of the substrate acts as an absorption layer for the heat radiated by the heater allowing for effective heat transfer from the substrate heater to the substrate. Finally the substrates are solvent cleaned by

sonication in methanol, isopropanol, and DI water prior to loading into the UHV MBE system (exception being etched Si wafers discussed later).

B. Sapphire buffer growth

There exists an alternate method of interface improvement that has been put to good use in the growth of III-V materials. When growing III-V materials it is common practice to grow a buffer layer of substrate material after desorbing the thermal oxide, this serves to bury any contaminates from the original surface beneath the buffer layer away from sensitive device structures. This is beneficial for semiconductor growth since MBE grown III-V materials are of extremely high quality, a similar process would be beneficial for the qubit devices since burying defects from the original interface would move them away from the qubit and the electric fields generated by it. Before this can be implemented it is necessary to be able to grow high quality epitaxial sapphire.

Growing Al_2O_3 is a relatively trivial process, in fact it is already in use during the fabrication of the qubits themselves and can be accomplished by oxidation of Al, CVD, or e-gun deposition, unfortunately, all of these processes result in amorphous Al_2O_3 or some suboxide form of it. In order for the buffer layer to be beneficial it must be epitaxial and perfectly crystalline in the sapphire (α-Al_2O_3 phase) any deviations will result in disorder and enable the formation of TLS.

The first method of sapphire growth explored was growth of Al from an elemental source in an oxidizing environment. The Al was evaporated from an oxygen resistant k-cell with a cell temperature ranging from 1100°C-1200°C. The oxidizing source was an Ozone generator outputting ~15% O_3 and ~85% O_2, oxygen flow was set so that the

background pressure of the chamber was at $1x10^5$ torr. Sapphire (0001) substrates were loaded in after the standard solvent clean and outgassed to ~300°C prior to growth. Three different growth regimes were observed, shown in Figure XI-2. For substrate temperatures less than 700°C a diffuse background is observed in RHEED and diffraction streaks fade away indicative of amorphous material. Substrate temperatures from 700°C to 1050°C result in crystalline growth with diffraction lines that seem to match the spacing of sapphire, but the RHEED is composed of clearly defined spots indicating large amounts of surface roughness. As substrate temperature is increased to >1050°C RHEED remains streaky but ex-situ analysis by AFM and profilometer show no detectable growth. From this it is quite clear that the observed morphologies are due to Al and AlO_x mobility on the surface. At low temperatures Al readily adheres to the substrate but upon oxidation AlO_x mobility is low resulting in amorphous material. As temperature increases sufficient mobility is achieved to allow the AlO_x to form crystalline material, but since the initial elemental Al is balled up from the difference in surface energies between metallic Al and sapphire, the resulting sapphire growth is also rough and 3D RHEED spots are observed. This could be rectified if AlO_x mobility is increased to the point where diffusion allows the mounds to diffuse to a smooth surface. However, before this can be reached the sapphire substrate becomes hot enough that incident elemental Al adatoms are desorbed before oxidation can occur, resulting in no growth.

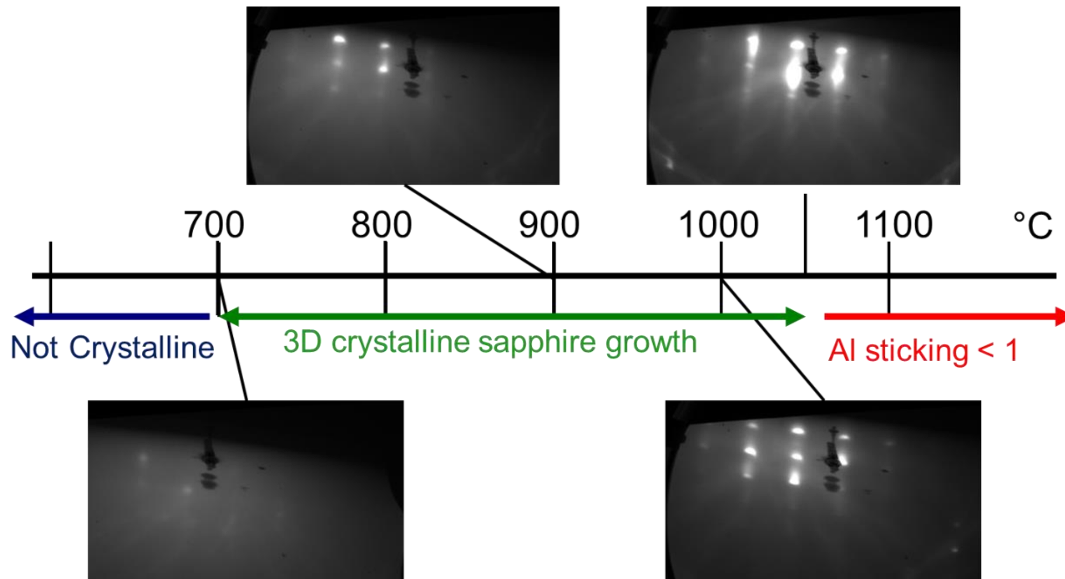

Figure XI-2 RHEED images along the [1000] for sapphire grown by oxidation of elemental Al at several different substrate temperatures. Three regimes are shown corresponding to amorphous, 3D, and Al adatom sticking coefficient of <<1.

The next method of sapphire growth explored was deposition of AlO_x from an e-gun deposition source in an oxidizing environment. The source material in the e-gun hearth was a crushed sapphire wafer, but the process of e-gun evaporation typically breaks some Al-O bonds resulting in a non-stoichiometric material, for this reason the same oxidizing environment used for the elemental Al growths was employed here. Figure XI-3 shows the RHEED images for e-gun deposition of sapphire at two different substrate temperatures as well as the initial substrate prior to deposition. At 900°C the AlO_x incident on the substrate does not have sufficient mobility to grow as a smooth layer and 3-D growth is observed, resulting in similar RHEED patterns observed for growth of sapphire from elemental Al. However, the AlOx is able to maintain a non-zero sticking coefficient to higher temperatures and at 1200°C substrate temperature streaky RHEED is observed, with clear deposition viewable by surface line scans.

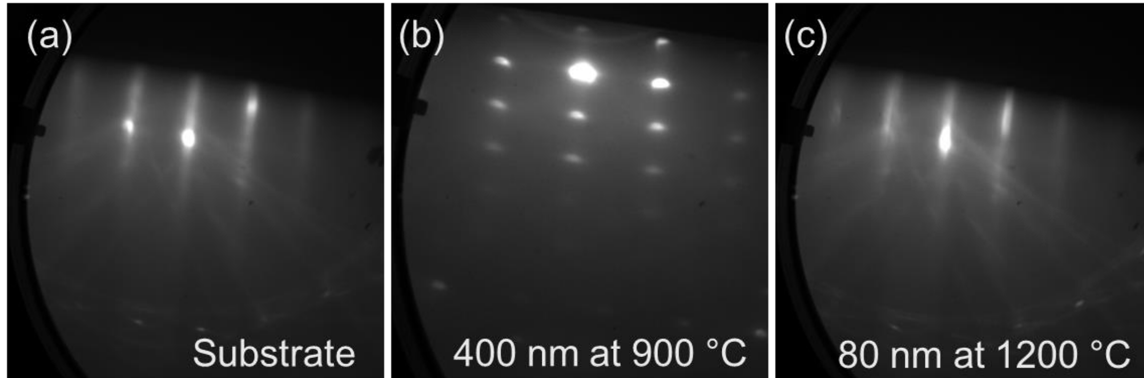

Figure XI-3 RHEED images along the [1000] showing (a) typical initial substrate diffraction, (b) ~400 nm of Al_2O_3 *deposited at a substrate temperature of 900°C, and (c) 80 nm of* Al_2O_3 *deposited at a substrate temperature of 1200°C.*

Although not fully characterized, it should be noted that the sapphire surface does seem to be sensitive to the oxidizing environment at high substrate temperatures even when no film growth occurs, see Figure XI-4. This is assumed to be due to loss of oxygen from the substrate when annealed at high temperatures in vacuum. The RHEED shows increased thickness in the diffraction streaks, this broadening is indicative of defect formation within the crystal, hints of spots are also visible indicating surface roughening. This is avoidable by cooling down the sample in the oxidizing environment previously described.

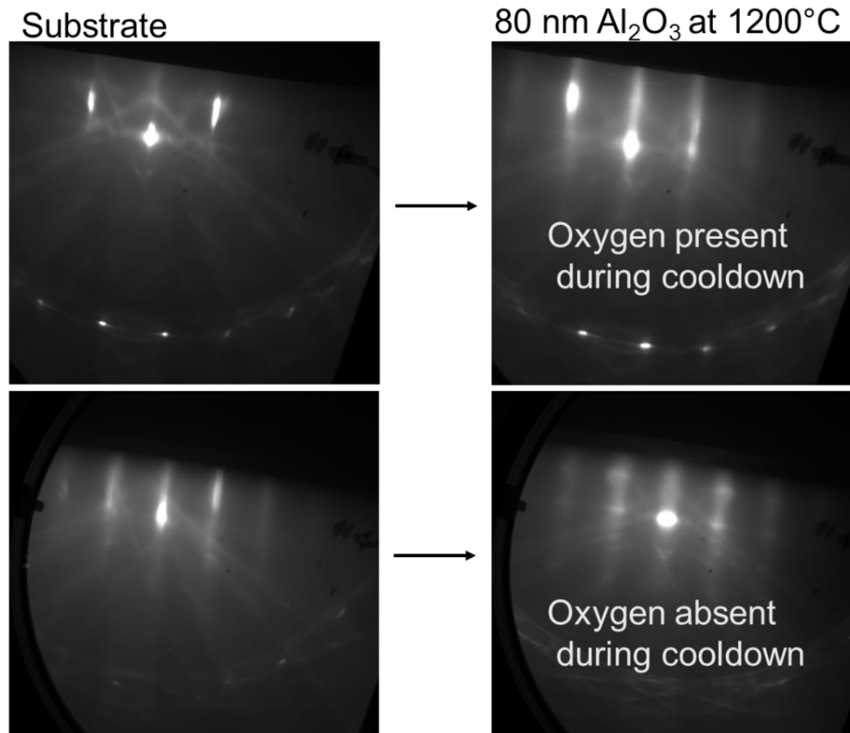

Figure XI-4 RHEED along the [1000] direction of sapphire surface grown at 1200°C with and without an oxidizing environment present during high temperatures. (Left) Images of the starting substrate before growth (Right) images corresponding to samples after 80 nm of Al_2O_3 deposition.

It is challenging to evaluate the crystal quality of the e-gun deposited sapphire buffer layer, a triple axis XRD scan is shown in Figure XI-5 shows a decrease in the full width half max of the (0006) diffraction peak from 12.2 arcsec to 12.06 arcsec. However, given that the film is only 80nm thick, and the relatively low Z elements composing sapphire XRD is likely not a technique sensitive to the thin film quality, and the most that can be said is that film quality is not measurably worse after growth.

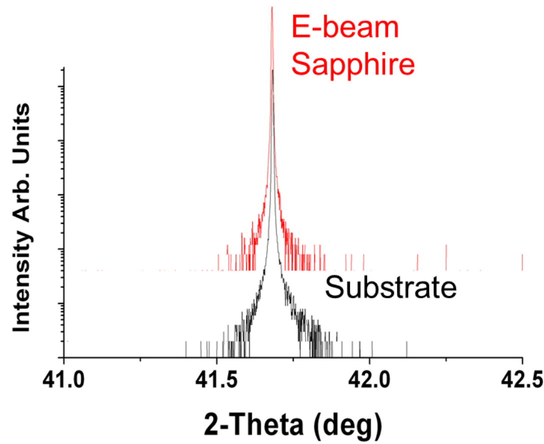

Figure XI-5 Triple axis XRD scan of the (0006) peak for a sapphire substrate before growth and the same sample after deposition of 80nm of sapphire at 1200°C.

AFM of a 1200°C deposited sapphire film can be seen in Figure XI-6. It is readily apparent that despite the promising looking RHEED, the surface is still not as smooth as the well-defined terraces obtained by ex-situ annealing. It is unknown what exact role surface roughness has on the loss of SCW's, some findings in the literature may indicate that losses scale with gap roughness,[134] but in this study roughness was not the only factor influencing SCW performance. A relatively naïve viewpoint would suggest that any additional surface roughness is unfavorable as it would provide additional surface area for TLS formation.

It was demonstrated that the surface achieved by high temperature e-gun deposition of sapphire did allow for textured growth of Al. RHEED of ~100 nm of Al deposited on sapphire for two different substrate growth conditions can be seen in Figure XI-7. At room temperature Al went down polycrystalline as seen by a RHEED pattern depicting rings, in contrast to growth in the Martinis MBE system we found that heating the sample slightly was required to get (111) textured Aluminum. This

discrepancy can be relatively easily explained by differences in thermocouple and cryoshield position between the two MBE systems.

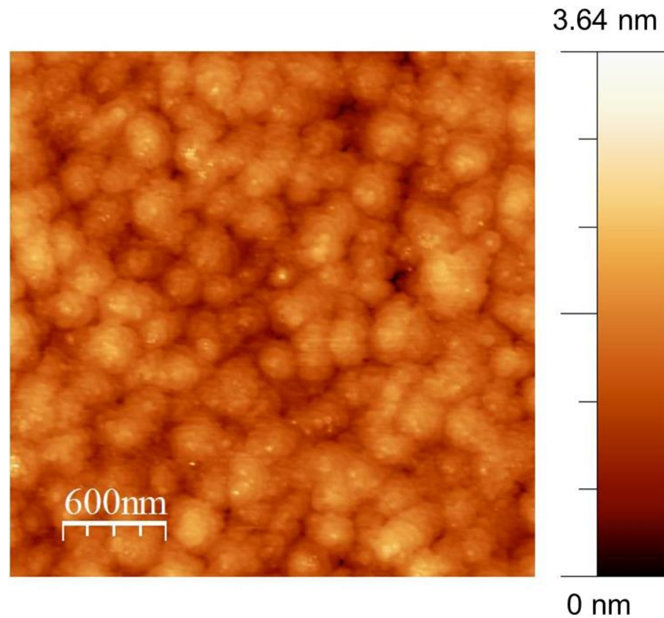

Figure XI-6 AFM of an 80 nm Sapphire film deposited at 1200°C in an Ozone overpressure.

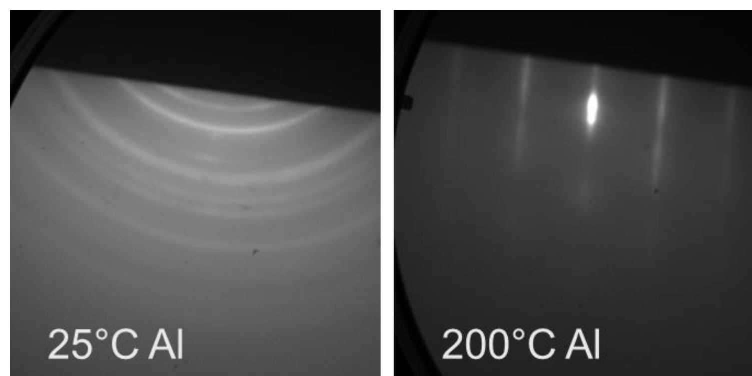

Figure XI-7 RHEED of Al grown on a (0001) sapphire surface grown by in-situ e-gun deposition for two different substrate temperatures. 25°C samples shows rings indicative of a polycrystalline film.

While promising it appears that the current MBE system is limited by substrate temperature when growing Al_2O_3 buffer layers, it is possible that higher substrate

temperatures would enable enough surface diffusion for atomically smooth surfaces. If that is achievable the rest of the process needed to fabricate a fully in-situ substrate-metal interface is already implemented.

XII. Appendix B – STM of Heusler materials

A. NiTiSn

Several collaborations have occurred with other members of the Palmstrøm research group focusing on charactization of half-Heusler and full-Heusler surfaces. Anthony Rice has been working on the semiconducting half-Heusler NiTiSn. Growth of Heusler materials by MBE is a challenging process primarily due to the lack of a growth window, many of the Heuslers are comprised entirely elements with sticking coefficients of 1 making stoichiometric growth of the materials challenging. For NiTiSn this problem is somewhat alleviated by the existence of several surface reconstructions sensitive to the composition of the material. A phase diagram of the observed surface reconstructions is shown in Figure XII-1. During growth RHEED shows a c(2x2) for Ti deficient films, a (2x1) for films near stoichiometry and a (1x1) reconstruction for films with Ti excess. After cooling films to room temperature after growth two other reconstructions are observed a (2x2) is seen at Ti poor coniditons between the c(2x2) and the (2x1), and a c(2x4) is observed for Ti rich conditions between the (2x1) and the (1x1).

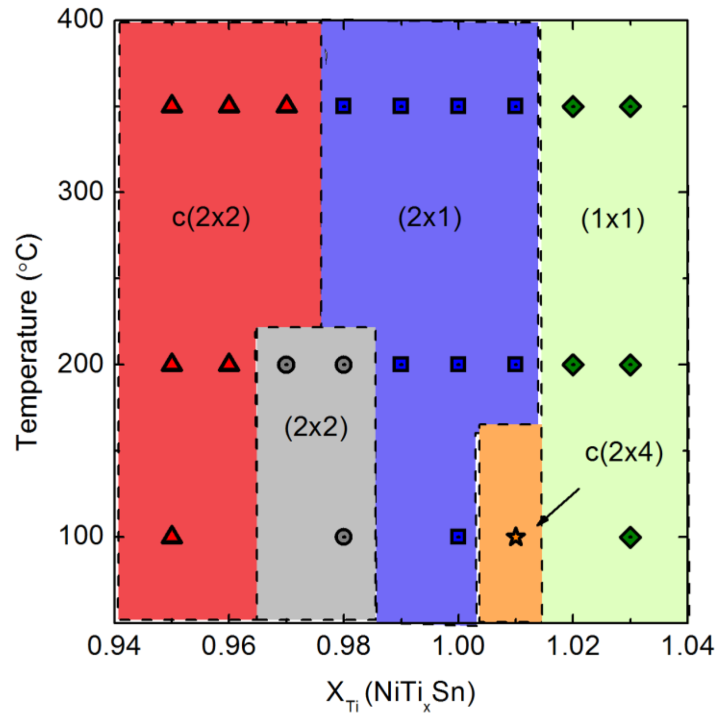

Figure XII-1 Approximate surface reconstruction phase diagram as a function of temperature and bulk Ti composition. Points represent experimental observations. Figure courtesy of Anthony Rice.

Samples grown by Anthony Rice were characterized via in-situ STM at 77K for samples that were Sn rich/Ti deficient $NiTi_{0.97}Sn_1$, stoichiometric NiTiSn, and Ti rich/Sn deficient $NiTi_{1.01}Sn_{.99}$. STM images of these surfaces along with line scans can be seen in Figure XII-2, the images show the reconstructions observed by RHEED of the sample surfaces. Figure XII-2(a) shows what may be Sn droplets on the surface as well in a small enough concentration that they are not observable in XPS measurements performed on the surface. Both the (2x1) and c(2x4) reconstructions observed in Figure XII-2(b,c) show regions where the reconstruction is rotated 90°, resulting in different domains of the same surface reconstruction.

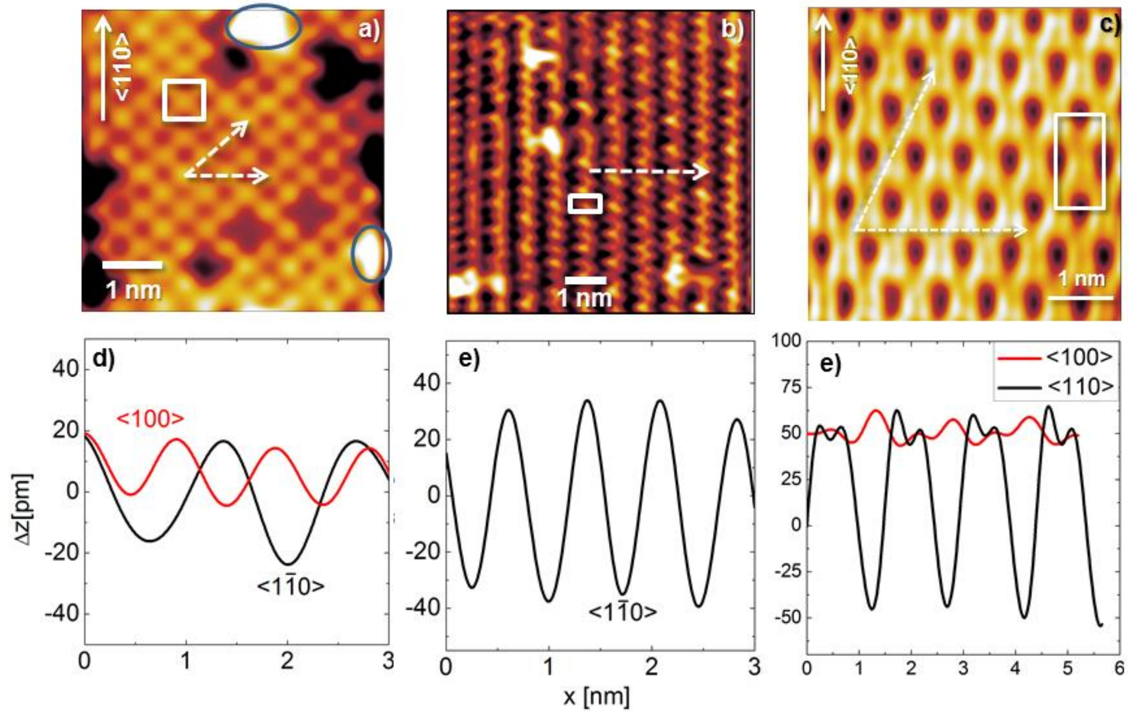

Figure XII-2 (a-c) STM images of c(2x2) ($NiTi_{0.97}Sn_{1.03}$), (2x1) (NiTiSn) and c(2x4) ($NiTi_{1.01}Sn_{0.99}$) surfaces showing filled states at 77K using a W tip with a bias of -0.5V and a tunneling current of 30 pA, (d-f) Depth profiles of the corresponding surfaces to surface above, with dotted lines marking where depth profiles were taken, and solid squares highlighting surface unit cells. The c(2x4) and (2x1) surface also showed domains rotated 90° relative to those shown.

A full-Heusler sample was also examined (Ni_2TiSn) via in-situ STM. RHEED of this sample showed ½ order streaks along the <110> directions consistent with the formation of surface unit cell rotated 45° and with periodicity of $1/\sqrt{2}$. STM of the surface can be seen in Figure XII-3 and reveals that the surface is in fact comprised of rows indicating the predicting shrinking of the surface unit cell only occurs along one of the <110> directions, the presence of the half-order streaks in RHEED along both the [110] and [1$\bar{1}$0] directions is explained in the STM by observations of the surface reconstruction rotated 90° on other terraces. The sum of the diffraction from both orientations explains the observed diffraction in RHEED.

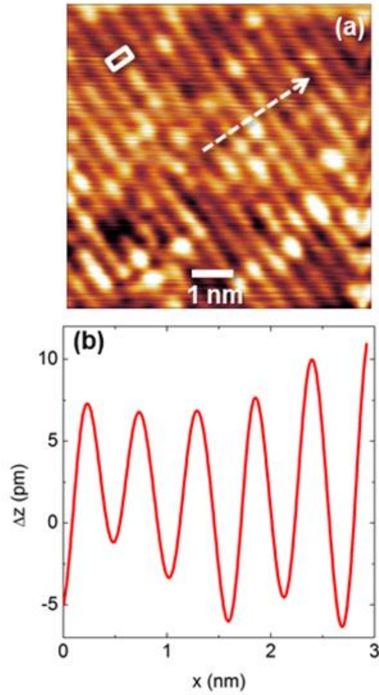

Figure XII-3 a)STM of a full-Heusler surface showing filled states at 77K using a W tip with a bias of -0.5V and a tunneling current of 30 pA and b) step profiles taken along dotted line in 8a. Other terraces on the surface showed similar rows rotated 90°.

The direct observation of the dimers present in each reconstruction allows for ball and stick models of the surfaces to be proposed. Figure XII-4 shows ball and stick models developed by Anthony Rice for the c(2x2) ($NiTi_{0.97}Sn_{1.03}$), (2x1) (NiTiSn), c(2x4) ($NiTi_{1.01}Sn_{0.99}$ at low T) and full Heusler (Ni_2TiSn) surfaces.

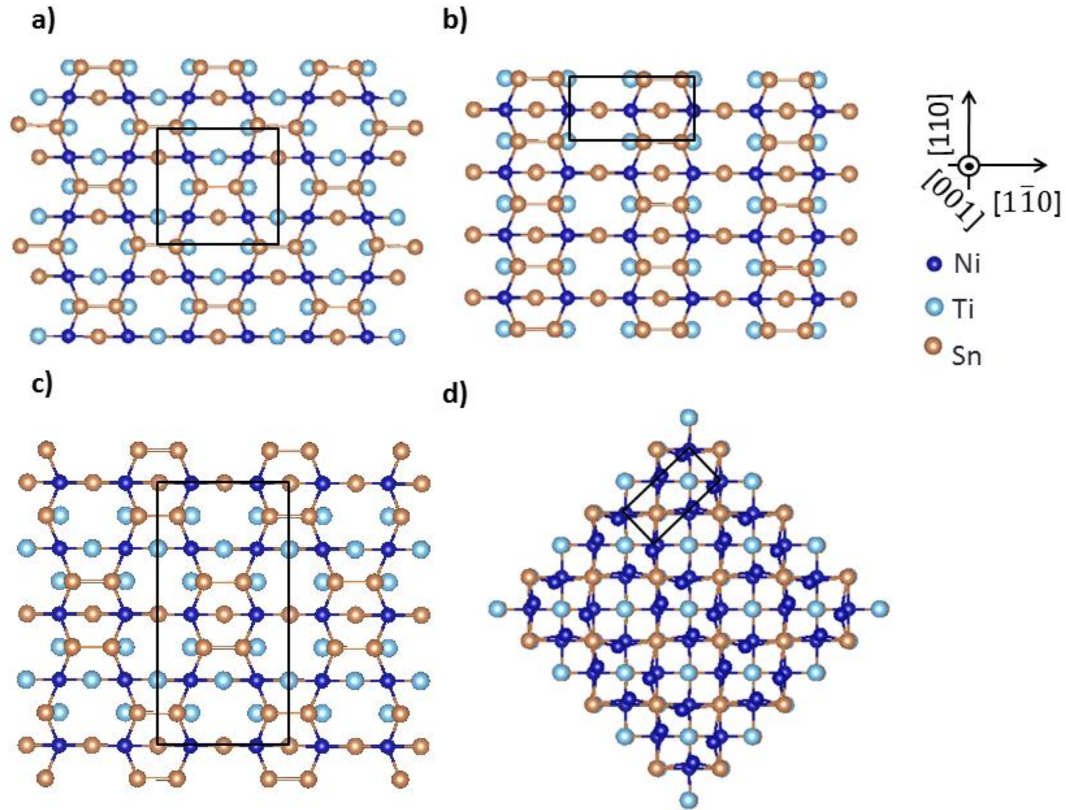

Figure XII-4 Ball-and-stick models for a) c(2x2) ($NiTi_{0.97}Sn_{1.03}$), b) (2x1) (NiTiSn), c) c(2x4) ($NiTi_{1.01}Sn_{0.99}$ at low T) and d) fH (Ni_2TiSn). Figure courtesy of Anthony Rice.

B. $Au_xPt_{1-x}LuSb$

Previous work within the group by Jay Logan showed via angle resolved photoemission spectroscopy (ARPES) that PtLuSb appears to have a dirac like linearly dispersing spin polarized topological surface state as is predicted by theory.[130] Unfortunately as grown films of PtLuSb are p-doped placing the Fermi level squarely within the valence band of the material, this is problematic as the dirac crossing is located approximately 0.24 eV above the Fermi level which is not able to be probed by ARPES. One possibility for moving the location of the dirac crossing with respect to the Fermi level is to dope the material, a promising approach for this while preserving the topological properties of the material is alloying with Au on the Pt site in the crystal.

For that purpose STM images and STS measurements of PtLuSb and various compositions of $Au_xPt_{1-x}LuSb$ where performed.

Figure XII-5 shows STM images at 4K for the PtLuSb surface without any alloying with gold. A smooth and ordered surface with an observable surface reconstruction is easily observed via STM. In contrast the various samples with Au alloying all show vastly different surfaces with no such consistent surface reconstruction observable, see Figure XII-6.

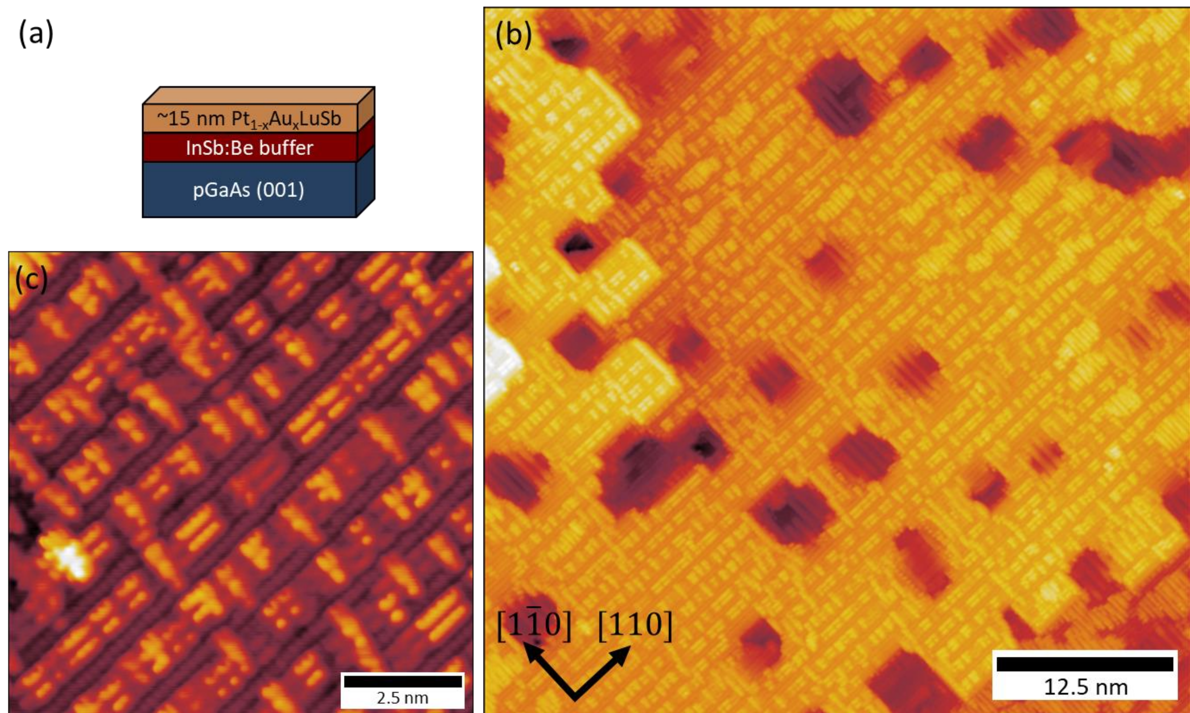

Figure XII-5 (a) Diagram of the sample structure used for STM measurements. (b) Image of the PtLuSb surface at 4k and a bias of -0.5V. (c) blowup of the dominant surface reconstruction observed for the PtLuSb surface.

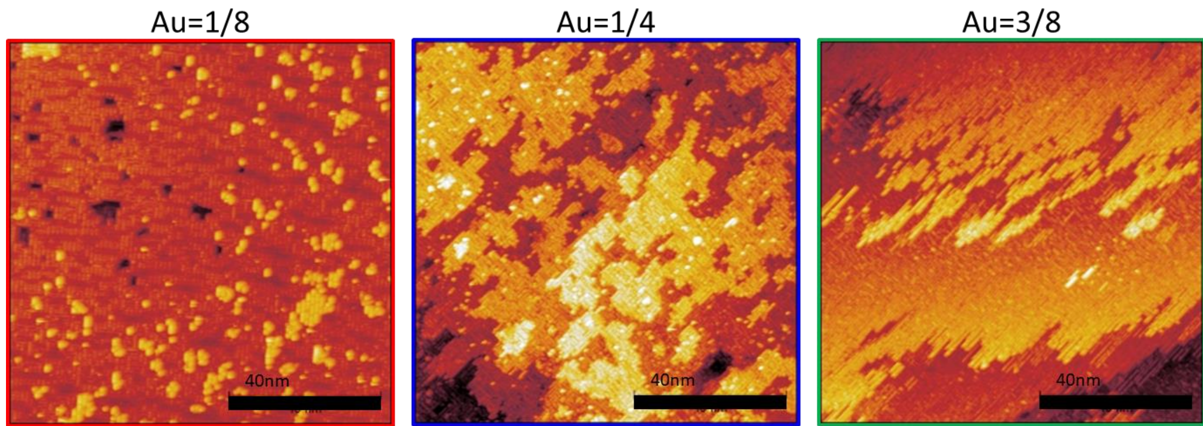

Figure XII-6 STM images of the surfaces for $Au_xPt_{1-x}LuSb$ samples where x = 1/8, ¼, and 3/8. Unlike PtLuSb consistent surface reconstructions were not observed and samples were significantly rougher.

STS measurements of the various surfaces can be seen plotted in Figure XII-7, these measurements were performed using the variable tip height method at a temperature of 4K. The valence band of the various samples appears to have a pair of peaks with relatively consistent spacing present in each measurement. The position of these peaks can be measured and plotted as a function of Au alloying, assuming that the shift in energy of the peak position corresponds to a shift in the Fermi level it is predicted that the Fermi level will lie on the dirac crossing for a composition of ~$Au_{0.45}Pt_{0.55}LuSb$. This conclusion makes the assumption that the increasing amount of Au within the crystal structure does not significantly change the position of the conduction and valence bands which may or may not be true and alter the total composition of Au needed.

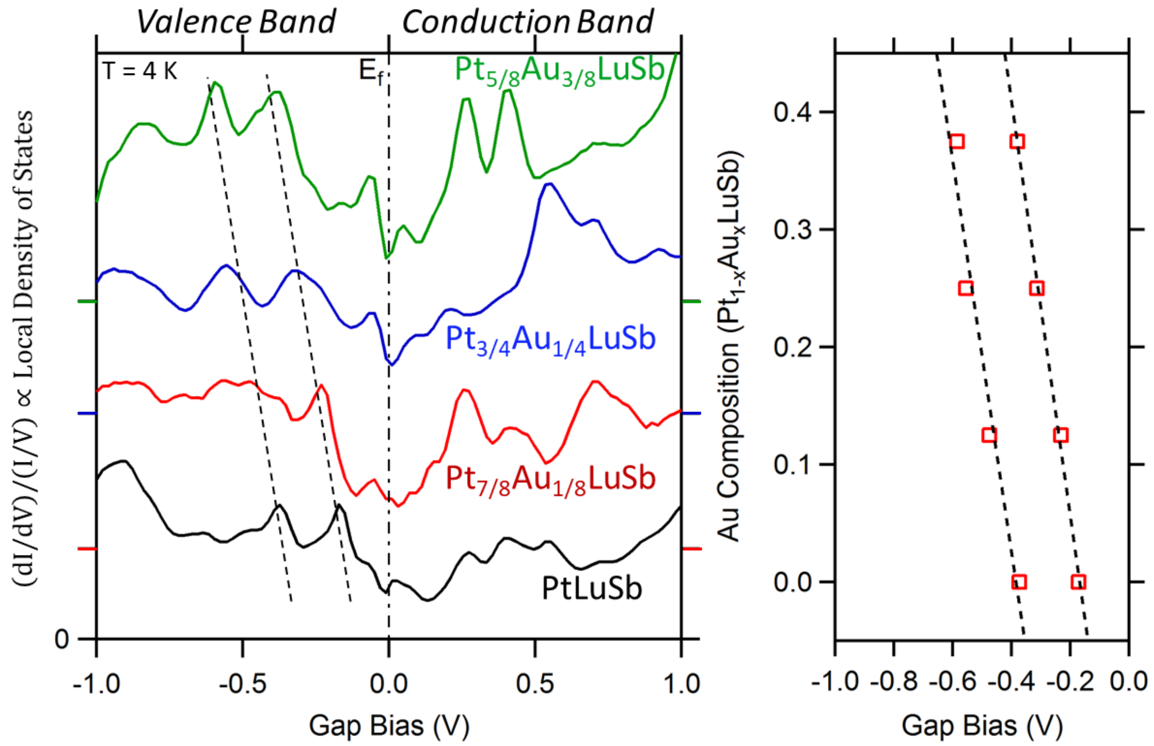

Figure XII-7 (Left) Variable tip height STS measurements for various compositions of $Au_xPt_{1-x}LuSb$, STS spectra are vertically offset from each other. A consistent pair of peaks is observable across all samples in the valence band showing a shift with Au composition, no such consistent feature is present in the conduction band. (Right) linear fit of the position of the pair of peaks in the valence band to sample composition.